Two-photon polymerization of immune cell scaffolds

Olsen, Mark Holm; Larsen, Niels Bent; Hjortø, Gertrud Malene

Publication date:
2013

Document Version
Publisher's PDF, also known as Version of record

Two-photon polymerization of immune cell scaffolds

PhD Thesis

Mark Holm Olsen

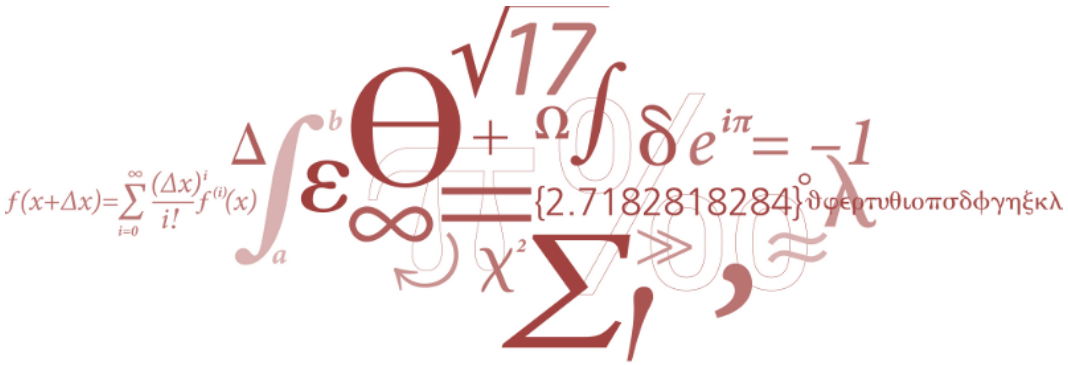

DTU Nanotech
Department of Micro- and Nanotechnology

DTU

PhD Thesis – Mark Holm Olsen

Supervisor – Niels B. Larsen, Co-supervisor – Gertrud M. Hjortø

DTU Nanotech, Department of Micro- and Nanotechnology – Technical University of Denmark

September 2013

Abstract

Cancer is the leading cause of mortality in the developed world despite major advances in therapy in recent years. Recently cancer immune therapies have developed into promising treatments against a number of cancer types. One of the most promising is dendritic cell based cancer immunotherapy. One of the major challenges towards increasing the vaccine efficacy has been to develop maturation procedures that produce highly immunogenic dendritic cells that also demonstrate strong migratory skills.

To test the migratory skills of the dendritic cells induced by the different procedures we present a versatile and easy to use chip integrated migration platform. Free-form constructs with three-dimensional (3D) microporosity were fabricated by two-photon polymerization inside the closed microchannel of an injection molded commercially available polymer chip for analysis of directed cell migration. Acrylate constructs were produced as woodpile topologies with a range of pore sizes from 5x5 µm to 15x15 µm and prefilled with fibrillar collagen. Dendritic cells seeded into the polymer chip in a concentration gradient of the chemoattractant CCL21 efficiently negotiated the microporous maze structure for pore sizes of 8x8 µm or larger. Cells migrating through smaller pore sizes made significantly more turns than through larger pores. Linear microchannels with diameters from 10 µm to 20 µm were also produced and simultaneous observations of dendritic cells migrating in the confined channels and in the fibrillar collagen were performed. Cells occluding the microchannels exhibited significantly higher migration speed than cells not occluding the channels and cells migrating in the fibrillar collagen.

To more precisely mimic the mechanical and chemical properties of the tissue traversed by the dendritic cells we also present a poly (ethylene glycol) diacrylate (PEGDA) based strategy to fabricate soft 3D hydrogel scaffolds. Our experiments with the hydrogel confirm we can control the mechanical properties and introduce biochemical cues on the surface that are recognized by fibroblast cells. Finally we present initial in-chip fabrication of soft 3D constructs holding more than 80 % water.

Resumé

Kræft er den hyppigste dødsårsag i den udviklede verden trods store fremskridt i behandlingen i de seneste år. Senest har forskellige kræft immunterapier udviklet sig til lovende behandlinger mod en række kræftformer. En af de mest lovende er dendritcelle baseret Cancer immunterapi. En af de store udfordringer for at øge effekten af denne vaccine har været at udvikle procedurer, der opmodner meget immunogene dendritceller, der samtidig udviser gode migrations evner, vigtigt for at finde vej tilbage til lymfe systemet.

For at teste dendritcellernes migrationsfærdigheder afhængigt af hvilken af de forskellige procedurer der er blevet brugt præsenterer vi en alsidig og let tilgængelig test platform integreret i en mikrofluid chip. Konstruktioner med 3-dimensionel(3D) mikroporøsitet er blevet fremstillet med 2-foton polymerisering inde i en sprøjtestøbt kommercielt tilgængelig og lukket mikrokanal chip for at analysere guidet celle migration. Konstruktionerne blev udformet som woodpile geometrier med porestørrelser fra 5x5 um til 15x15 um og udfyldt med fibrillært kollagen. Dendritceller der blev indsat i chippen, som har en koncentrationsgradient af kemokinet CCL21, navigere effektivt gennem den mikroporøse labyrintstruktur hvis porestørrelserne er 8x8 um eller større. Celler der navigerer gennem mindre porestørrelser drejer signifikant flere gange end gennem større porer. Lineære mikrokanaler med diametre fra 10 um til 20 um blev også produceret. I dem blev der foretaget simultane observationer af dendritceller der migrerer i trange kanaler, og i den fibrillære kollagen. Celler der fylder mikrokanalerne ud, udviser signifikant højere migrations hastighed end celler der ikke fylder mikrokanalerne ud og end celler der migrerer i den fibrillære kollagen.

For mere præcist at efterligne de mekaniske og kemiske egenskaber af vævet som dendritcellerne migrere igennem i kroppen, præsenterer vi også en poly (etylenglycol) diakrylat (PEGDA) baseret strategi til at fabrikere bløde 3D hydrogel konstruktioner. Vores eksperimenter med hydrogel bekræfter at vi kan styre de mekaniske egenskaber og krydsbinde biokemiske signaler på overfladen, der bliver genkendt af fibroblastceller. Endelig præsenterer vi indledende forsøg med at fabrikere bløde 3D hydrogel konstruktioner indeholdende mere end 80 % vand, inde i mikrokanal chippen.

Acknowledgements

I would like to thank everyone who has contributed to this thesis.

I would especially like to thank:

My main supervisor Niels B. Larsen and my co-supervisor Gertrud Malene Hjortø for their incredible commitment and hard work.

The laboratory technicians: Ina Blom, Lene Hubert, Lotte Nielsen and Ole Kristoffersen for their help and support.

My two students: Rasmus Meyer Mortensen and Roberta Leah for their input and great job in the lab.

My present and former colleagues in the Polycell group at DTU Nanotech.

Especially:

Johan Ulrik Lind, Thomas S. Hansen, Maria Matschuk, Jan Kafka, Esben Kjær Unmack Larsen*, Morten Bo Lindholm Mikkelsen*, Thor Christian Hobæk*, Adele Faralli and Lee MacKenzie Fischer.
*Also for the many interesting discussions over lunch.

In addition, I would like to thank Jennifer West and the rest of the West Lab at Duke University for the incredible opportunity for working in their laboratory.

I would also like to thank Hanne and Casper for proofreading this manuscript.

Last but not least I would like to thank my girlfriend Rita and the rest of my family for always being there for me.

List of abbreviations

2PA	2-photon absorption
2PP	2-photon polymerization
3D	3-dimensional
Arg-Gly-Asp	Arginine-Glycine-Aspartic acid
BzA	4-benzoyl benzylamine hydrochloride
CAD	Computer aided design
CCL19	Chemokine, recognized by CCR7, secreted by the lymph nodes
CCL21	Chemokine, recognized by CCR7, secreted by the lymphatic vessels
CCR7	Chemokine receptor 7
CD86	DC surface protein neccesary for T-cell activation
DC	Dendritic Cell
DPI	Dots per inch
ECM	Extracellular matrix
FBS	Fetal Bovine Serum
GF	Grofth factor
GM	Göppert-Meyer, unit used to measure the 2PA cross section
i.d.	intra dermal
i.n.	intra nodal
I2959	Irgacure 2959, 1-[4-(2-Hydroxyethoxy)-phenyl]-2-hydroxy-2-methyl-1-propane-1-one
I369	Irgacure 369, 2-Benzyl-2-dimethylamino-1-(4-morpholinophenyl)-butanone-1
IL-12p70	Interleukin produced by DC upon antigen stimulation
IP-L	Commercial resin from Nanoscribe GmbH
IUPAC	International Union of Pure and Applied Chemistry
LOC	Lab on a chip
LSM	Laser scanning microscopy
MALDI-TOF	Matrix assisted laser disorption/ionization-time of flight
NA	Numerical aperture
NHS	*N*-Hydroxysuccinimide
NIH-3T3	Standard mouse fibroblast cell
PBS	Phosphate buffered saline
PDMS	Poly(dimethyl siloxane)
PEG	Poly(ethylene glycol)
PEGDA	Poly(ethylene glycol) diacrylate
PHEMA	Poly(2-hydroxyethyl methacrylate)
PVA	Poly(vinyl alcohol)
RGD	Arginine-Glycine-Aspartic acid
SEM	Scanning electron microscopy
TCPS	Tissue culture polystyrene

Table of Contents

1. Introduction

Cancer is the leading cause of mortality in the developed world despite major advances in therapy in recent years. Cancer can often be treated with surgery, but some cancer types such as malignant melanoma or cancer that has metastasized are no longer good candidates for surgery[1]. Most widely used treatments for inoperable cancer such as chemotherapy and radiation have severe side effects and often have little or no effect. Even after surgery a number of malignant cells will still be present and here the combination with cancer immunotherapy, a treatment that takes advantage of the patients own immune system by boosting the response against the tumor, has proven very promising. Many challenges have arisen in the search for the most optimal way to stimulate the immune system to target cancer more effectively. One of the more capable therapies involves the stimulation of dendritic cells (DC) with cancer markers to start the adaptive immune response against the tumor. One major issue for DC induced cancer immunotherapy is that the DCs lose some of their migrating skills when stimulated in the laboratory to be highly immunogenic, and thus become less capable of moving to the lymph nodes. In the lymph nodes the DCs migrate to the T-cell rich areas to induce the immune response. This drawback has lead to a plethora of investigations targeting how to maintain effective migration while the DCs are still highly immunogenic antigen presenting cells[1–3]. To evaluate these findings an easy to use and highly adaptable migration platform is needed. To approach this challenge we have developed an in-chip 3D cell migration scaffold and tested migration of DCs against a relevant migratory chemokine. In addition, we present a strategy and initial findings towards a more advanced and tissue mimicking 3D scaffold.

1.1. Dendritic cell migration and cancer immunotherapy

In the immune system the DC is the most effective antigen presenting cell. One DC is capable of activating numerous T-cells and B-cells, and the signal from one DC will therefore quickly spread to a much more effective battle against a given pathogen by activating the adaptive immune response. DCs are found as immature DCs in many parts of the body, mainly in tissues near external surfaces where they are more likely to encounter foreign pathogens. When they encounter a foreign pathogen they undergo maturation to mature dendritic cells and start to upregulate the expression of new receptors such as CD86, CCR7 and many others. CCR7 is the main migratory receptor, crucial for recognition of chemokines CCL19 and CCL21 that guide the DCs from the tissue via the afferent lymphatics to the lymph nodes. Here they are the main contributors to the effectuation of the adaptive immune response, see **Error! Reference source not found.**

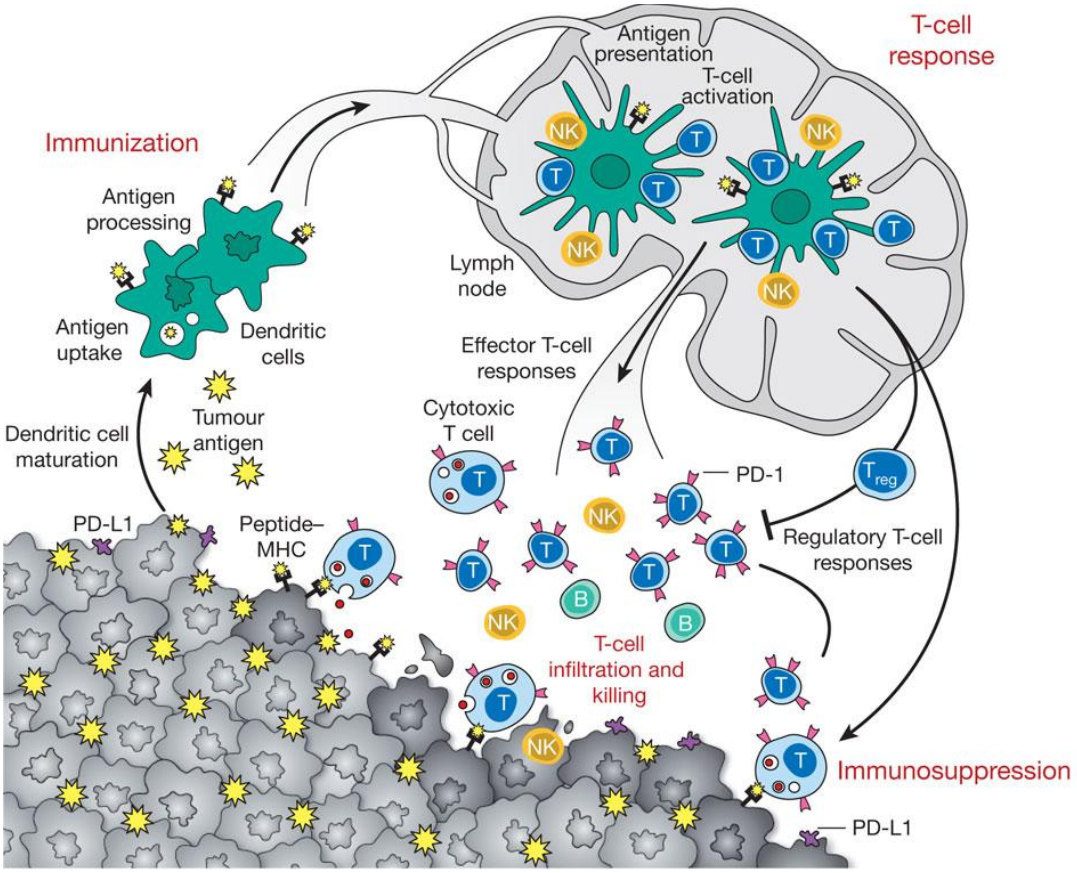

Figure 1 Schematic showing a simplified immune system with tumour antigen recognition and maturation of the dendritic cells, followed by their migration to the lymph node where they present the antigens to the T-cells. The now activated T-cells can respond with both effector and regulatory responses. The balance between these two T-cell responses is determined by the stimuli given to the dendritic cell during maturation. Therefore a huge part of building an effective cancer immunotherapy is to find the right stimuli during dendritic cell maturation. Figure adopted from Mellman et al.[4]

In DC based cancer immunotherapy the DCs are extracted from the blood of the patient as monocytes. During an up to eight day long procedure[5] the monocytes are first differentiated into immature DCs and subsequently matured followed by specific antigen presentation, either exogenously (protein, peptide, lysate) or by electroporation of mRNA representing ether specific epitopes or full tumor cell mRNA[3]. It is during this crucial period that the DCs' immunogenic and migratory skill subsets are developed. After antigen presentation the DCs are reintroduced in the body either intra nodally (i.n.) or intra dermally (i.d.), see Figure 2. The ability of the DCs to express the CCR7 receptor that recognizes the chemokines CCL19 and CCL21, secreted by the lymphatics, is paramount for an effective therapy. Recent developments have shown that the perfect maturation "cocktail" is not easy to develop, as it seems that some of the stimuli (PGE2) that increase migration potential hinder the immunogenic response by down regulating the very important immunogenic IL-12p70[1]. Observations made by Verdijk et al.[6] suggest that only a few percent of the i.d. injected cells reach the lymph nodes. While it would then seem natural just to inject the cells i.n., they found no immunogenic difference between the i.n. injected patients and the i.d. injected patients. One theory is that the clear migratory weakness of the DCs does not only hinder them in homing to the lymph nodes, but also hinders the i.n. cells in navigating inside the lymph nodes thereby lowering the immunogenic response and the therapy efficacy. Therefore a deeper understanding of DC migration mechanisms and the influence of maturation cocktails is needed to improve DC based cancer immunotherapy.

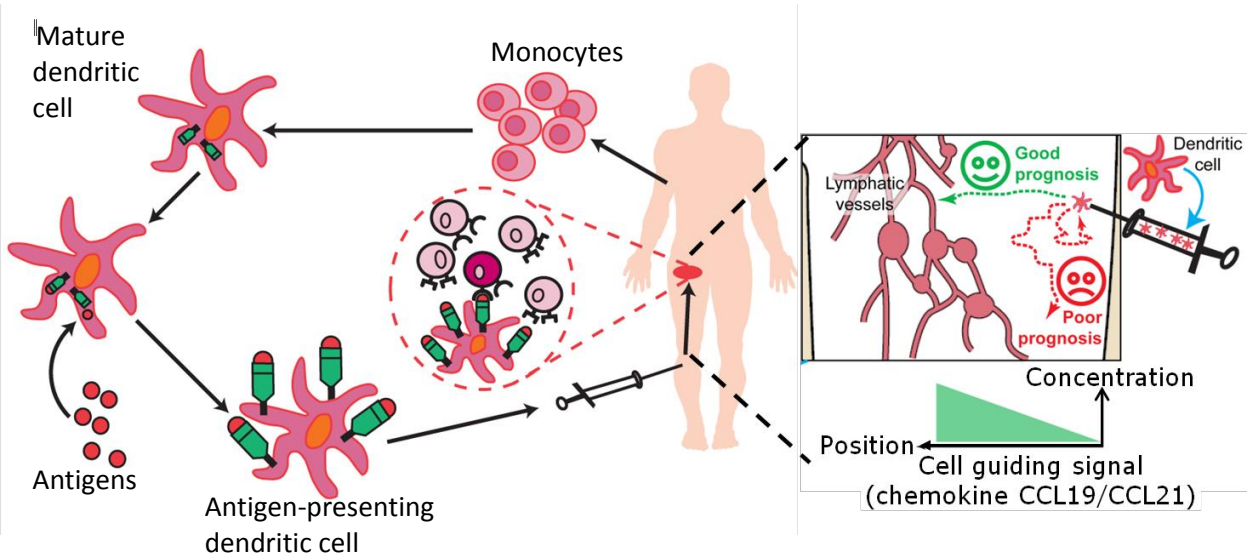

Figure 2 Schematic showing the steps of cancer immunotherapy. Monocytes are extracted from the patient and differentiated into immature DCs and then maturated into mature DCs under which they are presented to the specific antigen. Then the DCs are reinjected into the body and must migrate back to the lymph nodes to start the immune response. The lymphatic vessels and lymph nodes secret the migration guiding chemokines CCL19 and CCL21 creating a gradient that the DCs follow to the lymph nodes. If the DCs fail to migrate to the lymph nodes the patient prognosis is poorer.

1.2. Dendritic cell migration in 2D and 3D

The knowledge of *in vivo* DC migration is limited primarily because it is very difficult to visualize and track the cells. Recently a number of groups have exploited intravital two-photon microscopy to gain new knowledge about the different parts of the migration pathway from tissue to lymph node[7–9]. On their way from the tissue to the lymph nodes the DCs will encounter a plethora of obstacles, substrates and tissues[10], and studying where the injected DCs fail on their way to the lymph nodes is therefore a complicated task. CCL21 is secreted by the lymphatic vessels and it has been known for some time that the DCs respond and migrate towards the soluble chemokine gradient via the CCR7 receptor. CCL21 has been proven to also play a vital role as an anchoring point when the DCs enter the lymphatic vessels through preformed portals[7,11]. These portals have sizes of only a few micrometers and thus demand some squeezing and pulling for the large DCs to enter. For comparison , we have estimated our dendritic cells to have volume corresponding to a free diameter of 18 µm. Recently Weber et al.[8] have also confirmed that DCs perform haptotaxis when migrating towards haptotactic gradients of CCL21 immobilized in the tissue, thereby adding another crucial role to the CCR7 receptor and to the migration mechanisms of the DCs.

DCs are in a 3D environment almost all the time. Some parts of the endothelium linings might be considered by the cell as 2D, but for the vast majority of their time they will be surrounded by tissue components on all sides. For many years cell migration studies have been done on flat polystyrene petri dishes and culture flasks. These 2D studies do not resemble the environment the DCs encounter in vivo. Studies have shown that the interaction mode is different depending on the substrate dimensionality, cells simply behave differently on 3D substrates than they do on 2D surfaces[12–14]. This also translates to migration behavior, where it have been established that there are several mechanistic differences between 2D and 3D migration[15,16]. Evidence suggests that migration in 3D might have more in common with the migration mode found on 1D substrates as demonstrated by Doyle et al. who showed striking similarities in the migration mechanics. Some modes even reveal that integrin attachments are not needed for DCs to migrate through 3D collagen matrices but are only necessary when squeezing through narrow pores where contractile forces are needed to pull the nucleus through[17]. The nucleus is generally thought to be the limiting element when it comes to squeezing through narrow gaps and pores as it is less deformable and demands active cytoskeleton rearrangements[18,19]. If maturation of the DCs hinder or change any of these newly discovered mechanisms it might change the DCs homing potential in ways not yet understood.

1.3. Tissue engineering materials and 3D structured scaffolds

Cells behave differently both in culture and during migration in the 3D environment *in vivo* than they do on 2D substrates. When designing *in vitro* cell scaffolds it is therefore important to try to mimic the 3D environment as closely as possible to get realistic cell phenotypes or migration modes. Most widely used for 3D migration studies are naturally derived extracellular matrix (ECM) proteins such as collagen, as well as fibrinogen and matrigel that have been used to mimic the 3D environment of the ECM and simulate *in vivo* migration[20]. Also the polysaccharide based hydrogels, alginate, agarose and chitosan have been used exstensively[21].These gels all possess natural biochemical signals and are not always optimal if the aim of the study is a specific interaction or mechanism. Therefore artificial hydrogels such as poly(ethylene glycol) diacrylate (PEGDA), poly(vinyl alcohol) (PVA), and poly(2-hydroxyethyl methacrylate) (PHEMA) have been used as "blank slates" since they have no inherent biochemical cues. They can be chemically and mechanically modified to suit a specific tissue or cell type[22]. Especially PEGDA has been extensively used to pattern ECM proteins and growth factors in both 2D and 3D[23,24]. PEGDA has even been incorporated with biodegradable moieties, degradable by matrix metalloproteinases (also responsible for collagen degradation), allowing cells to migrate more freely as in collagen, for advanced tissue mimicking and angiogenesis studies[23,25].

These hydrogel types are random and do not permit the precise control over pore sizes and geometry needed to study specific migration mechanisms in 3D[26]. In tissue engineering this challenge has led to a plethora of ways to fabricate 3D scaffolds all with different advantages and drawbacks. Random scaffolds have been made with electrospinning and various leaching and gas techniques[27]. These scaffolds are fast and cheap to produce in large volumes for regenerative medicine, but do not employ a controlled 3D architecture. Inverse opal scaffolds made from colloidal-crystal templating, a technique developed for photonic crystals and introduced as cell scaffold by Kotov et al.[28], have both pore size control (interconnectivity) and control over the mechanical properties via range of artificial gel materials. Inverse opal scaffolds maintains the possibility to fabricate large volumes, but are limited to control over pore size and cavity size (porosity) not allowing control over more complicated geometries[29–32]. To get full control over 3D architecture and geometry computer aided design of scaffolds have emerged. These techniques utilize either a 3D printing technique to add layer by layer or a laser based technique to either add layers or directly polymerize free form structures[33]. Printing techniques are cheap and can print relatively large volumes with many different materials including soft tissue mimicking materials, but are limited by a resolution of approximately 100 µm. Stereo lithography is a widely used laser based layer by layer

technique, where a laser polymerizes a photo crosslinkable resin one layer at a time. With stereo lithography almost any geometry can be made with a resolution down to 20 µm[34]. A number of groups have used stereo lithography to build 3D cell scaffolds and constructs. Often used are acrylate based polymers such as PEGDA where it also is easy to add biochemical tissue mimicking functionalizations[35–37]. The only technique capable of fabricating true freeform scaffolds and obtain sub cellular resolution is 2-photon polymerization (2PP) or direct laser writing. 2PP is also developed for photonics but has, in recent years, found more and more use in bio medical engineering[38,39] and 3D cell mechanistic studies[40]. 2PP can be used with the same materials as most of the other 3D fabrication techniques, almost any photo crosslinkable material. The drawback of 2PP is a slow fabrication time, a consequence of the small spot size, which limits the total volume of the scaffold or construct.

All of the above mentioned technologies will need to be integrated into a macroscopic system containing fluidic handling structures that provides an easy to use platform for handling chemicals and solutions. Standard polymer fabrication techniques such as milling, hot embossing and injection molding are increasingly faster to produce polymer microchips on the industrial scale. Integrating the micro fabrication techniques with these either semi assembled or closed microfluidic systems, is a critical step towards achieving an effective easy to use migration platform. 2PP does as the only technology allow fabrication of structures inside closed microfluidic systems. This overcomes especially problems arising in the final bonding step where integrated micro structures easily break or the system is leaking. Therefore, in combination with some of the other mentioned technologies, we believe 2PP is a strong candidate for construction of confined in-chip migration scaffolds that can be tuned to mimic the mechanical, chemical and geometrical features that the DCs will encounter such as the ECM or the lymphatic vessels.

2. 2-Photon polymerization of cell migration constructs

In this section, all fabrication experiments in the hard commercial IP-L resin and the in-chip cell migration experiments in the fabricated constructs will be discussed.

2.1. What is 2-photon polymerization

2-photon polymerization is a 3D laser lithography technique. By utilizing a photo-chemical process that exploits non-linear effects of high intensity femto second lasers 2PP gains free form 3D construction capabilities by focusing the laser spot in all 3 dimensions. The 3 dimensional focusing arises from the 2-photon absorption phenomena where two photons of half the excitation energy excites a photo active molecule and starts a chemical process that cross links the resin. Effectively the 2-photon polymerization is constrained to a small volume pixel called a voxel that can be moved around, thereby creating free form 3D features. After crosslinking, the structure can be developed and the remaining resin washed away, leaving only the polymerized solid structure. A more thorough walkthrough of the optical and chemical principles can be found in the next paragraph. Since Kawata and coworkers, presented the first 3D structures created by 2PP in 1997 [41], the interest in 2PP and its applications has flourished. Pioneered by the photonics community optical crystals[42,43] and later wave guides and micro lenses were among the early applications[44,45]. Also micro mechanical systems[46,47] and lab on a chip (LOC) systems[46,48–50] were rapidly being developed taking advantage of the novel ability to create arbitrary 3D structures without the need for support structures or scaffolding. Since the 2PP technique enabled 3D structures to be constructed numerous examples of animals[51], well known landmarks[52] and figures[53] have been created to show the capabilities of the technology. Within the last couple of years biomedical applications have also been addressed, especially within the fields of tissue engineering and cell culture scaffolds that aim at mimicking *in vivo* 3D environments either in bulk[38,54,55] or by studying single cell attachments and mechanics[56]. Two examples of 3D structures fabricated by 2PP can be seen in Figure 3.

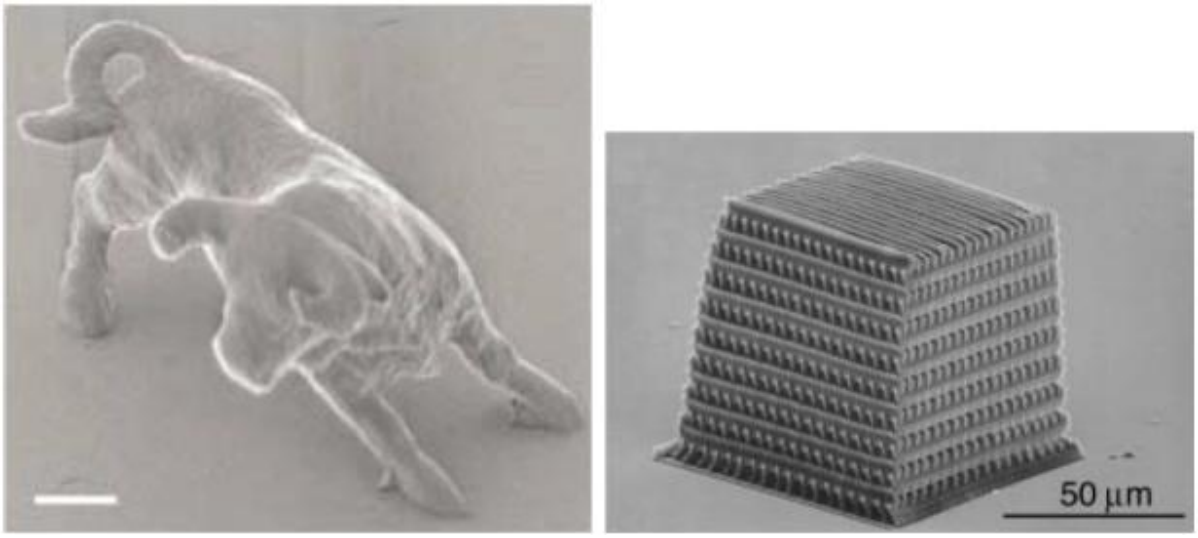

Figure 3 SEM micrographs of 2PP fabricated structures representing the ability of the technique to create arbitrary 3D structures. Left a micro sized bull[51] approaching the resolution limit of the technique and right a photonic crystal[42]. Scale bar on the left image is 2 µm.

2.1.1. Optical and chemical principles of 2-photon polymerization

2-photon polymerization is a 3D laser lithography technique where a resin is crosslinked only in the focal point of a laser. Compared to single photon laser lithography the 2-photon polymerization alters the spatial resolution from 2 dimensions to 3 dimensions. Effectively the 2PP voxel is a cigar shaped volume where the polymerization takes place. The 3rd dimension or spatial z resolution arises from the 2-photon absorption (2PA) phenomena where two photons of half the energy excite the molecule from its ground state to the excited state. For this to happen, very high photon intensity is needed. Pulsed lasers are the only light sources capable of delivering high enough intensity during their very short pulses (ns - fs) and are therefore necessary to obtain 2PA.

For 1-photon absorption the absorption rate is linearly dependent on the photon flux. When a laser beam encounters a molecule the probability of the molecule absorbing the energy of a photon is linearly proportional to the incident photon flux or intensity, ergo a 2 W laser will excite twice as many molecules as a 1 W laser at any given time. This principle works for 1-photon absorption only when the incoming photon matches the energy needed to raise an electron from the ground state to the excited singlet state. When talking about 2PA the transition from ground to excited state happens if two lower energy photons are absorbed by one molecule at the same time. Very high intensities are needed due to the very short time (10^{-18} s)[57] the molecule will be in the transient virtual state, halfway between the ground and excited state, see Figure 4. The photon energy needed for 2PA is not exactly half compared to 1-photon absorption,

but as a rule of thumb the wave length doubles for 2PA. Thus common near UV photo initiators are absorbing light in the wavelength range of 350-400 nm, they are good candidates for the near IR Ti:Sapphire lasers emitted light at 700-800 nm, though almost any photo active compound can be addressed by choosing an appropriate laser.

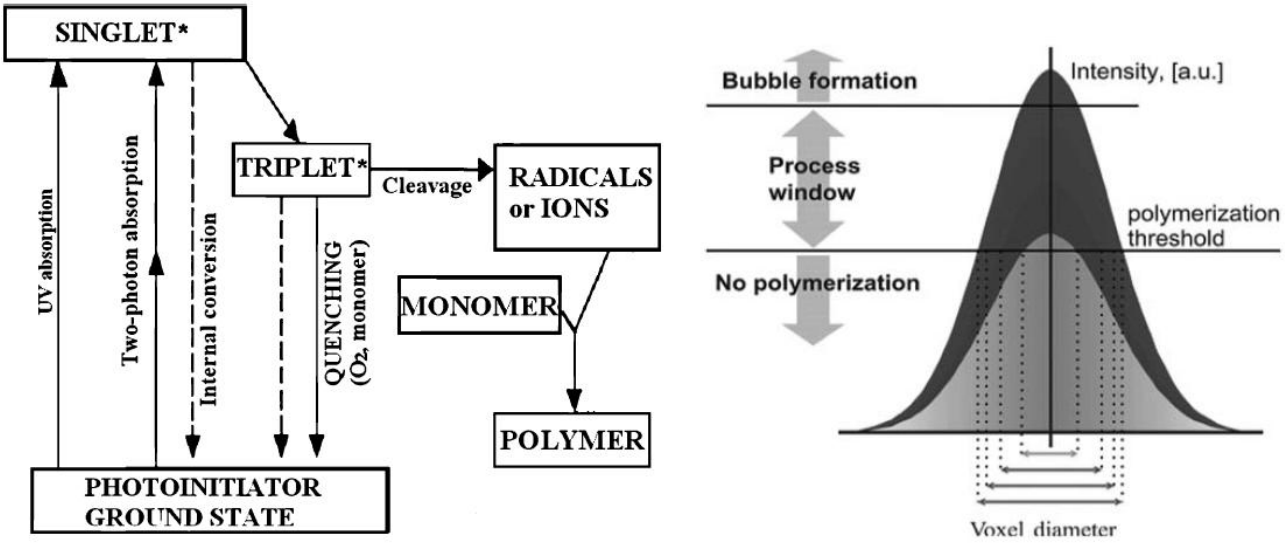

Figure 4 Left, a Jablonski style diagram adopted from Wu et al.[58] showing the activation and deactivation pathways of a photo initiator. Both single-photon and 2-photon absorption is shown as well as various deactivation pathways and internal conversion to the triplet state via cleavage creating radicals or ions that can initiate polymerization. Right, radial Gauss distribution approximating the laser intensity at the focus plane[59]. To achieve 2-photon polymerization the intensity must exceed the polymerization threshold. The volume of the focal point above the threshold defines the voxel. By carefully controlling the laser power sub diffraction limit feature sizes can be created.

2PA is a nonlinear process of the third order[60]. This means that the energy absorption rate responsible for degenerate 2PA can be described as follows:

$$\frac{dW}{dt} = \frac{8\pi^2\omega}{c^2n^2} I^2 Im[\chi^{(3)}]$$

where ω is the angular frequency, C the speed of light in vacuum, n the refractive index of the medium, I the laser intensity and $[\chi^{(3)}]$ the imaginary part of the third order susceptibility tensor. From this equation the relevant nonlinear part is the quadratic dependence on the intensity. Since 2PA only happens at the very highest of intensities above what is called the polymerization threshold, it only occurs when the laser is very focused and only in the center of the focus where the intensity is highest. To achieve this very tight focus, microscope objectives with high numerical apertures (NA) are utilized to focus the laser, because with a high NA objective the depth of field becomes very shallow and thus tightens the focus in the axial z

direction. Combining this with the rate of absorption scaling with the square of the intensity means that the likelihood of 2PA tapers off very quickly with distance from the focus center. The voxel in which the 2PA happens is thus well defined, even in the axial z direction, which is what creates the intrinsic 3D capabilities of a 2PP system. The polymerization threshold comes from the competition between deactivation mechanisms such as quenching, internal conversion and radical termination, see Figure 4, and the active radicals in the polymerization reaction. Ergo there is a threshold above which a solid structure will be created and below which the crosslinking is insufficient and the resin stays viscous or soluble[45]. The polymerization threshold is also dependent on the ability of the initiator molecule to absorb photons via 2PA, known as the 2-photon absorption cross section, *δ*. It can be found using the definition of the number of absorbed photons per time:

$$\frac{dn_p}{dt} = \delta N F^2,$$

with *N* being the number of absorbing molecules per volume and *F = I/hv* the photon flux, where *h* and *v* are the Planck constant and the frequency respectively. Knowing that

$$\frac{dW}{dt} = \frac{dn_p}{dt} h\nu$$

we get the 2-photon absorption cross section

$$\delta = \frac{16\pi^3 h\nu^2}{c^2 n^2 N} Im\left[\chi^{(3)}\right]$$

δ has units of 10^{-58} m^4 s /photon also known as GM, from the German physicist Maria Göppert-Mayer who was the first to describe 2PA in 1931[61]. It can be seen from the units that the cross section is a double area from the two separate photons needed to excite the molecule. Also noticeable is the factor of 10^{-58} which is inserted to normalize most compounds to a 2-photon cross-section between 1 GM and 10^3 GM. This factor also tells us why really high laser intensities are needed for 2PA to occur.

When a molecule, here a radical photo initiator, is excited by 2PA a fraction of the excited molecule will undergo internal conversion to the triplet state and from there cleave and create radicals or ion species eventually starting the polymerization, see Figure 4. The fraction of photons that creates a radical is called the radical quantum yield, ϕ, and is another important parameter after the 2PA cross section to yield an effective 2PP initiator. The radical quantum yield should not be confused with the fluorescent quantum yield, *η*, often expressed for chromophores[62] as the fraction of absorbed photons being emitted as

fluorescence. A high radical quantum yield is therefore dependent on a low fluorescence quantum yield since lower η means greater chance of intersystem crossing to the triplet state and thus a higher ϕ[63]. As can be seen in Figure 4, a high fluorescence (path not shown) quantum yield and internal conversion quantum yield gives less triplet states and thus less chance of cleavage and radical formation. The radical formation rate, r_r, thus scales with the laser intensity squared, the 2PA cross section and the radical quantum yield:

$$\boldsymbol{r_r \sim \phi \delta I^2}$$

A photo initiator with a high $\boldsymbol{\delta}$ and a high ϕ (or low η) is desired to achieve more efficient polymerization at lower power and faster processing speeds.

Due to the above mentioned factors, the volume being polymerized by a 2PP system is confined in 3 dimensions and thus able to create arbitrary 3D features in any photo active material. Because the laser light is not absorbed below the threshold intensity 2PP can be performed in the bulk of the material, as compared to standard lithography techniques where the light will be absorbed along the way and restrict polymerization to the very surface or at least to a shallow top layer, see Figure 5.

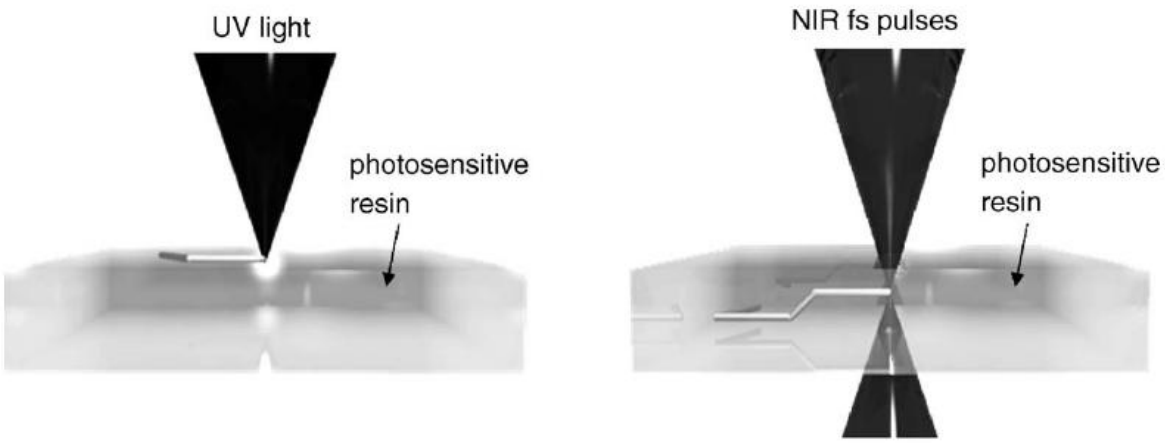

Figure 5 Left, when using 1-photon absorption the UV laser light is absorbed at the surface and thus only 2D structures can be created. When using a near IR laser for 2PP the light travels through the sample without being absorbed and allows in depth polymerization at the focus plane of true 3D structures[58].

Polymerization speed and degree will be governed by the chemistry used in the resin. The following equations shows the photoinitiation step in a 2PA activated radical reaction:

$$\boldsymbol{I + 2h\nu \rightarrow I^* \rightarrow R^{\cdot}}$$

The photoinitiator absorbs the two photons and undergo intersystem crossing (ISC) and cleavage to become an activated radical that can initiate polymerization of a given monomer:

$$\boldsymbol{M + R^{\cdot} \rightarrow RM^{\cdot} + M \rightarrow RMM^{\cdot} \ldots . \rightarrow RM_n^{\cdot}}$$

In 2PP this reaction implies cross linking of the created polymer chains either between themselves or by an added cross linking agent to create the solid polymer that makes up the 3D structure. Radical lifetime and polymerization efficiency depends on a number of factors including radical termination by quenching (O_2, other radicals), internal cyclization (combination) and chain transfer to another organic molecule in the resin[64]. These factors will depend on photoinitiator, monomer and solvent as well as reaction conditions (temperature, atmosphere) and are thus very different from resin to resin and this will affect the minimum feature size and processing parameters.

The feature size achievable with 2PP is theoretically infinitely small since the voxel dimensions depend on the width and height of the laser beam being over the polymerization threshold intensity, see Figure 4. The voxel dimensions are however, in reality, limited by system and laser power stability and the applied photo chemistry and monomer composition[53]. The smallest achievable feature size will scale with the objective used to focus the laser. Calculations adopted from 2-photon microscopy can easily be used to estimate how the voxel size scales with different objectives and immersion media. From Webb et al[65] it follows that the optical resolution (area in which 2PA occur) can be calculated by the following expressions (for NA>0.7):

$$r_{xy} = \frac{0.325\lambda}{\sqrt{2}NA^{0.91}} \qquad r_z = \frac{0.532\lambda}{\sqrt{2}}\left[\frac{1}{n - \sqrt{n^2 - NA^2}}\right]$$

r_{xy} and r_z are the lateral and axial resolution respectively, λ the wavelength, n refractive index of medium and NA the numerical aperture of the objective. When inserting parameters from our 2PP system we get voxel dimensions of: $d = 2r_{xy} = 264\ nm$ and $l = 2r_z = 622\ nm$ which is already well below the diffraction limited resolution from a 780 nm light source ($r_{xy} = 0.61\lambda/NA$)[53]. Important to note from these equations is that the voxel length in z scales with the square of the numerical aperture of the objective and is thus a very important parameter to achieve minimum feature sizes. The aspect ratio of the voxel calculated here is less than 3. In reality the axial resolution is not as good as predicted and it is more realistic to expect aspect ratios between 3 and 6[66], meaning that the voxel takes the shape of a Cuban cigar. The aspect ratio as well as the overall size of the voxel also scales with laser power and exposure time. Since the voxel is not a well defined structure but the definition of a threshold energy, right outside of the voxel the radical concentration will be very close to the threshold. By increasing laser power and exposure time the polymerized volume will grow. An increase in laser power or exposure time will affect the aspect ratio in different ways according to Sun et al[67] and it is not completely understood how the exposure parameters together with radical lifetime and radical diffusion contribute to the overall shape of the polymerized volume. However, it can be concluded that the smallest achievable dimensions are obtained

with a high NA objective at near threshold laser intensity and that high laser intensities and high 2PA cross sections will allow shorter exposure times.

2.1.2. Two-photon polymerization in Biomedical engineering

2PP research has, as previously mentioned, developed rapidly from purely proof of concept to photonics and micromechanical systems since the first demonstration in 1997[41]. Features have been routinely fabricated down to 100 nm by several groups[45,68], but also features well below 100 nm have been presented[69,70]. When applying 2PP for fabrication of devices or systems for biomedical purposes high resolution is rarely the subject of investigation. Feature sizes of single cell dimensions of 3 µm - 50 µm are far more relevant. The easy computer assisted design (CAD) of 3D structures means that biomedical devices for a number of applications have been realized. The ability to control features in the µm range have spurred researchers to investigate single cell mechanics[56] by constructing small web like structures with rods that bend depending on the force asserted on them, see Figure 6. This includes 3D adhesion properties in 3D scaffolds featuring two different resin components, one component for the 3D rod scaffold and one component for the specific adhesion sites[40].

Tissue mimicking scaffolds of various shapes and symmetries have also been constructed with 2PP. Most common are structures based on either stacked cylindrical blocks[54,71,72] or linear rods creating either woodpile[55,73–76] or cross-hatched[71,73,74,77,78] structures, but also more complicated scaffolds based on spheres[79], truncahedrons[80] or Schwarz P-surfaces[74] have been created. Most of these scaffolds have feature sizes well above single cell dimensions, and those investigating cell sized features seem to conclude that they are less suitable for the cell culturing purposes they are intended for due to the cells being unable to properly spread and adhere[73,75]. When studying 3D cell migration Tayalia et al.[55] employed smaller features with pore sizes in the woodpile down to 12 µm by 12 µm and conclude that even though the pores are about the size of a single cell, migration speed is only slightly reduced. In a later study they completely abandon the smallest pore size[76] in favor of 25 µm to 75 µm pores. A woodpile from Tayalia et al. can be seen in Figure 6 with 12 µm x 25 µm pores.

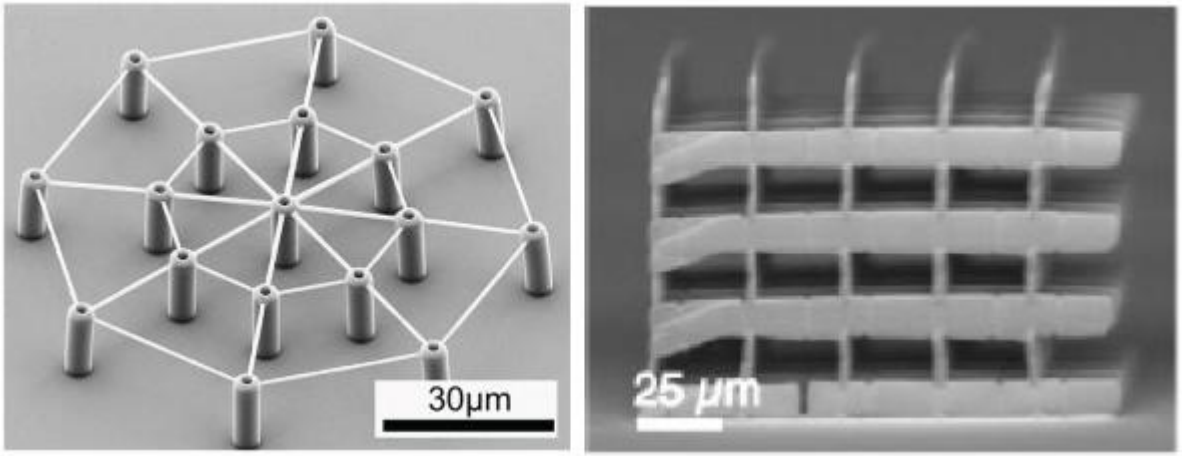

Figure 6 Left: Web structure from Ormocomp resin, used for single cell force measurements[56]. Right: Woodpile structure of acrylate resin, used for cell migration, pore size 12 µm x 25 µm[55]

The ability of the 2PP systems to polymerize a defined volume inside or on the other side of a material not absorbing the near IR light also means it can be used to polymerize resins inside cavities of already assembled microfluidic systems. Until now this feature has only been put to practical use by two research groups. Iosin et al. showed the first example by processing 3D protein structures used as enzymatic reactors inside an already bonded micro chip[81]. The chip consisted of a polydimethylsiloxane (PDMS) top part containing the channels bonded to a glass slide. This simple proof of concept configuration allowed them to construct 3D structures inside the pre sealed chip and ensure easy development of the exposed structures by exchange of fluids in the system. Amato et al. applied a 2PP system to construct a porous filter used to separate micro particles by writing cross-hatched structures inside a commercially available glass chip[82]. The system proved very effective in separating different sized particles, but did however show prolonged and cumbersome pre bake and post processing steps due to the choice of resin and the long and shallow channel design of the chip.

2.1.3. Limitations of two-photon polymerization

2PP is a serial process meaning it cannot easily be up scaled to mass production since the fabrication depends on a single laser beam with a very small spot size. One could apply more lasers or split the beam of a more powerful laser and thus decrease production time, but compared to wafer scale wet or dry etching known from classical micro and nano fabrication 2PP is a slow but still versatile process. The very small spot size and intrinsic ability to create 3D structures means that fabrication of large areas and especially volumes will be overly time-consuming. Since the spot size is very small fast processing speeds depend on effective photoinitiation and cross linking of the resin allowing shorter exposure times and thus faster writing

speeds. To take advantage of the shorter exposure more precise laser control has been developed. Recently systems utilizing galvanometric mirrors for controlling the laser spot have been presented and shown to increase writing speed significantly[83,84]. Yet no mass production or easy up scaling is within reach if structures much larger than 100 µm by 100 µm are wanted. Also the ability to create complex 3D structures has to occur with slower processing speeds due to inertia in the system either in the stage controlling the sample or the laser maneuvering. When accelerating and decelerating the stage in a stage controlled system, such as the Nanoscribe system used in this project, it becomes harder to maintain high resolution as the writing speed exceeds 500 µm/s - 1000 µm/s. The galvanometric scanning systems are better suited to retain precision at high writing speeds, but it will always be a trade off to increase complexity for speed. Though mass production is unlikely the 2PP process does gives some opportunities for lowering costs. Several groups have demonstrated that using the 2PP fabricated structures as molds will deem the 2PP process advantageous for more than just prototyping. Kumi et al. show how the 3D capabilities can be used to create micro channels with arbitrary cross section by using a 2PP structure as a mold[48]. Also more complex 3D structures with overhangs and loops can be replicated by casting soft materials such as PDMS[85,86]. Koroleva et al. have shown that also complex scaffold structures can be replicated[87]. Limitations in the complexity of replicated structures do however mean that only well suited designs are applicable for casting.

2PP delivers unprecedented 3D capabilities and resolution, but is not easy to scale for production of thousands of samples or great areas/volumes. The vast number of photoactive materials applicable with 2PP does however mean that the 2PP technology will find prolonged usage in research fields such as biomedical engineering, micromechanical systems and photonics also in the future. In combination with standard mass production techniques such as photolithography or casting of polymerized structures 2PP can also serve a purpose in specialized production facilities.

2.1.4. 2PP migration constructs presented in this thesis

We find that 2PP scaffolds designed for migration purposes are infrequent and that even fewer, if any, employ feature sizes on or below single cell dimensions. In our effort to mimic the migration environment in the connective tissue as well as the transmigration into the lymphatic vessels, we envision that a variety of pore sizes and 3D topologies of varying complexity are needed to construct a migratory screening platform. Therefore we bring pore sizes down to 5 µm by 5 µm in woodpile scaffolds with 2 stages of increasing complexity added by including barriers to force the cells to change direction in x, y and z inside

the scaffold. We also show a simpler channel structure with varying dimensions to investigate confined migration and compare these findings to the well known migration in 3D fibrillar collagen.

We do this in combination with a state of the art in chip fabrication process that has the advantage of both fast and simple development, made possible with a commercially available chip from ibidi® (µ-Slide Chemotaxis^{3D}) and the low viscosity acrylate resin IP-L 780 from Nanoscribe GmbH. The µ-Slide Chemotaxis^{3D} chip is designed for 3D cell migration studies and thus features a thin bottom suited for microscopy as well as several inlets allowing for easy fluid exchange. By combining more complex 3D structures with improved in chip fabrication schemes I believe our system is a substantial step forward towards introducing the next generation of integrated customizable cell migration platforms. Further discussion of the advantages and limitations of our system will be given in the following sections.

2.2. 2PP setup and in chip fabrication methods

In this section it follows how the 2PP setup works and how the different 3D constructs are prepared.

Methods

Two-photon polymerization was performed on a Nanoscribe Photonic Professional system (Nanoscribe, Eggenstein-Leopoldshafen, Germany). The Nanoscribe system uses a 780 nm Ti-Sapphire laser emitting 150 fs pulses at 100 MHz with a maximum power of 100 mW (20 mW at the sample surface) and is equipped with a 20x, 0.5 NA air objective and a 100x, 1.4 NA oil immersion objective. The substrate is placed in a holder that fits into a piezoelectric x/y/z stage. Holders for various substrates were provided by Nanoscribe, but a custom aluminum adaptor that fits in the 4 inch wafer holder was milled to mount the ibidi chip, see Figure 7. Writing is done by controlling the laser in time and moving the stage with the substrate in x, y and z and hence moving the substrate relatively to the laser focus. All constructs accept where noted otherwise are fabricated from manually written code in the gwl language developed by Nanoscribe. An example of the code used to write a 100x100x70 µm^3 in-chip woodpile construct can be found in Appendix 1.

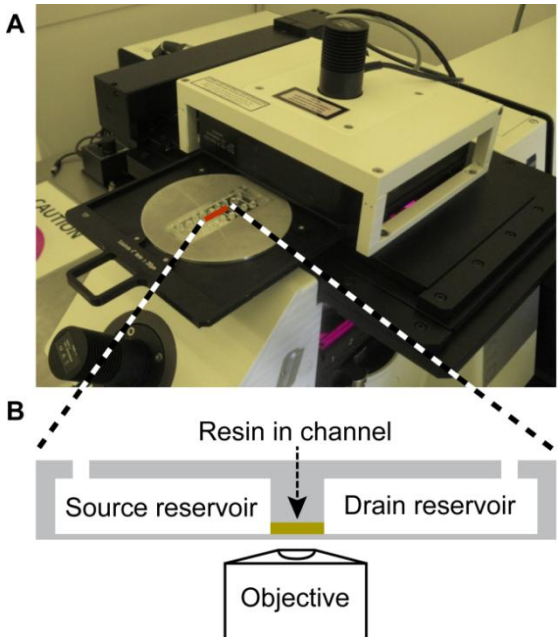

Figure 7 (A) Nanoscribe Photonic Professional two-photon polymerization system with ibidi chip mounted in a custom-made aluminum adaptor. The adaptor fits in the 4 inch wafer holder and is controlled in x/y/z by the piezo stage. (B) Cross section of the ibidi chip used for in chip 2PP showing the reservoirs (65 µL) and channel (<1 µL) geometry with the channel loaded with resin (yellow). The thin chip bottom layer is optimized for microscopy with high NA objectives and thus ideal for high resolution 2PP fabrication adopted from Olsen et al.[88].

A more detailed view of the classical experimental setup can be seen in Figure 8, where the laser is focused in the resin, which has been drop cast on a cover glass. It can also be seen that the voxel is located only in the center of the laser focus and is thus capable of polymerizing any structure or points depending on the stage moving the sample about. In Figure 8 is depicted an immersion objective, but an air objective has also been used. Initial experiments used circular Ø 30 mm x 0.17 mm glass cover slips as substrates in an open system. The cover slips were cleaned with acetone and 2-propanol (both Sigma-Aldrich, St. Louis, MO) before a drop of resin was placed on the top and the substrate was fixed in the holder with 4 drops of Fixogum (Marabu, Tamm, Germany). After exposure the substrates were developed in 2-propanol by submersion in a beaker for 20 minutes and washed with acetone before drying with compressed air. Structures were produced in a liquid acrylate based resin (IP-L 780, Nanoscribe). Writing speeds ranged from 600 µm/s to 1200 µm/s depending on the depth of writing into the resin, see below for optimized recipes. Larger writing depths caused loss of light intensity, and the writing speed was reduced to retain complete cross linking and structural rigidity. All structures were written in order from the largest to the smallest writing depths to minimize refraction of the laser beam from already polymerized structures. Thus, the first layers written are furthest away from the objective and the surface of the substrate. In open systems, this technique requires the initial writing of support pillars and beams in the opposite writing order to prevent polymerized lines of the targeted structure from floating away in the liquid resin. In the

fairly viscous IP-L resin the polymerized lines are only floating away when very long lines are written. Supports structures were not required for in-chip writing since the structure could be anchored both to the channel ceiling and to the channel bottom, thus securing stability during the writing process.

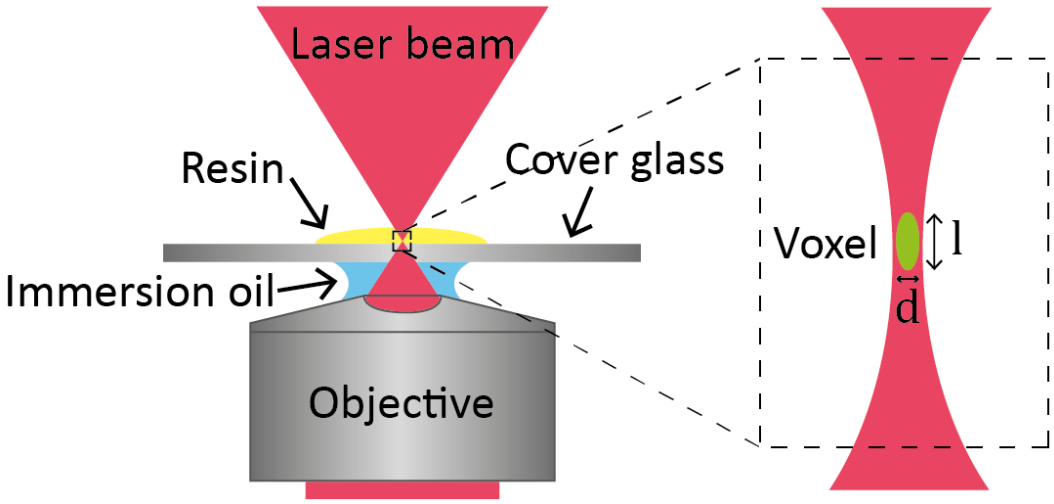

Figure 8 Scheme showing the standard experimental setup in cross section for 2PP with the Nanoscribe Photonic Professional. The laser beam is focused by the immersion objective through the cover glass, mounted on a piezo controlled stage (not shown). Only in the focus of the laser beam, inside the voxel, is the intensity above the threshold value and only here will the resin polymerize. By moving the stage in x, y and z arbitrary 3D features can be constructed.

The polymer chip (µ-Slide Chemotaxis^{3D}, ibidi, Martinsried, Germany) was mounted on the stage via fixation with Fixogum to a custom made aluminum adaptor (see Figure 7A). A drop of resin was placed on one channel inlet for the channel to fill by capillary forces. All inlets were left open during fabrication. Residual resin on the inlet was removed with tissue. Identical writing parameters were used for the chip and the cover glass substrates. To account for the custom aluminum adaptor and the resulting new positions of the defined writing area of the ibidi chip (compared to the standard holders) the sample holder configuration file in the Nanoscribe system folder had to be rewritten. By manually moving the stage to the center of the three channels on the ibidi chip using the 20x air objective we defined three new center positions in which the stage would center. The ibidi holder could then be chosen as any other holder and the system could be programmed to change between the three channels on the chip as if it were 3 different substrates. An initial manual measurement of the channel height was performed via the autofocus system to determine the required structure height to fill the channel. After the auto focus system had established the z position of the channel bottom the top was found by manually focusing on the top and applying the ”find interface” command to precisely determine the z position. The height as observed by the Nanoscribe system could then be calculated and the required structure height be chosen.

Development was done by filling the reservoirs with 2-propanol wait 10 minutes and emptying half of the volume through the channel inlets and the rest through the reservoir inlets. The process was repeated three times. After development, the reservoirs and channels were sterilized by flushing with ethanol in a flow bench, and left to dry for 24 hours.
In some instances the chip reservoirs and 3D scaffolds or channels constructs were surface coated with Poly (ethylene glycol) diacrylate (PEGDA) to increase surface hydrophilicity and ensure complete filling of the channel structures with collagen and avoid bubble formation. The procedure is inspired by earlier work in our group[89]. The chip was wetted with ethanol by filling each reservoir with 65 µl 70/30 % ethanol/water and emptied again. Subsequently 10 mg (10 µmol) PEGDA mw 1 k Da and 0.5 mg (2 µmol) 4-benzoyl benzylamine hydrochloride (CAS 24095-40-7), abbreviated BzA, was dissolved in 1 ml PBS (all from Sigma Aldrich), before 65 µl of the solution was added to each of the two reservoirs in the chip. To aid wetting the photo active solution must be added before the remaining ethanol inside the channel has evaporated and dried out in the 3D structure. All inlets were plugged and the chip was exposed to UV light 15 minutes (32.4 J/cm^2) using a custom built photo reactor with a broad illumination maximum from 330–380 nm (Philips Cleo S-R fluorescent tubes). After exposure the chip was rinsed three times with water. Ultimately the chip was sterilized by flushing with ethanol in a flow bench, and left to dry for 24 hours.

Scanning electron microscopy (SEM) micrographs were obtained with a FEI Quanta 200 ESEM FEG microscope (FEI, Hillsboro, Oregon) at DTU CEN. This allowed us to use the Environmental SEM (ESEM) mode to image insulating materials such as polymers without a metal deposition step.
Confocal micrograph stacks were acquired with a Zeiss LSM 5 microscope (Carl Zeiss, Oberkochen, Germany) with either a 63x, 1.4 NA (numerical aperture) oil immersion objective or a 40x, 1.2 NA water immersion objective, using excitation light at 488 nm and collecting emitted light from 515-550 nm. The recorded stacks were processed into 3D reconstructions using ImageJ[90].

2.2.1. Structure design and optimization of writing parameters

Before the start of this project, it was envisioned that the Schwarz P-surface was the ultimate scaffold unit cell. This is a minimal surface geometry with interconnections in all 3 directions and would allow migration on both the “inside” and the “outside” of the scaffold surface if a hollow design cold be realized, see Figure 9. The complexity of the structure and thus the required writing time with our stage controlled system did however turn our attention towards the simpler woodpile structure comprised of stacked linear rods, see Figure 9. The woodpile structure allows for easy tuning of pore sizes and the p-surface for migration in all

three dimensions, and will thus probe the cells ability to make decisions whether to change direction in x/y or z. The much simpler woodpile structure allows for higher average writing speeds due to long linear stretches, where the maximum writing speed can be sustained longer relative to slower speeds when writing tight corners or stopping and starting. Based on the above arguments it was decided to go forward with woodpile structures as one of the goals was to construct scaffolds spanning several hundred micrometers.

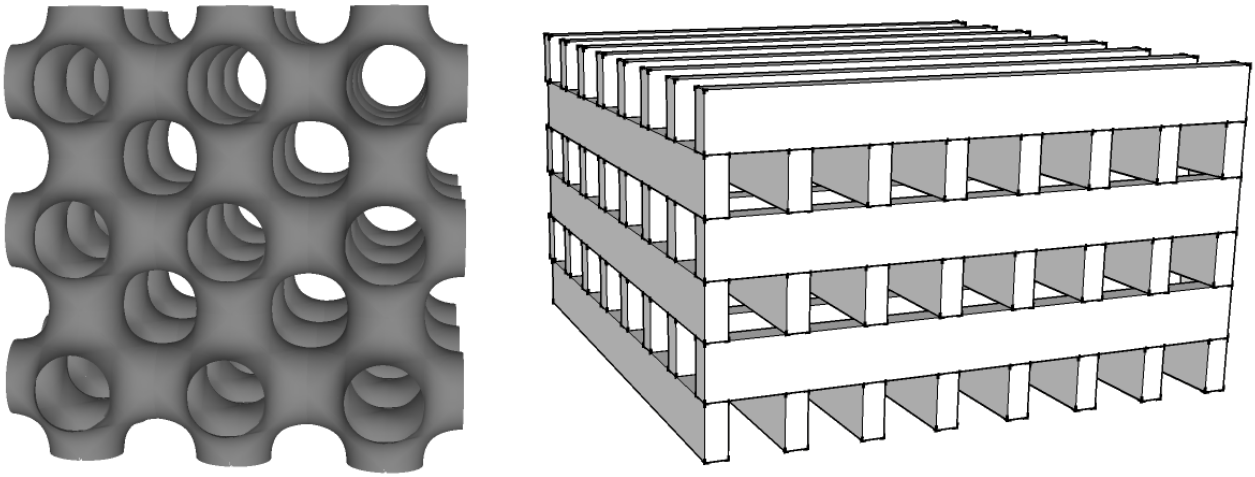

Figure 9 CAD drawings of 2 different scaffold geometries. Left: A scaffold structure based on the symmetric Schwarz P-surface unit cells of 15 µm x 15 µm x 15 µm, pore diameter is thus 7.5 µm. Right: A woodpile structure based on 100 µm x 10 µm x 4 µm beams with a 14 µm pitch, pores here are thus 10 µm x 10 µm, as used in this project.

This project was the first to rely primarily on 2PP for the main fabrication tasks. Therefore the first task was to establish the best suited writing parameters for writing the woodpile scaffolds as fast as possible. Writing speed and line distance in both x/y and z is essential in reducing overall fabrication time. Also dwell time, the amount of time the system waits between each line segment being written, proved to be an important factor to speed up the process. Next writing sequence and laser power to match the various writing speeds also ended up as key to the overall process.

Our system is equipped with a 20x, 0.5 NA air objective and a 100x, 1.4 NA oil immersion objective. Both objectives where initially investigated for optimized writing speeds of the woodpile scaffolds, but the elongated voxel of the 20x objective meant a loss in z resolution that was not tolerable for our application. Therefore only the 100x objective is described here. It now follows how the key parameters were investigated and how the final woodpile recipe came to be.

Update rate/writing speed: The update rate is the frequency in which the stage moves from point to point. Together with the point distance it defines the writing speed as follows: Speed = update rate x point distance. The point distance was kept constant during all experiments at the standard value of 200 nm since all experiments were performed under continuous mode where the stage does not stop between internal points and the laser is always on. Thus the update rate defined the writing speed. A maximum update rate of 6000 (1200 µm/s) was found to be most effective though higher speeds could be achieved, but then considerably thinner lines were observed leading to unstable structures. Later in the process a significant loss in laser power was observed when polymerizing deep inside the resin. This resulted in a need to gradually decrease the update rate to 3000 (600 µm/s) when writing structures up to 70 µm inside the resin.

Line distance x/y: The distance between individual lines when writing polylines. The maximum line distance depends on the voxel width, d_{xy}. The Nanoscribe software language, "gwl", includes a polyline and a meander command which together extend a single line between two points to a number of parallel lines with a defined distance between them, the line distance. This is very effective when many parallel lines are needed to construct a beam. By increasing the line distance the overall number of lines can be reduced. A maximum line distance of 250 µm was found while maintaining structural rigidity.

Z distance, layer distance: The distance between individual layers of the structure. The achievable z distance depends on the voxel length, l, and on how much overlap between layers is needed for a stable structure. A maximum layer distance of 1.3 µm could be achieved without noteworthy loss of stability. To ensure that the individual beams were anchored to the underlying beams an overlap of 1 layer (1.3 µm), half a layer from the top beam and half from the bottom beam was found to be sufficient, see Figure 10.

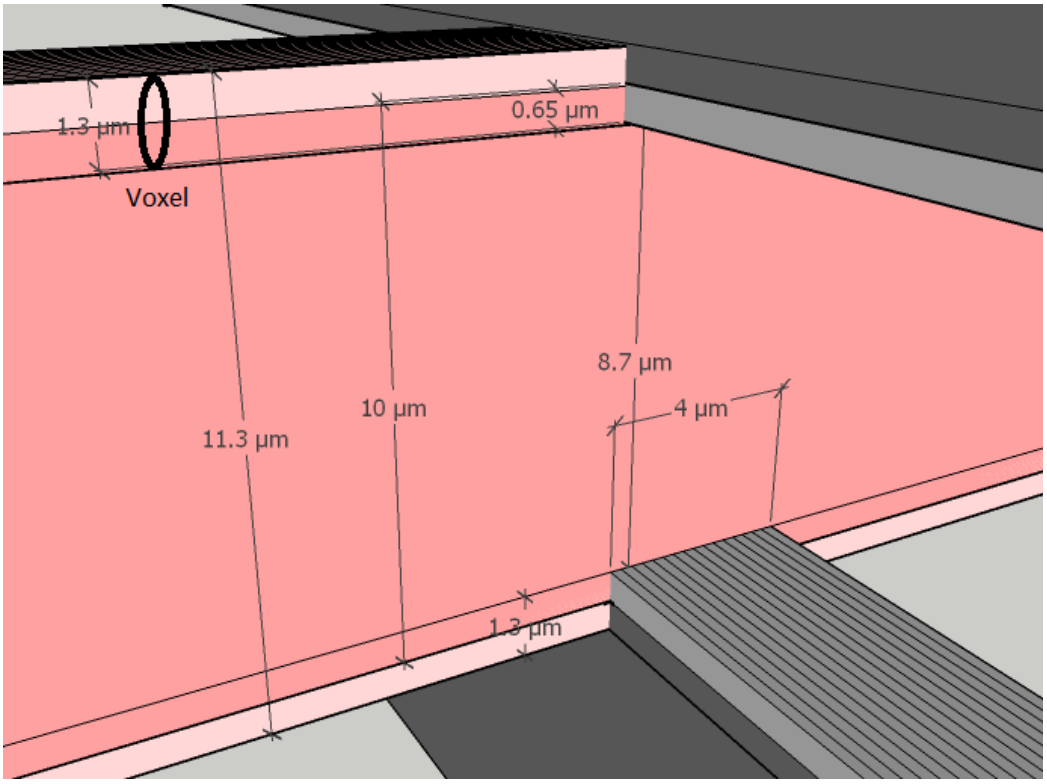

Figure 10 CAD drawing of woodpile beams showing the overlap caused by the voxel length, beams measuring 4x10 µm (dark gray or red) are shown as an example. The voxel length of 1.3 µm and the thickness of the resulting bottom and top layers are shown as well as the 16 individual lines (250 nm lateral separation) making up the width of the beams. The axial length of the voxel (1.3 µm) increases the height of the beams from 10 µm on the CAD drawing by 0.65 µm at both ends (light gray or light red) extending the beam height by a total of 1.3 µm, this extension gives rise to a 1 layer overlap of 1.3 µm, even though the CAD drawing as shown in Figure 9 shows no overlap.

Dwell time: The length of time the system pauses, with the laser off, from a line segment is stopped until the next is started. Even though the woodpile structure consists of many very long lines the standard dwell time of 200 ms meant that half the time the system was waiting instead of writing. It was impossible to observe this with the naked eye but a reduction of the dwell time to 10 ms cut the process time in half. It is important to remember to apply the meander command when reducing dwell time otherwise the stage will not have time to go back to the start of the next line before the laser is started again. This short dwell time can only be used when distances between line ends are short (less than ≈5 µm).

Laser power: The laser power was quickly adjusted to the maximum power that would not cause bubble formation or damage to the structures. A laser power of 80 % was used throughout this work and was found to be optimal for writing in the IP-L resin used here. If smaller features or other chemistries are desired lower power and also slower writing speeds may be necessary, see section 3.4 on 3D structuring of hydrogels.

Writing sequence: The writing sequence is not a parameter per se but it proved important. Two things influenced the writing sequence: 1) the already polymerized resin refracted the laser light due to a changed index of refraction upon polymerization and thus decreased the effective laser power when writing structures deep inside the resin, a kind of shadow effect (Figure 12 D). As a consequence all structures higher than 20 µm had to be written from the top down. 2) Combined with the very long single lines in the woodpile and the viscous resin, meant that the line just polymerized floated away before the subsequent line was polymerized next to the first. To overcome this issue support pillars and beams written from the bottom up had to be incorporated when free standing structures were fabricated on cover glass, see Figure 11 for the writing sequence. Inside the channel of the ibidi chip the top layer was anchored to the ceiling of the channel and thus no support was needed.

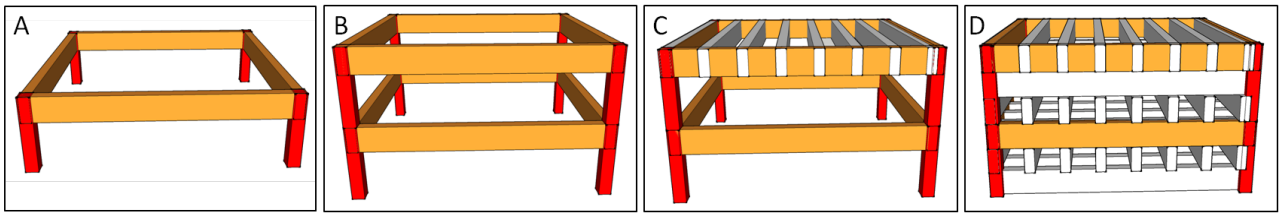

Figure 11 CAD drawing of the writing sequence for woodpile constructs with support structures when writing free standing structures on cover glass. (A) Lower support frame consists of first 4 pillars 5x5x30 µm (red) and then 4 beams 4x10x100 µm (orange). (B) Upper support frame is added identical to the lower one (pillars first then beams). (C) The first layer of the woodpile beams has been added (white) written from the top. They are spanning the support beams to avoid the individual lines floating away. (D) Remaining woodpile beams have been added and the construct is finished.

To determine these parameters test structures in the shape of small “tables” were designed to test whether the parameters would result in stable structures. The table has 2 legs each H x W x L = 4 µm x 10 µm x 4 µm and the table top consist of a single written layer approximately 1.3 µm in thickness, see Figure 12 A. The table top was written with lines perpendicular to the span in order to test the cohesive strength between the individual lines. When a standard line distance of 200 nm are used the single lines can just be distinguished and no apparent weak points can be observed (Figure 12 B), but when speed and line distance is increased to 300 nm the cohesiveness of the table top decreases and a near failure can be seen in Figure 12 C. The table seems to have collapsed which is attributed to the weakened table top. It was found that reducing the line distance to 250 nm was just enough to maintain structural integrity and therefore chosen as the optimal writing condition. The individual lines are visible and the surface roughness is thus increased. If a smoother surface is essential a line distance of 100 nm or below can be recommended, at the cost of a longer fabrication time. The optimized parameters were used to construct

the first woodpiles, see Figure 12 D, where the shadow effect can be observed as the inner beams in the third layer of the woodpile have collapsed due to very poor polymerization. This observation led to the top down writing sequence explained above. Otherwise the woodpile confirmed that a z distance of 1.3 µm and a line distance of 250 nm gave satisfactory structural stability.

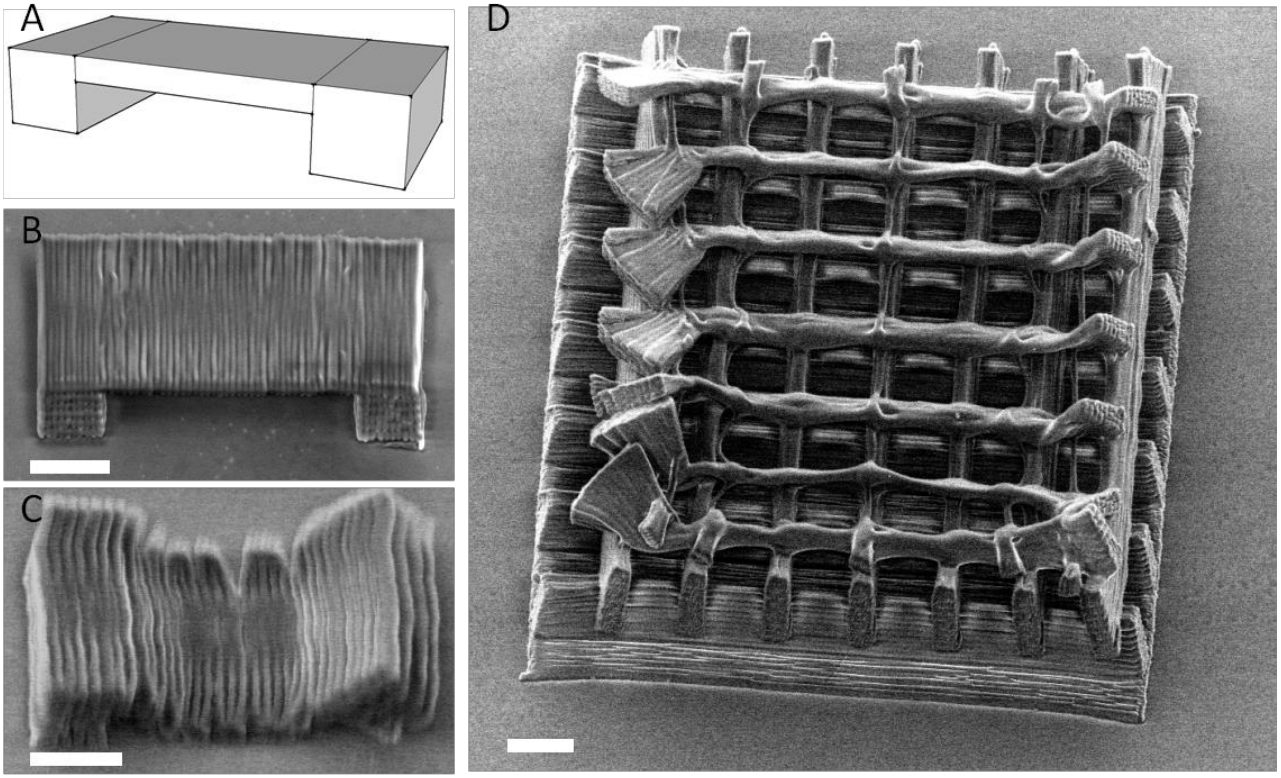

Figure 12 (A) CAD drawing showing the table structure used to optimize parameters, the table has 2 legs each 4 µm x 10 µm x 4 µm spaced 12 µm apart and connected by a single layer approximately 1.3 µm in thickness. (B – D) SEM micrographs of 2PP polymerized structures viewed at 30 degree tilt angle. (B) Table in good condition constructed with the following parameters: Line distance 200 nm, Z distance 0.9 µm, writing speed 600 µm/s. (C) Table showing poor structural integrity. The layer spanning the two legs is clearly on the verge of breaking apart due to an enlarged line distance of 300 nm together with a Z distance of 1.3 µm and a writing speed of 1200 µm/s. (D) Woodpile structure where the third layer in the woodpile is not properly polymerized due to the shadow effect of the underlying layers. The woodpile was written with the optimized parameters: writing speed 1200 µm/s, line distance of 250 nm and a z distance of 1.3 µm. It is clear from D that the bottom 2 layers are sufficiently polymerized, thus the shadow effect is only a problem when woodpiles exceed 20 µm in height. Scale bars are 5 µm in B and C 10 µm in D.

The optimized recipe that was used to write both woodpile and channel structures can be seen in the scheme below. With these parameters the writing time of a 6 layer, 100 µm x 100 µm x 60 µm woodpile, as depicted in Figure 9, was reduced to 45 minutes. There are no considerable changes in the writing time when the design is adjusted to pore sizes of 5 µm, 8 µm 10 µm and 15 µm.

Optimized writing parameters	Value
Update rate (@ structure height)	3000 (60+ µm), 4000 (60-40 µm), 5000 (40-20 µm) and 6000 (20-0 µm)
Line distance x/y	250 nm
Z distance, layer distance	1.3 µm
Dwell time	10 ms
Laser power	80 % (16 mw @ sample)
Writing sequence	Top down (apart from single channel design)

Following the initial optimization experiments, evaluation and visualization of the fabricated structures was done only with confocal microscopy. Confocal microscopy allowed for detailed 3D reconstructions with the possibility to visualize the internal pore structure of the woodpiles, something that, as can be seen in Figure 12 D, can be difficult to distinguish in a SEM image. IP-L is highly auto fluorescent and was easy to image with fluorescein-like settings. Figure 13 shows is a confocal 3D reconstruction of the woodpile above seen from above with a 50x, 0.8 NA air objective.

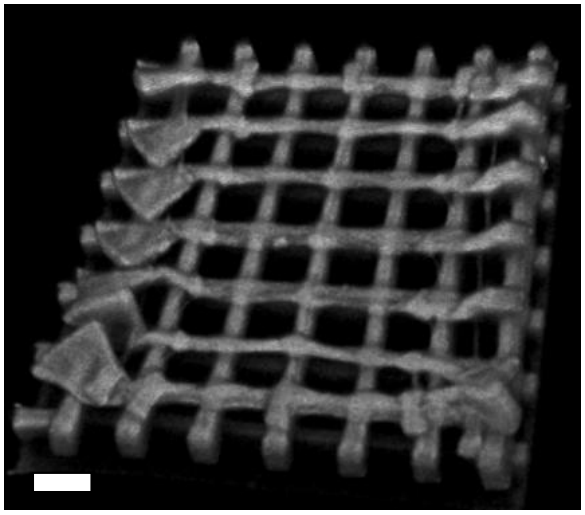

Figure 13 Confocal 3D reconstruction of the same 2PP fabricated woodpile structure displayed in Figure 12. Confocal images of the IP-L structures proved an excellent way to evaluate and visualize them. The shadow effect causing the third layer to collapse is clearly seen. Scale bar is 10 µm.

To further improve the visualization of the internal pore structure we opted to use oil and water immersion objectives as can be seen in Figure 14. Matching the refractive index of the polymer structure with immersion oil lowered the refraction enough to acquire perfect 3D visualization. It was necessary to invert the writing direction from bottom up to top down, and hence it was also necessary to introduce support

pillars and beams to immobilize the individual lines when writing the top layers first. The necessary support structures can be seen as a CAD drawing in Figure 11 and a confocal 3D reconstruction in Figure 14 (A). A cut out of the center of the woodpile for better visualization of the internal pore structure is shown in Figure 14 B. An excellent reproduction of the CAD drawings is presented, thus demonstrating our ability to construct 3D woodpile scaffolds on cover glass substrates.

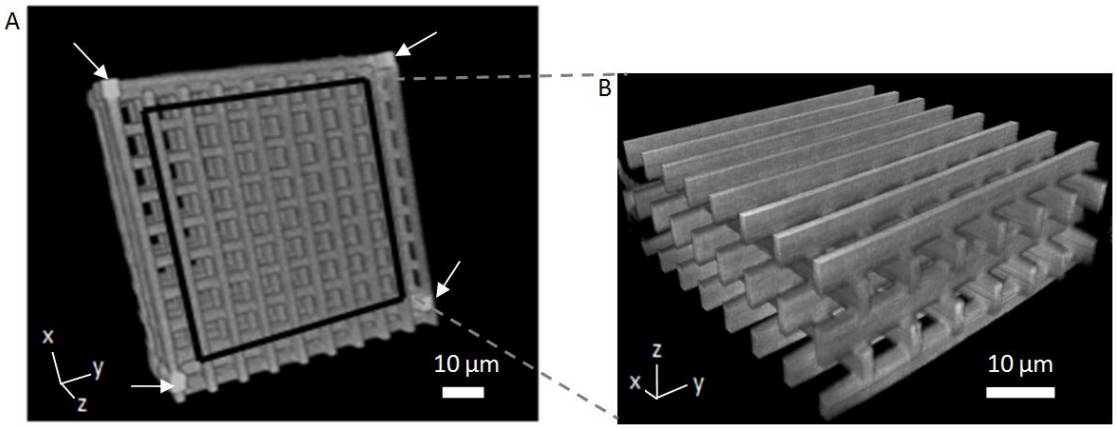

Figure 14 Confocal fluorescence microscopy of a freestanding autoflourescent woodpile structure on a cover glass with pore sizes of 8 x 8 µm in the x, y and z directions. (A) 3D reconstruction of the woodpile construct, confirming a porous 3D structure. Support pillars and beams were added at the corners and around the edges of the structure (pillars marked by white arrows). (B) Reconstruction of the center volume outlined in A.

2.2.2. Cytotoxicity test of polymerized IP-L resin

Cytotoxicity of polymerized IP-L 780 resin was evaluated using a dendritic cell (DC) metabolism assay to ensure no adverse effects originated from the resin. Cytotoxic comparison was made against Tissue Culture grade polystyrene (TCPS) as a non-toxic reference and against PEGDA photopolymerized with the initiator Irgacure 2959, a system that is often used in biomedical applications and in tissue engineering in general and proven to be one of the least cytotoxic[78,91].

Methods

Experiments were performed in a 96 well TCPS microtiter plate (Nunclon grade, Nunc, Roskilde, Denmark). 50 µL IP-L 780 was dispensed into a well and photopolymerized with a dose of 180 mJ/cm^2 at 365 mW in a MA4 mask aligner (Suss Microtec). 50 µL of 1 kDa PEGDA (Laysan Bio, Arab, AL) with 0.1% w/v IrgaCure 2959 (2-Hydroxy-4'-(2-hydroxyethoxy)-2-methylpropiophenone, CAS 106797-53-9, Sigma-Aldrich) was dispensed into a second well and photopolymerized with 8.6 J/cm^2 using the mask aligner. The latter high

exposure dose was required due to the presence of ambient oxygen acting as a radical quencher. A third untreated well was used as the non-toxic TCPS reference. Samples were prepared in triplicate on each plate.

All wells were washed three times with MilliQ grade water (Merck Millipore, Billerica, MA) and left with MilliQ water for a further 72 hours at room temperature. Culture medium consisted of IMDM with 1% penicillin / streptomycin (P/S) and 10 % Fetal Bovine Serum (FBS) from Invitrogen (Life Technologies, Paisley, UK). The wells were filled with culture medium for 15 minutes and emptied, prior to seeding 5000 – 10000 DCs in 100 µl culture medium in each well and incubation for 24 hours. The number of cells used in each experiment was constant but varied with the number of cells in the provided vials from Herlev Hospital between experiments, since the assay measures the relative metabolism an individual cell count was not performed. 10 µl AlamarBlue (Life Technologies) was added to each well and incubation was continued for 2 hours. After incubation 100 µl supernatant was transferred to a new microtiter plate, and the developed color was measured in a Victor3 plate reader (Perkin Elmer, Waltham, MA).

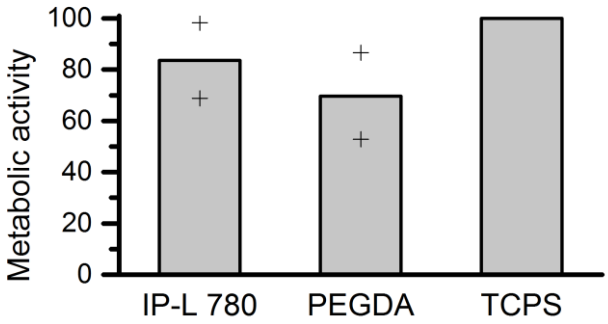

Figure 15 Metabolic activity of dendritic cells cultured on different materials. Tests are performed with an AlamarBlue assay and the graph shows the activity relative to the metabolic activity on TCPS. Values are the average of two independent experiments shown with marks. The values for the TCPS are normalized for each experiment.

The TCPS well bottom was chosen as reference material for the DC metabolic activity on the two photopolymerized materials. Figure 15 shows that photopolymerized IP-L 780 induces some reduction in DC metabolism compared to TCPS, but a smaller reduction than observed on the commonly used PEGDA/Irgacure 2959 system. These results were obtained on 1.5 mm thick material layers coating the entire well bottom. Considering the extremely small volumes of photopolymerized material in the in-chip constructs as well as an efficient washing process we do not anticipate significant cytotoxic effects. Cell functional assays supported this assumption by showing indistinguishable migration behavior of DCs loaded in channels with or without a fabricated IP-L construct.

2.2.3. 2PP migration scaffolds inside a commercially available polymer chip

Because the near IR laser will not be absorbed by common polymer materials, 2PP allows for polymerization of liquid resins inside already assembled and bonded microfluidic channels. Here we use a polyethylene based chip from ibidi called µ-Slide Chemotaxis^{3D}. It is purpose built for 3D migration chemotaxis studies in collagen and includes two 65 µl reservoirs divided by a 1 mm wide and only 70 µm high channel in which the migration is observed. In the photograph in Figure 16 the channel is highlighted with a black dashed line and the reservoirs with a white dashed line. Each single reservoir and the channel have two inlets giving six in all and allowing for fast and easy liquid exchange. A schematic of the chip in profile and the mounting position in the Nanoscribe 2PP system can be seen in Figure 7, page 17.

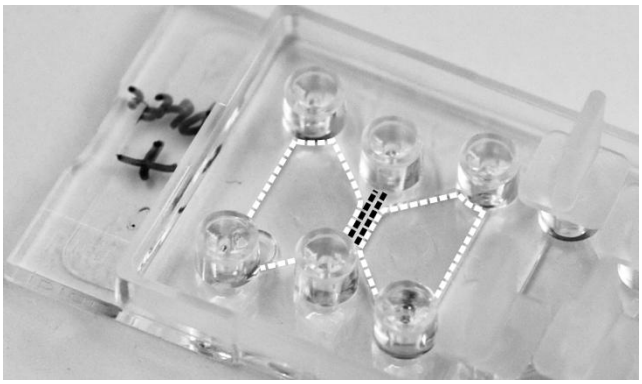

Figure 16 Photograph of the ibidi µ-Slide Chemotaxis^{3D} chip (76 mm x 25 mm) used as platform for two-photon polymerization of cell-sized 3D microstructures in the center channel (black dashed lines) between chemoattractant-containing and –free reservoirs (white dashed areas), adopted from Olsen et al.[88].

Most microfluidic chips designed for in-chip high resolution optical microscopy can be used as substrates for in-chip 2PP fabrication. The thin bottom layer and the two reservoirs situated next to the channel in the ibidi chip is a particularly favorable design, see Figure 16. The two reservoirs with a total volume of 130 µl in close proximity to a total channel volume of ≈1 µl facilitate fast diffusion based development due to a very short diffusion distance of only 0.5 mm. Development times are further reduced by pressure-driven and thermal convection effects during the filling and emptying of the reservoirs. The closed microchannel system uses very small volumes (few µl) of costly resins and optional biomolecular additives compared to open systems. For chemotaxis analysis, the closed chip system is reported by ibidi to sustain a controlled linear concentration gradient in solution for up to 48h with a better control of the observed gradient than in previously reported open systems written by 2PP[55,76]. The chemoattractant concentration gradient is established in the middle channel section with dimensions of W x L x H = 1 mm x 2 mm x 70 µm. Writing a

woodpile structure of this size is obviously not possible given the writing parameters discussed above, as it would mean a total fabrication time of several days for one channel. We therefore chose to reduce the writing time by fabricating a construct of smaller outer dimensions positioned in the middle of the channel. The easy fluid exchange in this chip combined with the use of a liquid resin meant that loading and development is achieved within minutes. The only previously reported similar procedure includes pre-exposure soft baking steps and cumbersome development in long closed channel systems where loading and development thus tally to hours and days[82] instead of minutes.

2.2.4. Gradient stability in ibidi chip and inside woodpile construct

To establish whether the gradient formed inside the channel in the ibidi chip was actually stable for longer periods of time we did a time lapse experiment showing the gradient formation and stability. We used a chip with a collagen filled channel and loaded 0.1 mg/ml rhodamine-marked Streptavidin (Sigma Aldrich) in Phosphate buffered saline (PBS) (Sigma Aldrich) in one reservoir and pure PBS in the other reservoir. We then monitored the fluorescence intensity with the same Zeiss LSM 5 confocal microscope as used for 3D reconstructions of the 2PP constructs, with a 5x, 0.3 NA objective. This objective is able to image the entire channel width as can be seen in Figure 17, and is thus perfect for observing the cross channel gradient.

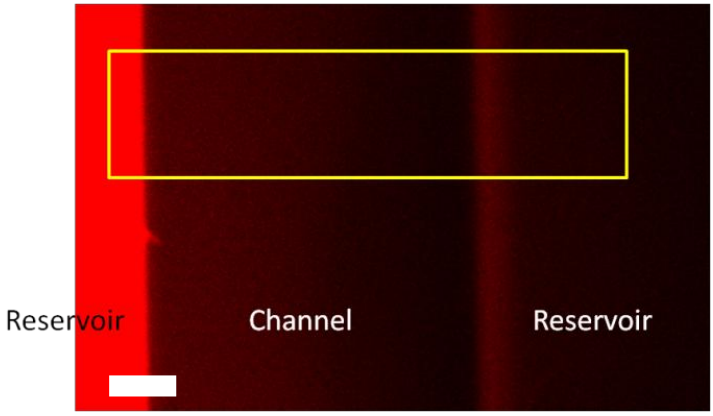

Figure 17 Confocal micrograph (5X, 0.3 NA) of a collagen filled ibidi channel 2 hours after addition of 0.1 mg/ml rhodamin marked streptavidin in PBS in the left reservoir and PBS in the sink reservoir. The yellow rectangle shows the area used for analyzing the concentration variation across the channel. It can be observed that a gradient has formed from left to right. The height of the reservoirs (400 µm) compared to the shallow channel (70 µm) increases the observed intensity causing the overexposure of the detector in the source reservoir and the slight increase in intensity just after the edge of the drain reservoir. Scale bar is 200 µm.

As Figure 18 shows, the gradient in the ibidi channel was stable for at least 42 hours after loading of 0.1 mg/ml streptavidin. The gradient slope was also stable up to 42 hours, though the overall concentration seemed to increase a little. This could be an artifact from the image acquisition, since it was not trivial to maintain the exact same focus and acquisition conditions when reloading and focusing on the sample multiple times. Our data supports a long term stable gradient in the ibidi channel in agreement with the 48 hours stability claimed by ibidi[92].

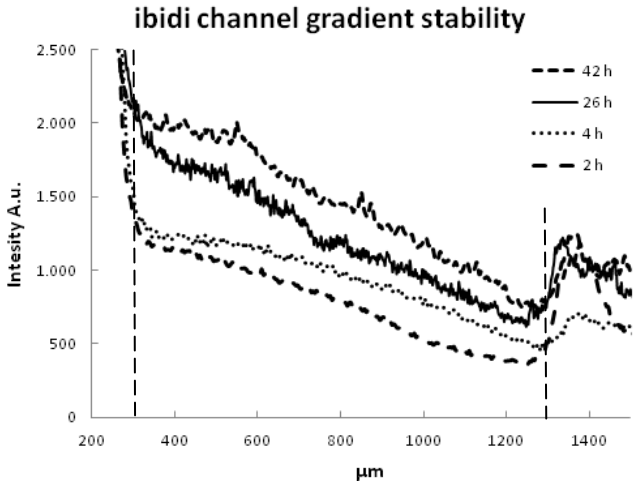

Figure 18 Graph showing excellent stability of a streptavidin gradient in a collagen (1.61 mg/ml) filled ibidi channel for up to 42 hours. The source image for the profile at 2 hours is shown In Figure 17. The intensity has been scaled for visual purposes. The intensities decrease in the far right after the slight increase at the channel/drain interface to a level comparable to the lowest channel level, indicating a very low concentration of streptavidin in the right side of the channel, even after 42 hours. Dashed vertical lines indicate approximate channel boundaries.

After having established that the gradient inside the ibidi channel was stable over long times it was calculated if the introduction of a woodpile scaffold would drastically affect the gradient formation and if the gradient was timely formed inside the construct. The diffusivity of a compound A in a medium B can be written as D_{AB}. The diffusibility, Q, in a porous medium is then the ratio of the effective diffusivity, D_{eff}, of compound A through the porous medium to D_{AB}[93]. van Brakel and Heertjes expressed the diffusibility as:

$$\boldsymbol{Q = \frac{\varepsilon\delta}{\tau^2}}$$

where ε is the porosity, δ the constrictivity, and τ the tortuosity[94]. The tortuosity τ is close to unity in the woodpile design since the straight channels of the construct are parallel to the gradient direction being created inside the construct. The porosity is 0.71 for a perfect woodpile structure with 10 µm x10 µm pores

separated by bars of cross-sectional dimensions 10 µm x 4 µm. The introduction of a 1.3 µm vertical overlap between overlying bars to optimize the mechanical stability reduces the porosity slightly to a value no smaller than 0.68. The constrictivity cannot be calculated directly. However, van Brakel and Heertjes estimated that the constrictivity does not depend on the particular shape of the porous structure, but only on the ratio β between the maximum and minimum cross-sectional dimension of the porous path through the construct. For our woodpile design $\beta \approx 2$ corresponding to a constrictivity of approximately 0.9[94]. Inserting these values into the expression for the diffusibiilty yields:

$$Q = \frac{0.68 \cdot 0.9}{1^2} = 0.61$$

The results show that the effective diffusion constant is reduced by <50% inside the construct compared to outside with a corresponding small delay in establishing a chemoattractant concentration gradient within the construct. However, the lateral extent of the construct is only up to 20% (200 µm) of the entire channel extent (1 mm) in the direction of the concentration gradient. This implies that the delay in gradient formation inside the construct will be insignificant in comparison to the establishment of the channel-wide concentration gradient and the total duration of the migration experiments being between 24 and 48 hours.

2.3. In chip 2PP cell migration constructs

In this section the different in-chip migration constructs fabricated with the IP-L resin are presented.

2.3.1. Woodpile scaffolds

Pore dimensions of 5x5 µm, 8x8 µm, 10x10 µm and 15x15 µm were fabricated, see Figure 19, to ensure a range of pore sizes spanning from below a single cell dimension to above. Dendritic cells have been reported to have cross sections in the range of 7-8 µm in a 3D environment[95], however we observed elongated and clearly squeezed cells in channels with a cross section of 10x10 µm, which would indicate that the cells used here are even larger. Since it was impossible within a reasonable timeframe to fill the channel with one big woodpile the minimum construct dimensions were given by three requirements: (a) A substantial number of cells should traverse the porous construct instead of migrating around the construct (minimum length); (b) No cells should be able to sense both ends of the construct with their

dendrites simultaneously (minimum width); (c) Cells should not be able to migrate above or below the construct (full channel height).

By positioning three or four 100 µm x 100 µm woodpiles next to each other, see Figure 19, we gained length substantial enough to guide many cells through the scaffolds instead of around. After a few experiments it was found that the DCs did not migrate through the 5 µm pores in substantial numbers to allow statistical analysis, which is why some of the experiments were done without the 5 µm pore woodpile scaffold. The biological relevance of migration analysis constructs with widths on the 100 µm length scale is supported by a recent publication showing oriented motion of murine dendritic cells only within the nearest 100 µm of chemokine-secreting lymphatic vessels[96].

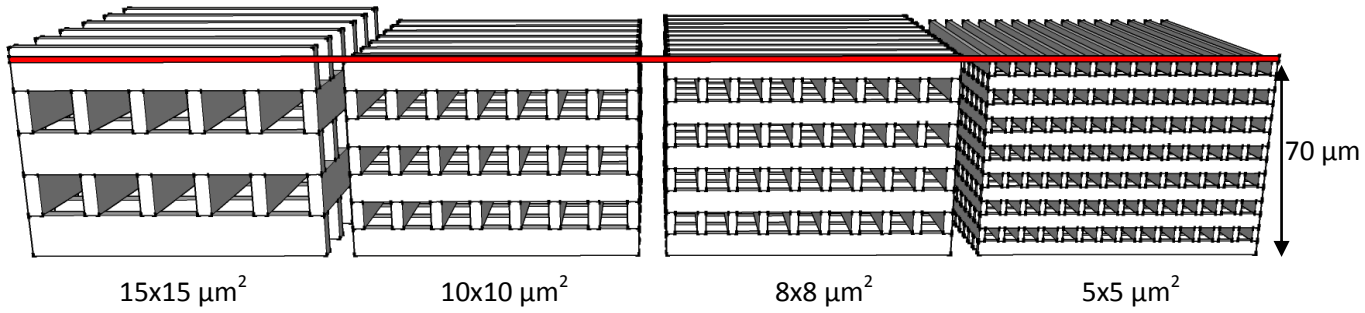

Figure 19 CAD drawing of the four different woodpile scaffolds used for in chip migration studies. All four constructs have approximate dimensions of L x W x H = 100 µm x 100 µm x 70 µm in height. By adjusting the number of layers the height was fitted to the measured channel height to ensure no cells squeeze below or above the construct. The red line indicates 70 µm and shows that all 4 constructs will fill the entire channel.

The number of layers in the woodpiles was adjusted individually to fill the channel from top to bottom to ensure that no cells could migrate above or below the construct. A variation in channel height between 55 µm and 75 µm was observed between ibidi chip batch numbers and at different positions on the chip, wherefore no constant construct height could be established. To further challenge the navigating skills of the cells and make them actively decide to enter the 3D scaffold we designed the bottom layer perpendicular to the chemokine concentration gradient in order to avoid cell migrating in a 2D like environment at the bottom of the channel.

Complete development of in-channel woodpile constructs was verified by standard fluorescence microscopy and confocal 3D reconstructions. To allow for standard fluorescence microscopy a CO_2 laser (FH Flyer, Synrad, Mukilteo, WA) was used for sectioning a chip next to the woodpile construct to provide optical access. Figure 20 shows fluorescence micrographs of an in-channel woodpile construct in front and

bottom view and a confocal 3D reconstruction all confirming the presence of a continuous porous structure from channel top to bottom in all woodpile constructs.

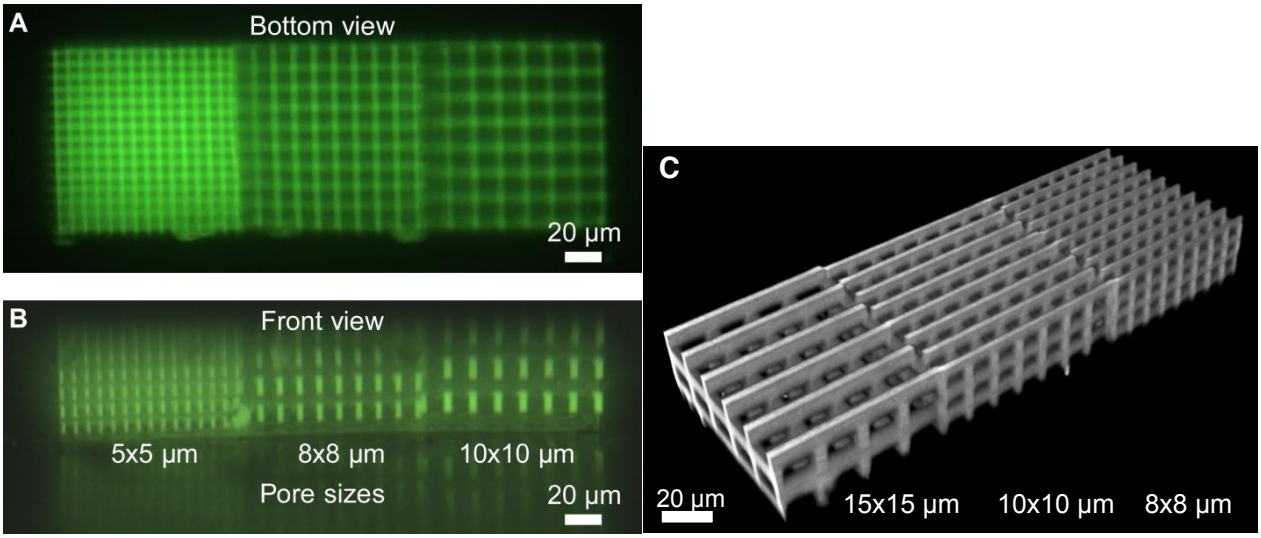

Figure 20 Fluorescence micrographs (A and B) of a woodpile construct in an ibidi channel shown in (A) top view and (B) side view after cell analysis and regeneration with collagenase. Each construct consists of three 100 x 100 x 70 μm^3 volumes with 5x5 μm^2, 8x8 μm^2, and 10x10 μm^2 pore sizes respectively. A reflection in the channel bottom is seen in the front view image. A and B are adopted from Olsen et al.[88]. (C) A confocal 3D reconstruction of in-channel woodpile constructs with pore sizes of 15x15 μm^2, 10x10 μm^2 and 8x8 μm^2 respectively. A clear internal pore structure is observed, confirming that in-channel constructs are comparable to constructs fabricated on cover glass substrates. These constructs have been used repeatedly for migration experiments and subsequently undergone collagenase regeneration without observable damage.

The basic woodpile topology described above permits direct cell migration from the front to the back of the construct with no need for turning. If a cell wants to turn it will, due to the woodpile geometry, need to change its vertical level in advance in order to reach a channel in the perpendicular orientation. By introducing barriers blocking the straight path through the constructs by one additional photopolymerized barrier per channel at alternating positions in neighboring channels, we force all migrating cells to perform at 3D spiral turn at least twice. When the cell encounters a barrier as it follows the increasing chemokine concentration it will need to change level, then move sideways and then finally change level again before it can continue its forward movement. The alternating barrier positions assure this spiral turns are needed twice to traverse the construct. The barriers measure 2 µm in thickness and overlap the inside wall of the woodpile beam with 2 µm on each side to ensure stability. The top and the bottom of the barrier both have the 1.3 µm overlap with the perpendicular beams, identical to the layer overlap in the woodpile construct, see Figure 10. Figure 21 A shows a CAD drawing of the woodpiles with barriers in perspective and in side view. The basic woodpile structure is shown in gray, while the additional barriers present in all

three layers are highlighted in dark green. The side view shows the barrier-free passage ways for cells in the three layers with sideway channels. The outer dimensions of the construct are increased to L x W x H = 400 µm x 200 µm x 70 µm to provide longer and more detailed analysis of the migration path of the individual cells and force a higher number of cells through the scaffold.

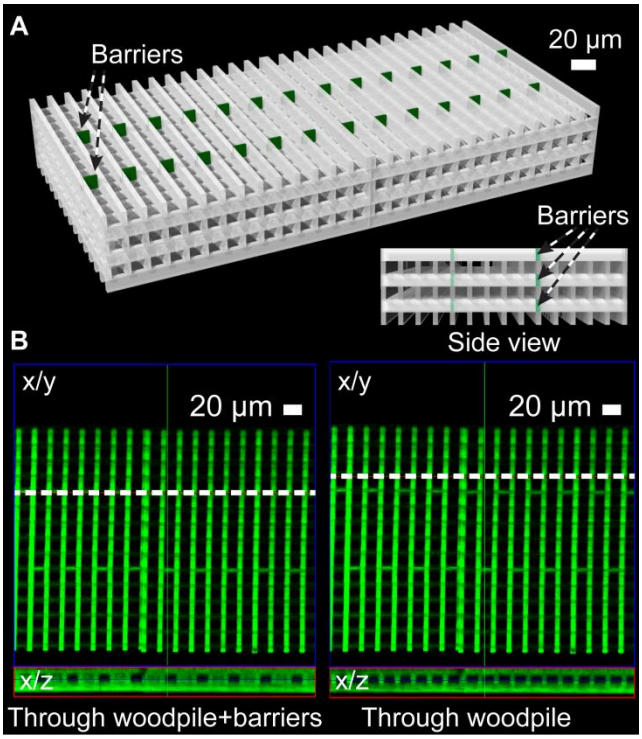

Figure 21 Higher complexity 3D cell migration construct. (A) Schematic of the construct highlighting in green the additional barriers introduced to obstruct cell migration straight through the construct (from front to back). Insert: Construct in side view showing the free passage ways in the perpendicular direction. (B) Confocal fluorescence micrograph of the construct fabricated by 2PP, focusing on the lower three layers. Left: Orthogonal slice through the barriers (along dashed line in x/y projection) showing blockage of every second front-to-back channel in the x/z projection. Right: Slice through the basic woodpile showing all channels being open at these locations. From Olsen et al.[88].

We selected the 10x10 µm pore size for the higher complexity construct and also fabricated enlarged standard woodpile constructs to compare migration behavior when the cells are forced to move 200 µm and change direction in both lateral and vertical dimensions. Figure 21 B shows a confocal fluorescence micrograph of one of the layers containing extra barriers in the final in-chip produced construct. Cross-sectional views (x/z) through the layer (x/y) show either the added barriers blocking every second channel or open channels depending on the y position of the cross-section, confirming that the cells need to do 2 spiral turns to traverse the construct.

2.3.2. Mix and match

Ideally, all cells should be forced to migrate through the construct. We tried to achieve this by a "mix-and-match" combination of 2PP fabrication of the 3D micro structured construct followed by conventional 2D patterned exposure through a shadow mask in a mask aligner to polymerize bulk barriers leading up to the construct. IP-L, as already discussed, changes its refractive index upon polymerization and is thus easy to visualize directly after polymerization, thereby allowing us to align the barrier structures precisely to the already polymerized woodpile scaffolds and only develop the construct at the end.

Methods

In brief, the in-chip construct was exposed as already described but without development of the structure, i.e. unexposed IP-L 780 resin remained in the chip channel. The bulk barriers were designed as open areas in a standard photolithography chrome-on-glass shadow mask. The resin-loaded chip was mounted in a Suss MA4 mask aligner (Süss Microtec, Garching, Germany) where the bulk barrier outlines on the shadow mask were aligned to the visible polymerized construct in the resin. The bulk barrier areas were exposed to a dose of 300 mJ/cm^2 at 365 nm, followed by simultaneous development of both construct and bulk barriers according to the procedure previously described.

The bulk barriers effectively blocked the remaining channel volume next to the construct and would force the cells to migrate through the construct, see Figure 22. Unfortunately, the cells showed very limited or unusual migration behavior that was interpreted as being caused by released cytotoxic compounds from the bulk barriers. It is believed that the large bulk polymerized IP-L barriers meant that either unpolymerized monomers or still active photo initiators might continously be released from the bulk. Since the development procedure was not optimized for removing umpolymerized reagents from the bulk polymerized volumes it led to a cytotoxic effect not previously observed with the 2PP constructs alone. We chose not to explore the use of bulk barriers further since the cell analysis could be performed with statistical significance on the fraction of cells migrating through the construct in the absence of bulk barriers.

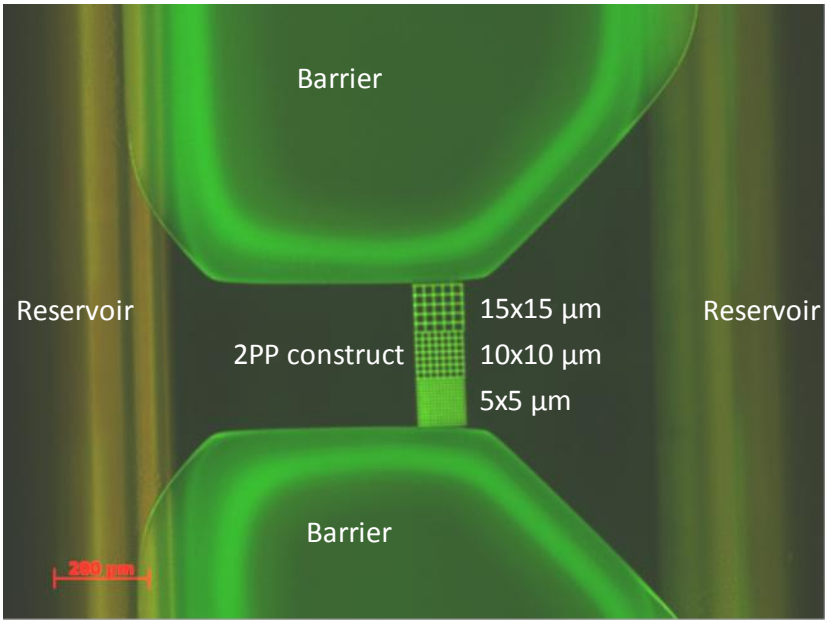

Figure 22 Fluorescence micrograph of 2PP woodpile construct with pore sizes of 5x5 μm^2, 10x10 μm^2 and 15x15 μm^2 inside the ibidi channel with bulk barriers blocking the remaining channel and inlets. The cells were thus forced to enter the construct from the right in order to migrate from one reservoir to the other adopted from Olsen et al.[88].

2.3.3. Channel constructs

To further investigate cell migratory behavior it was decided to design linear channel constructs. Cells have been shown to change morphology and migration mechanism when confined in 2 dimensions[97,98]. We believe that a major advantage of our system is the ability to observe migration simultaneously in a random 3D collagen matrix and inside a micro fabricated construct. In the following, the fabrication of channel structures of various kinds is presented. Initially it was envisioned that we could determine the height in which the individual cells migrated through the constructs by designing simple multilayer channel constructs as shown in Figure 23 with barriers completely blocking specific entrances, and thus deduct which height they entered the construct from and which channel they migrated through. Refraction from the separation layers limited the visibility through the construct and made it impossible to track the cells. Therefore only the single channel design shown in Figure 23 was used for migration studies.

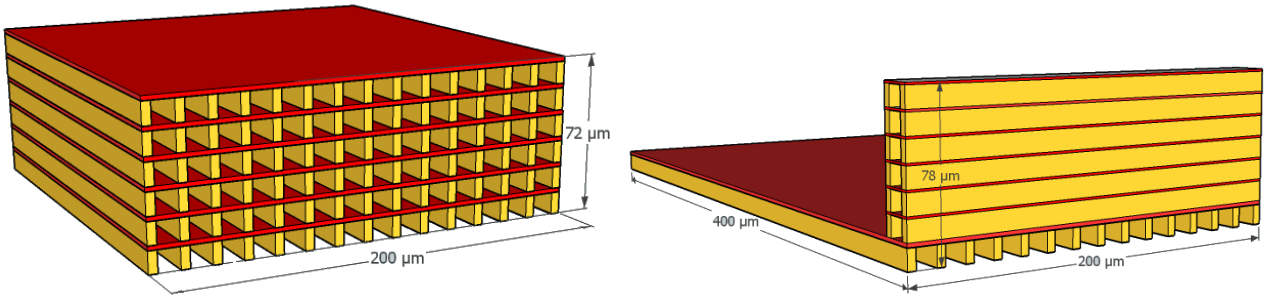

Figure 23 CAD drawings of 3D channel construct designs**.** Left: Multilayer channels design that proved not fit for use due to refraction from the separating layers (red) limiting the visibility through the construct and thus rendering tracking of the cells inside the construct impossible. Right: Single channel design with 10x10 µm channels of length 400 µm closed by a lid (red) and a wall permitting the cells going over the construct.

Single channel construct designs with channel dimensions of 10x10 µm, 15x15 µm and 20x20 µm were fabricated. Also lengths of both 200 µm and 400 µm were made. A wall at the beginning of the channels was incorporated to prevent the cells from just migrating over the channels. It consisted of two rods 10x4 µm in cross section and 200 µm wide (yellow) placed 10 µm apart with a horizontal separation layer (red) of 1.3 µm thickness to stabilize the wall every 10 µm in height. For the 10 µm and 15 µm channels a horizontal lid (red) of only one written layer (1.3 µm thickness) was stable enough to span the rods and close the channels. When the channel width was increased to 20 µm a lid of three written layers (3.9 µm) was needed to maintain a stable structure. The critical moment where a collapse is most likely is assumed to be upon evaporation of the last remaining fluids in the channels after development. A substantial surface tension induced stress is believed to be the cause of the observed collapse of the 20 µm spans when only one layer was used. When fabricating structures larger than 300 µm by 300 µm it is necessary to stitch together structures due to the limited range of the piezo stage of the Nanoscribe equipment. Therefore an intersection can be observed in Figure 24 where the two halves of the channels are stitched together with the help of the less precise motorized stage. The construct depicted in Figure 24 has the exact dimensions of the single channel CAD design shown in Figure 23.

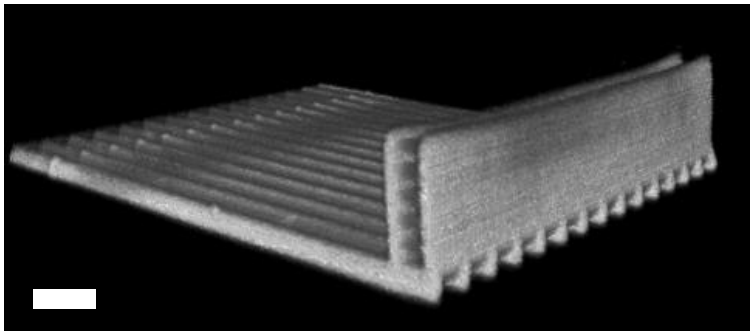

Figure 24 Confocal 3D reconstruction of a single channel construct with channels measuring 10x10x400 µm. Only approximately 220 µm of the construct length can be seen due to the limited viewfield of the objective. The separation layers positioned every 10 µm can be observed in the wall, which is also only shown in part. Scale bar is 20 µm.

2.3.4. 2PP based on 3D CAD files

In the course of this project it was also evaluated how the Nanoscribe system and the included software package, especially the Nanoslicer, performed when given the task to write true arbitrary 3D shapes from stl-format 3D files. The Nanoslicer works as the name suggests by slicing the 3D geometry at a defined interval, similar to other 3D printing software. It outputs a solid file where the whole interior of the geometry is completely cross linked, a contour file where only the contour lines are cross linked and a combined file where both are featured. Several adjustments had to be made to the recipe optimized for woodpile and channel constructs in order to allow for higher complexity writing tasks. The writing speed was reduced to 200 µm/s, the laser power reduced to 70 %, and the layer distance reduced to 0.5 µm for enhanced resolution. The three objects shown below in Figure 25 were written from the bottom up to ensure adhesion to the substrate and clearly illustrate the true capabilities of the 2PP technique. The Lego brick and the x-wing fighter in Figure 25 A and B respectively were written from the combined file, meaning both the contour and the center of the constructs are polymerized, still one layer at a time. The diamond lattice in Figure 25 C is written only from the contour file, which results in the hollow structures as seen in the top of the construct. By only writing the contours of an object, one can significantly reduce the required writing time. Even though only the contour was written of the diamond lattice the complexity of the geometry would give writing times two to three times longer compared to a similar sized woodpile construct. We did consider only writing the contours of the woodpile constructs, but the mechanical stability of the structures would have been compromised.

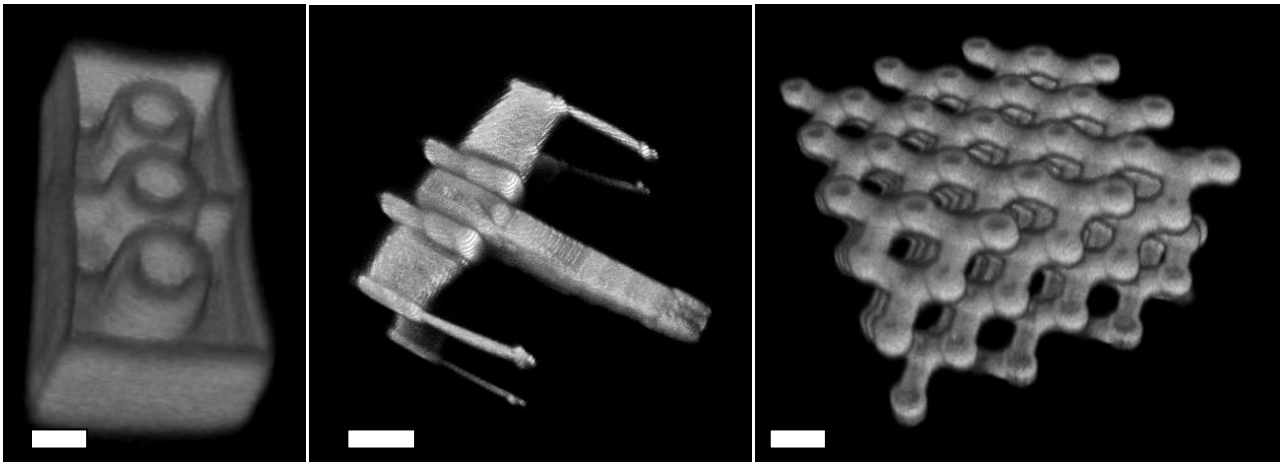

Figure 25 Confocal 3D reconstructions of 2PP fabricated 3D figures. (A) A standard (2 by 8) Lego brick measuring (LxWxH) 32 x 16 x 12 µm. (B) X-wing fighter measuring (LxWxH) 46 x 40 x 14µm. (C) Diamond lattice construct measuring (LxWxH) 64 x 64 x 42 µm, with a 10 µm pore size. Scale bars:(A) 5µm, (B) and (C) 10 µm.

2.4. In chip migration studies

The migration studies presented in the following are done almost exclusively by Gertrud Malene Hjortø. The cells used are mature dendritic cells provided by Morten Hansen and Özcan Met at Herlev University Hospital. Briefly the dendritic cells result from extraction of monocytes from blood of healthy donors, followed by differentiation and maturation to mature dendritic cells. The techniques involved in extraction and maturation as detailed in earlier work will not be discussed here[1,2,4,99,100]. Cell handling protocols as performed at Herlev University Hospital and by Gertrud Malene Hjortø can be found in Olsen et al.[88] and in Appendix 1.

2.4.1. Migration through Woodpiles constructs

Mature dendritic cells suspended in collagen were seeded in the sink reservoir and 60 ng/ml of the chemoattractant CCL21 was filled in the source reservoir of the ibidi chip. The collagen gel acts as a natural biological environment mimicking the in vivo extracellular matrix and aiding migration via adhesion sites and physical support. A stable gradient is formed across the whole channel width and inside the woodpile constructs as discussed above. Mature dendritic cells express the receptor CCR7 that recognizes CCL21, which *in vivo* is secreted by the lymphatic vessels and as such acts as a primary homing signal and is vital in the adaptive immune response. Here we analyze the DCs ability to transmigrate through collagen filled

woodpile constructs with varying pore sizes in order to assess the effect of confinements and pore sizes in 3 dimensions. This will attempt to mimic the squeezing and navigation necessary when the DCs are homing to the lymph nodes through the different environments encountered in vivo. Woodpile constructs with pore sizes of only 5 µm saw very few transmigrating cells and is not included in the results, due to a lack of statistical relevance.

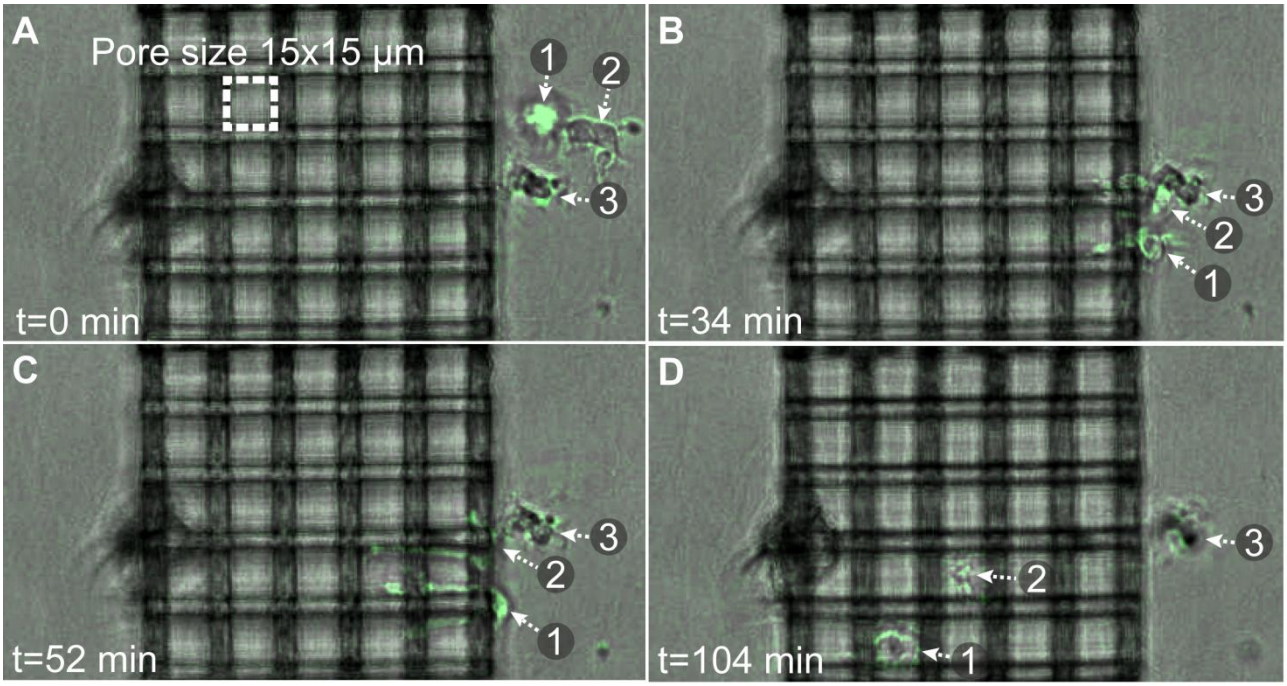

Figure 26 Phase contrast microscopy snapshots (bottom view) showing two dendritic cells (labeled "1" and "2") migrating inside a 15 x 15 µm pore size woodpile construct. Both cells probe neighboring channels in (B) and (C), before deciding on a channel to migrate through in (D). Direct link to movies: http://web-files.ait.dtu.dk/maol/Woodpile_movies.zip. The cell outlines have been highlighted in green by use of image processing in ImageJ[90].

Time-lapse analysis was used to determine the number of turns the cells performed during the transmigration of the woodpile constructs. In Figure 26 two cells are seen migrating through a 15 µm woodpile construct, first a decision has to be made to which pore to go through. When a channel is chosen transmigration begins and in this case no turns are observed. The gradient is established along the channels and will thus not in itself encourage the cells to change channels. It is therefore only the physical confinement of the cells and the sheer option to make the turn that will influence the number of turns made. The number of turns made by the individual cells were counted and compared in Figure 27 and Figure 28. First the number of cells going straight through the construct was compared to the number of cells making one or more turns, Figure 27. A turn is counted as a 90 degree turn in the x/y plane, due to a lack of depth perception inside the scaffolds the inevitable turn made to change position in z is not

counted. Significantly more cells are making no turns in the woodpiles with 15 µm pores compared to 8 µm pores.

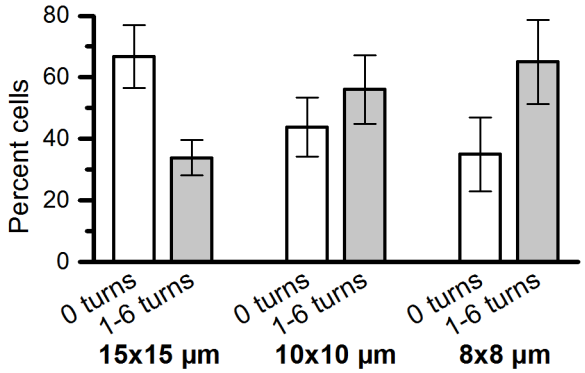

Figure 27 Comparison of the fraction of cells moving straight through a woodpile construct to cells taking one or more turns, as a function of the construct pore size. Significantly more cells turn as they migrate through 8x8 µm pore constructs than through 15x15 µm pore constructs (p=0.033). No significant difference is observed between the 10 µm and the 8 µm constructs but the trend is clear, the smaller pores induce more turns. Error bars show the standard error of the mean (n≥7).

The pore size definitely has an effect on the likelihood that a turn is made by the cell when traversing the constructs. If one looks a little more closely at the number of turns performed by the cells in the different constructs, it becomes clear that the smaller and more confined constructs increase the tendency for the cells to seek out new and possibly less constrained routes to traverse the construct. In Figure 28 the number of turns is detailed for the three different pore sizes and although no statistical significance is seen, there is a clear trend showing more turns from cells in the 10 µm and 8 µm constructs. Whether the tendency to induce more turns is also seen when comparing the 8 µm and the 10 µm pore constructs is difficult to tell. No statistical significance was found, but if the number of cells observed were increased it is possible that the trend would be clearer still. Tighter physical confinement and smaller pore sizes seem to induce more turns and could possibly be a measure of migration ability.

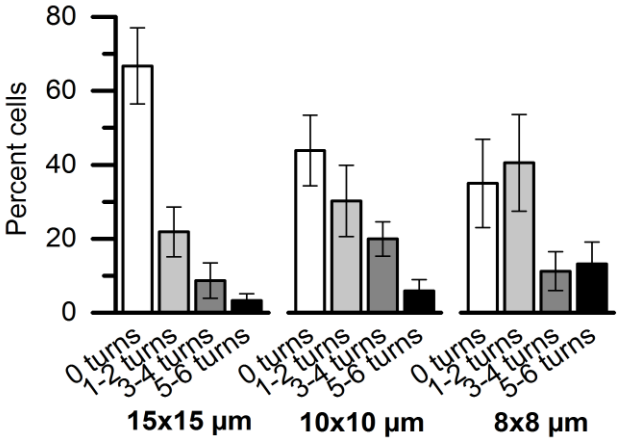

Figure 28 Detailed cell migration analysis as a function of construct pore size. There is a clear trend towards more cells making at least one turn in the smaller pore constructs. It is less clear if the 8x8 µm pores induce more cell turns than the 10x10 µm pores. Error bars show the standard error of the mean (n ≥ 7).

In the standard woodpile constructs the cells can traverse the constructs without making any turns. We therefore opted to introduce barriers in the woodpiles to force the cells to make at least two turns, see Figure 21. The length of the constructs was also changed from 100 µm to 200 µm to create a longer pathway for the cells in the construct. The introduction of barriers and the extended width of the constructs were added to better mimic the less ordered i*n vivo* extracellular environment where barriers are abundant and no straight unhindered paths are very likely. In Figure 29 the standard woodpile construct with a 10 µm pore size is compared to the construct with barriers to see the effect on the number of turns made by the cells. First it can be observed that no cells traversed the constructs with barriers without turning at least twice as deemed necessary by the two barriers they have to circumvent. Next it was found that while as many as 30 % of the cells do not turn in the standard woodpile the fraction of cells that spread over more turns increased compared to the 100 µm constructs and a number of cells were observed doing more than 6 turns, something not observed in the 100 µm long woodpiles. As expected this indicates that the longer distance traversed increase the likelihood of a cell deciding to do a turn even though it is perpendicular to the gradient slope. It could appear as if the fraction of cells going straight through the construct in the standard woodpile is added to the fractions doing 1-2 and 3-4 turns in the woodpile with barriers, signifying that the cells that would tend to go straight through if they could also opted to do a minimum of turns in the woodpile with barriers. By introducing this more complicated 3D woodpile maze it is shown that DCs can navigate through increasingly complex 3D structures. The migration ability of the DCs could be measured by letting them navigate through constructs of increasing complexity.

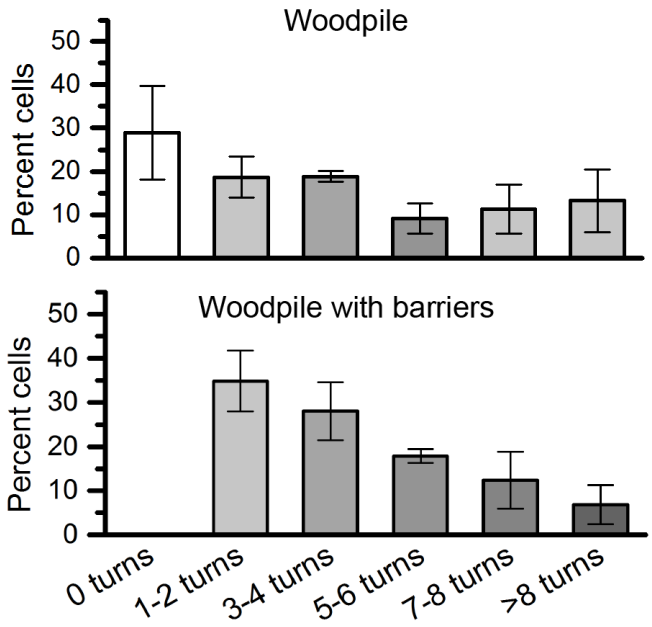

Figure 29 Fraction of DCs making specific numbers of turns inside an in-chip woodpile construct with 10x10 µm pores without (top) or with (bottom) additional barriers. The fraction of cells making a specific number of turns seems to be more spread out in the standard woodpile construct when the length is increased from 100 µm, in Figure 28, to 200 µm here (top). Note that cells by design of the construct must make at least two turns to pass the barriers. Error bars show the standard error of the mean (n=3).

2.4.2. Migration through microchannels

Migration through microchannels of varying length and cross section are performed according to the same protocol as the woodpile studies above. The channel constructs, Figure 24, are written in the middle of the bottom of the microchannel in the ibidi chip. We expect the gradient to be established inside as well as outside the microchannels. As demonstrated by others[101] the gradient observed by cells inside microchannels might be similar to what is observed in Boyden chambers where a steep concentration gradient is observed from the back to the front of the cells when the cell is reaching through the pores in the membrane with their long dendrites. If the cell is occluding the channel and thus hindering the gradient formation when migrating inside the channel a steep gradient will be formed from the front to the back of the cell. Here we analyze the influence of the channel cross section and the channel length on migration speed and also compare the in-channel migration to cells migrating outside the channels in the unstructured collagen. This gives a very good comparison between migration inside and outside the channels, because migration studies of the cells in the collagen matrix are performed simultaneously with the migration studies of the cell inside the channels. As a result it gives an unprecedented foundation to compare the two situations under near identical conditions.

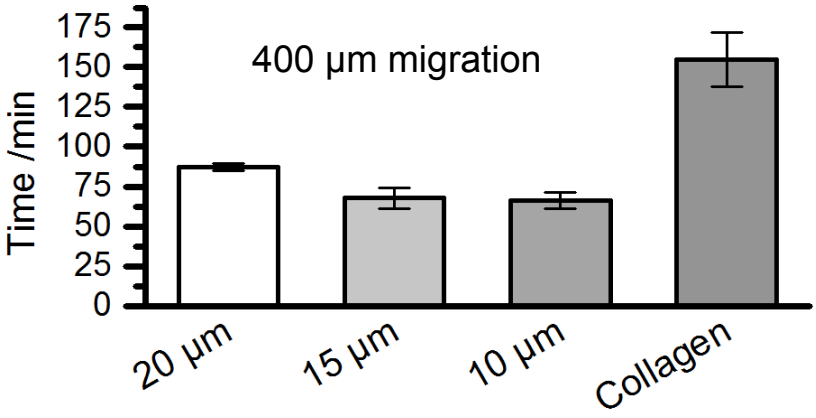

Figure 30 Comparison of migration time through 400 µm long microchannels with cross sections of 20 µm, 15 µm and 10 µm, and through 400 µm collagen. Significantly longer migration time (approx. 30 %) is observed for cells migrating through the 20 µm channels compared to both the 15 µm and the 10 µm channels ($P<0.05$). There is no observed difference in migration time between 15 µm channels and 10 µm channels. The time it take the cells to traverse 400 µm along the gradient axis is roughly doubled when done outside the microchannels in the unstructured collagen matrix compared to inside the microchannels. Error bars show the standard error of the mean (n=3).

We observe a significantly shorter migration time through the 15 µm and 10 µm channels than through the 20 µm channels, Figure 30. There is no measurable difference in migration time between the 15 µm channels and the 10 µm channels which could indicate that an occlusion is formed by the cells in the narrow channels but not, or only partly, in the wider 20 µm channels, see Figure 31.

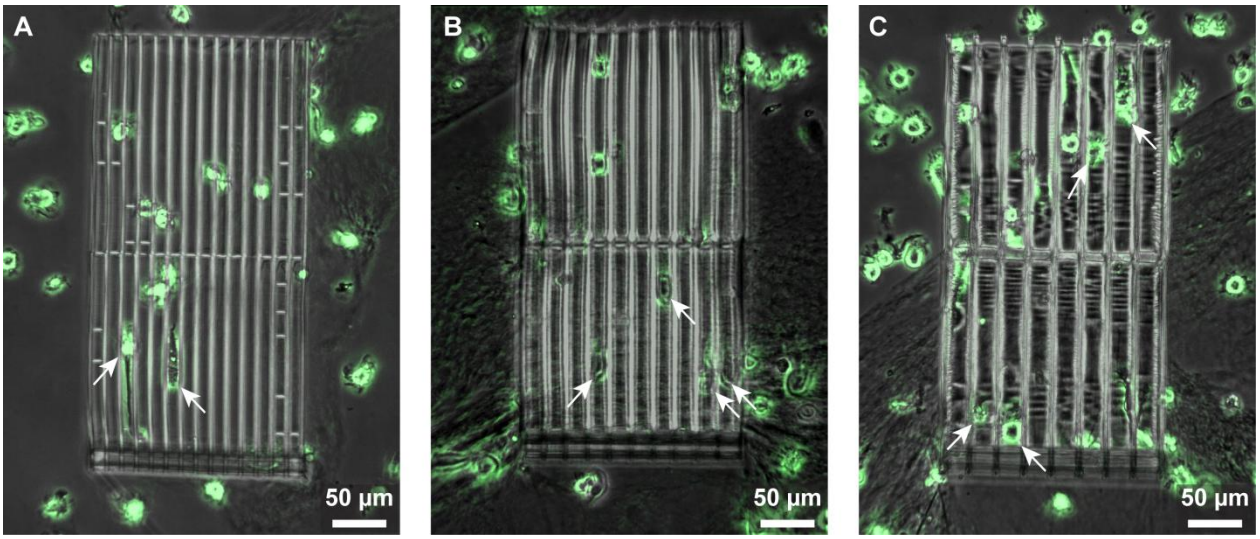

Figure 31 Phase microscopy snapshots showing dendritic cells migrating through the channel constructs with cross sections of (A) 10 µm, (B) 15 µm and (C) 20 µm. Cells inside the channels are highlighted with white arrows. In the 10 µm channel (A) it is clear that the right cell is elongated (50 µm) and occludes the channel. The cells in the 15 µm channels (B) are substantially shorter but still seem to occlude the channel. In the 20 µm (C) channels it is difficult to distinguish the cells in the channels from those on top of the construct indicating that they are less confined and probably do not occlude the channel completely. The cell outlines have been highlighted in green by use of image processing in ImageJ[90].

The migration time in the collagen matrix parallel to the gradient axis is more than double compared to inside the channels. Migration in all channel constructs outperformed the free roaming migration in the collagen matrix that showed a much longer migration time to traverse the 400 µm next to the channels. Migration speed in the collagen matrix was as low as 2.6 µm/min towards the CCL21 source, compared to 4.6 µm/min, 5.9 µm/min and 6.0 µm/min for the three channel constructs. Comparable *in vivo* and *in vitro* observations have been made and also conclude that dendritic cells migrate faster confined in microchannels than they do outside in the collagen matrix either *in vitro* or *in vivo* in the extracellular matrix[17,96,102]. The more complicated the matrix is and, consequently, the number of decisions that have to be made by the cell could be some of the main factors that explain the huge difference in migration speeds. The increased gradient slope as perceived by the cell inside the channel is most likely also a factor. To evaluate whether these effects of the perceived gradient slope were dependent on the channel length, we tested the migration time of the 400 µm channels against 200 µm channels, Figure 32.

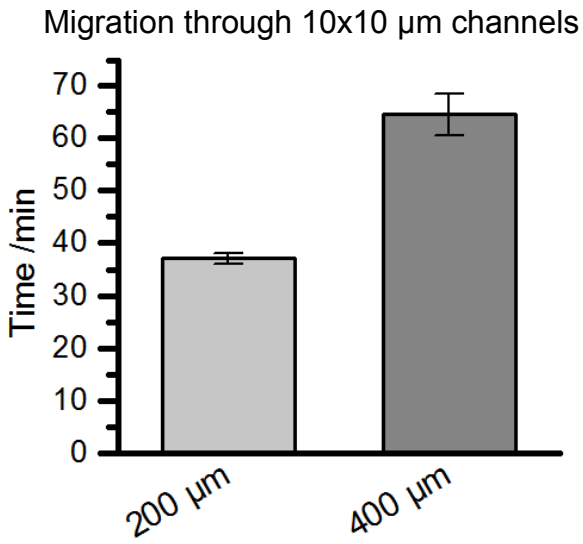

Figure 32 Migration time needed for the cells to traverse the 200 µm and 400 µm long channels with a cross section of 10x10 µm. Migration speed is slightly, but significantly (P=0.04), higher for the 400 µm channels at 6.2 µm/s vs. 5.4 µm/s for the 200 µm channels. Error bars show the standard error of the mean (n=4, 200 µm and n=5, 400 µm).

We compared the migration time in the 10 x 10 µm wide channels and found that the migration speed was slightly higher in the longer channels, namely 6.2 µm/min compared to 5.4 µm/s in the shorter channels. This difference is not much but if the occlusion theory is correct it would indicate that the longer channels favored faster migration because the occlusion is in effect in a longer channel leading to a greater concentration difference between the beginning and the end of the channel. This would again lead to an

increased gradient slope that will affect the migration relatively more in the longer channels. The decrease in migration speed observed from the 400 µm channels to the 200 µm channels is very low compared to the gap between the different cross sections in Figure 30 where the speed is reduced to 4.6 µm/min in the large, 20 µm channels. This indicates that the steepness of the increased gradient slope is an important factor in determining the migration speed.

2.5. Chip regeneration compensates for higher fabrication costs

As part of the cell handling and migration protocols used we developed a method for regeneration of the polymer in-chip migration constructs, see Appendix 1. Thanks to the easy liquid exchange and sink/source design of the ibidi chip system we were able to introduce a collagenase treatment that thoroughly dissolves the collagen gel and rinses the chip of collagen and cell residues and prepares the construct for repeated experiments. The effect of the collagenase treatment is observed in Figure 20 where there is no sign of collagen left on the constructs after multiple experiments. The hard IP-L resin creates a tough structure where the pores are still intact and the structural integrity of the construct is not compromised by the repeated treatments. The collagenase regeneration not only drastically reduces the cost of multiple experiments for this system but also for many others that utilize collagen in confined spaces. The only requirement is easy liquid exchange in the system.

2.6. Discussion

2.6.1. In chip 2PP fabrication of woodpiles and channel constructs

2-photon polymerization is still a new technology and progress is being made to improve the fabrication speed and the accuracy of the systems[83,84]. Here we opted to only use a 100x, 1.4 NA oil objective because it created a voxel of dimensions smaller than the demanded feature size. We briefly tested a 20x, 0.5 NA air objective, but chose not to go forward with the optimization due to a much larger axial length of the voxel and what seemed to be a requirement for lower writing speed to achieve full polymerization. If the voxel dimensions are calculated as previously described, the voxel will be 2.7 times wider and an astonishing 7 times longer than for the 1.4 NA objective. Thus the need for longer exposure times are explained by the loss in light intensity by the less tight focus. It was not properly investigated whether the extended voxel from the 0.5 NA objective was as well defined in height as was the case for the 1.4 NA objective. One could

imagine that if the polymerization threshold of the 0.5 NA objective was as sharp as the 1.4 NA objective then the introduction of a more powerful light source could vastly increase the volumetric writing speed, while still maintaining the overall confinement of the written lines and allowing for the creation of high resolution geometries. This means that even when low NA objectives are used the precision of the stage will still allow shallow channels or pores to be created if the voxel is well defined. To avoid many sequential lines an objective with a NA providing only the needed resolution is recommended in order to achieve the optimal writing speed. Such a strategy has been adopted by Ovsianikov et al.[54,78] to produce cylinder based scaffolds of PEGDA with a 20x, 0.4 NA objective. In retrospect an objective with an intermediate NA of ~1 would most likely have increased the writing speed of the constructs presented here without compromising the level of detail in 3D.

In this project the scope has not been to develop new technologies, but to apply current technologies in new and smarter ways. 2PP is not suitable for large volume scaffolds for grafting in regenerative medicine or building new organs from the bottom up. It definitely has the precision and resolution needed for tissue engineering, but for the time being writing speeds are too slow for many of the applications that require large volume or large numbers, thus rendering the cost of a single experiment or product too high. We have tried to utilize the benefits of the 2PP technique by polymerizing cell migration constructs of increasing complexity inside a microfluidic channel in an all polymer commercial chip. To the best of our knowledge there are only two other examples exploiting the 2PP techniques ability to polymerize constructs inside a closed microfluidic system[81,82]. Our system improves a number of issues demonstrated by other 2PP fabricated migration constructs[55,76] as well as issues already demonstrated in other in-channel fabrication schemes[82]. In-chip benefits of our migration system entail better control of- and longer lasting chemical gradients. These are paramount for reproducible and physiological relevant chemotaxis analysis, lower needed volumes of potentially expensive chemicals and easy cleaning and regeneration of the system. Our system also benefits from much faster loading and development times than previously described systems thanks to easy fluid exchange and the use of a low viscosity resin with no need for a pre-exposure baking step. We do not however address complex scaffold structures such as Schwarz p-surface or more *in vivo* like random fibrillar constructs, which might resemble the extracellular matrix more. The more complex or random structures would greatly extend the writing time and it is believed that the complexity of the connective tissue, with both loose and dense zones[103] as well as complex gradients of both chemical and mechanical nature[103] is impossible to mimic in its full extent. Therefore one must choose which tissue or characteristic of cell motility to address by the *in vitro* system. The fabrication of woodpile as well as channel constructs represents a choice of geometry that is based on what simple constructs can

approximate a given *in vivo* condition. By introducing these geometries into a premade microfluidic system it is demonstrated that 2PP fabrication of 3D cell migration constructs might be one of the best alternatives for 3D cell migration studies in terms of flexibility and ease of use.

2.6.2. Migration through woodpiles

Most noticeably we saw almost no dendritic cells traverse the 5 µm woodpile constructs. Most of the cells opted to go around the constructs thus moving perpendicular to the gradient to avoid squeezing through the narrow confinements. It has previously been shown that dendritic cells can traverse 5 µm pores in Transwell chambers[99,104] and Faure-André et al. show migration through 4 µm micro channels[102]. It is believed that the decision to go around the construct is influenced by the easier modulated collagen matrix, but if there is no other way the dendritic cells are capable of squeezing through smaller pores. The main topological difference between the Transwell system and the woodpiles is the much smaller thickness (width) of the 10 µm thick Transwell membrane that allows DC dendrites of lengths up to 70 µm, see Figure 26, to explore the highest and lowest chemokine concentrations simultaneously - effectively presenting a very steep concentration gradient. Comparably, our 100 µm wide constructs with a definable gradient slope resemble the *in vivo* microenvironment of the DCs more closely[96] and does not present the cells with a sudden increase in chemokine concentration through the next pore. This will make the decision to go around or seek other routes more plausible before deciding to squeeze through a small pore requiring cytoskeletal rearrangements and most likely nuclei deformation[18,19]. In general the DCs continue their migration path after entering the construct and do not seem to have a problem detecting the concentration gradient within the construct. We observed multiple possible pathways being probed by both the DCs in Figure 26 C. DCs show very long straight dendrites (up to 30 µm) being extended into the construct channels prior to deciding on a channel for transmigration. Up to 70 µm long dendrites are observed in the time-lapse movies (the source movie to the snapshots in Figure 26 can be seen on this direct link: http://web-files.ait.dtu.dk/maol/WoodpileMovie_15um_pores_2min_per_frame.avi). We also observed DCs going both back and forth inside the constructs before finally deciding to move in the direction of the gradient. This would indicate that the DCs can easily sense the gradient in the adjacent channels and thus also in the neighboring layers in the construct while having the opportunity to go both left and right as well as up and down. This differentiates the 3D structured migration constructs presented here from channel structures and membranes, which do not allow the cell to detect the gradient from a true 3D environment. The presence of additional barriers in the woodpile constructs prevents straight extension of probing dendrites, and may thus result in less persistent cell motion either as a result of

differences in signal processing or due to the need for repeated cytoskeletal rearrangements. We observed DCs using quite some time to decide which way to go when they encountered a barrier, this decision process can be clearly observed in the time-lapse movies (direct link: http://web-files.ait.dtu.dk/maol/WoodpileMovie_10um_pores_w.barriers_2min_per_frame.avi.). By introducing constructs of varying complexity it will most likely be possible to assess the specific migratory properties of a cell population relevant to a specific tissue or migratory pathway *in vivo*. The 2PP technique has proven suitable for the fabrication of 3D constructs that are applicable to mimic the less organized *in vivo* extracellular microenvironment. The synthetic in-chip fabricated 3D constructs presented here ideally capture the best of both analytical approaches by providing accurate structural definition and allowing for arbitrary variation in 3D connectivity, with or without the added fibrillar collagen ultrastructure. Straight channel constructs of 10x10 μm^2 to 20x20 μm^2 cross-section resulted in DC migration speeds of 4-6 µm/min, however, the effective migration speed was significantly reduced upon the introduction of branching or barriers in the channel systems due to repeated directional decision processes by the cell when encountering an obstacle to its direction of motion, be it parallel (woodpile wall at the construct entrance) or perpendicular (barrier). This is in agreement with *in vivo* migration studies showing slower migration speeds of approx. 2 µm/min of dendritic cells migrating towards lymph nodes[96].

2.6.3. Confined migration through channel constructs

By increasing the channel cross section from 15 µm to 20 µm we observed a substantially lower migration speed 5.9 µm/min vs. 4.6 µm/min. At least two phenomena will affect the migration speed when increasing the channel cross section. Firstly, by increasing the size of the channel the cells will not feel the same confinement[97] and behave more as if they were not in a channel at all. Secondly, as mentioned above, if the cells do occlude the channel a very steep gradient will quickly form between the front leading edge of the cell and the trailing end giving the cell the impression of a steeper gradient. These two phenomena could very well come into effect at the very moment when the cells no longer fill the channel cross section. At that moment the steeper gradient will no longer be formed and the cell will be less likely to change migration behavior when entering the channel because it does not feel confined enough to do so. In that case the migratory behavior of the cell will resemble more the cell migrating in the free collagen matrix. We calculated the volume of a dendritic cell to correspond to a sphere of diameter 18 µm on average, by measuring the average length of three cells in a 10 µm channel and multiplying with the channel cross-section. This size supports the assumption that the step from 15 µm to 20 µm in cross section could be around the threshold where the cells change from a confined to an unconfined migration mode. This would

also explain why the migration speed did not change between the channels with a 10 µm cross section and a 15 µm cross section. Snapshots from migration movies in Figure 31 support this theory by showing that the dendritic cells are clearly confined in the 10 µm channels, most likely confined in the 15 µm channels and less confined in the 20 µm channels. In fact it is very difficult to distinguish the cell morphology inside a 20 µm channel from those in the free collagen matrix, this is not the case for DCs migrating inside the 10 µm and 15 µm channels (direct link to movies:

http://web-files.ait.dtu.dk/maol/ChannelMovie_10um_2min_per_frame.avi
http://web-files.ait.dtu.dk/maol/ChannelMovie_15um_2min_per_frame.avi
http://web-files.ait.dtu.dk/maol/ChannelMovie_20um_2min_per_frame.avi).

We observed dendritic cell confined migration speeds of 6 µm/min in straight microchannels filled with fibrillar collagen in accordance with former work using protein coated but unfilled channels[102]. At the same time, we measured the migration speed of the cells not entering the channels but migrating alongside them in the random collagen matrix. With this setup the same batch of cells can be compared under identical conditions, and an unprecedented comparison can thus be made between confined and unconfined migration speeds. We found that free roaming cells traversed the 400 µm with an average speed parallel to the gradient of 2.4 µm/min or under half the speed of the completely confined cells in the 10 µm and 15 µm channels. The free roaming cells migrating in the collagen matrix also had the opportunity to go left and right and up and down thereby increasing the length of their overall migration path thus slowing down the traversing speed. The speed of the cells in the 20 µm channels falls in between the confined and the free migrating cells and could be called semi confined migration. Similar observations have been done before by Tong et al.[98] who also observed the division of migration speeds into steps depending on the degree of confinement. This indicate that only when the degree of confinement changes will the speed change. Thus, the speed will not necessarily changed but when the dimensions are changes only if the dimension change also changes the degree of confinement. As a result the migration speed in the 10 µm and the 15 µm channels was identical. Tong et al. observed the inverse relationship between confinement and speed compared to our experiments, but they did not use collagen filled channels and did not use dendritic cells, so the morphological change is therefore not comparable. The migration speed in the shorter 200 µm channels was slightly slower at 5.4 µm/min compared to 6.2 µm/min in the longer channels. The reason for this is believed to be the steepness of the gradient created inside the occluded channel. When the cell enters the channel the gradient step is quickly created and the chemokine concentration behind and in front of the cell equilibrates now with the concentration at the start and at the end of the channel

respectively. The concentration difference between the beginning and the end of a channel in a linear gradient will be doubled when doubling the length of the channel. The steepness of the gradient across the cell is thereby heavily influenced by the channel length and thus favors a higher migration speed in the longer channel.

3. Soft biomimetic hydrogel as cell migration platform

3.1. Poly (ethylene glycol) diacrylate as biomimetic hydrogel

A hydrogel is a "gel in which the swelling agent is water" as defined by IUPAC[105]. The connective extra-cellular matrix consists primarily of collagen, a protein based hydrogel. It is natural to look for artificial alternatives among soft hydrophilic networks that have similar properties, but are more easily tailored to a specific need. For this Poly (ethylene glycol) diacrylate (PEGDA) is a great candidate. As mentioned in the introduction, PEGDA is a widely used material in tissue engineering. The poly (ethylene glycol) PEG chains are generally known for their hydrophilicity and their protein repellent properties. Moreover it was recently shown that a PEG coating can also hinder adsorption of non-protein drugs and small molecules to various polymer surfaces[106]. The PEGDA macromers (Figure 33) normally used have a molecular weights ranging from around 500 g/mol to 20.000 g/mol. With these molecular weights the number of PEG monomer units vary from only a few to several hundreds.

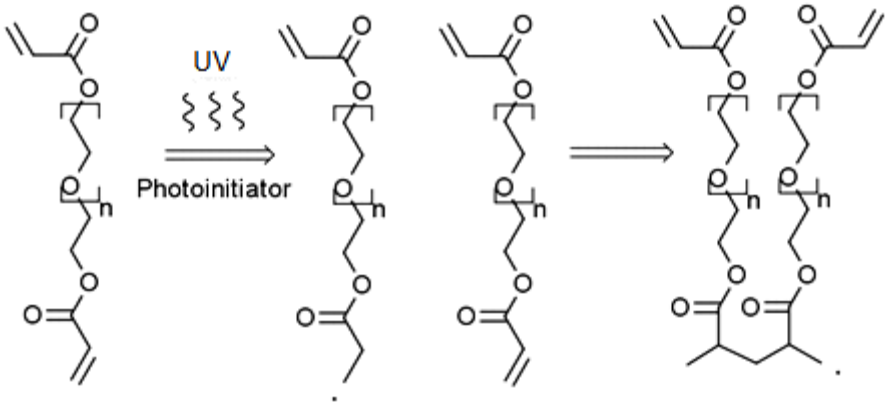

Figure 33 PEGDA macromer unit and the gel radical polymerization mechanism. The acrylate ends with the vinyl group attached to the ester is the reactive moiety. n denotes the number of PEG units in the chain. It is the ether in the chain that accounts for the hydrophilic properties of PEG. After initiation the polymerization will propagate along the kinetic chain and add more and more macromers to the network until it terminates, see Figure 34.

The very short (<700 g/mol) macromers are fluid at room temperature and are thus easier to work with and mix with various photoinitiator compounds. But the short chain networks do not hold as much water as the longer chain networks due to the shorter distance between the cross links in the gel, see Figure 34 A. Radical photoinitiation is the most widely used method to crosslink the gels.

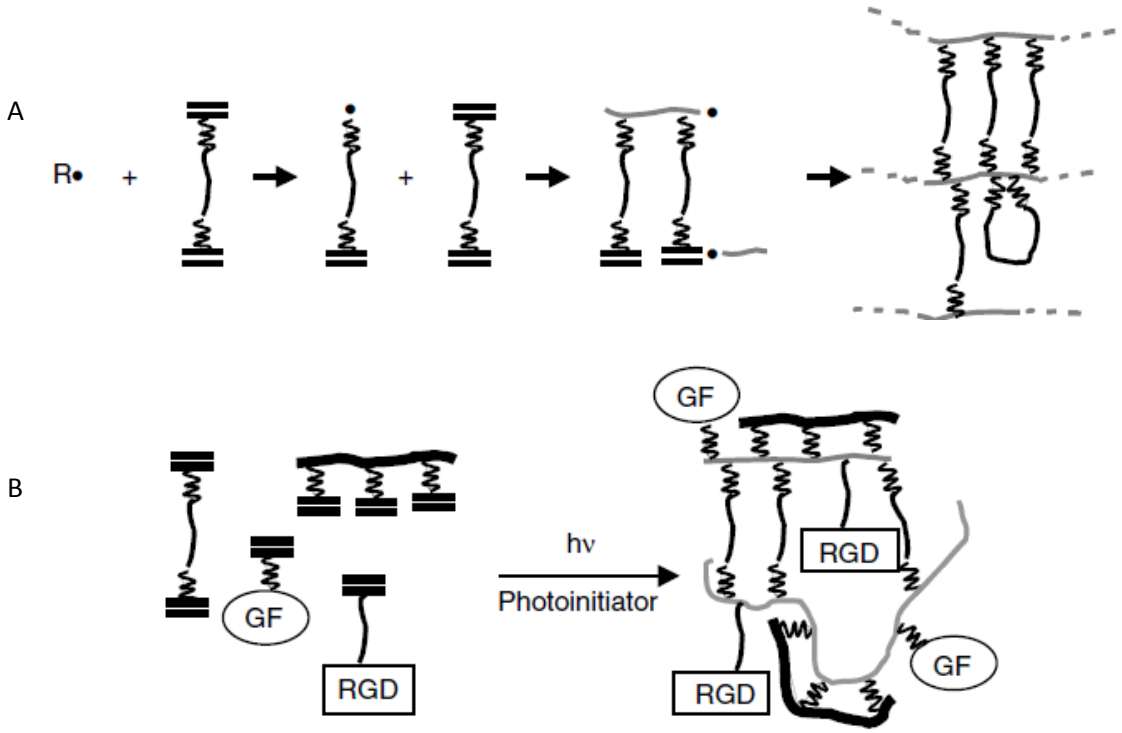

Figure 34 (A) Polymerization and cross linking of PEGDA hydrogels. The light gray chains are called the kinetic chains and are the backbone of the network. The double lines are the vinyl groups with the PEG chains in between and the dots are free radicals. Because PEGDA is a divalent macromer the acrylate in the opposite end can link two kinetic chains together with a cross link, when the cross linking density is high enough the solution reaches the gel point. (B) If functional moieties are added to monoacrylate PEG macromers they can be incorporated into the gel, RGD and GF are short for the tri-peptide Arg-Gly-Asp and a Growth Factor respectively, to create a biochemically tailored gel. The figure is adapted from Bryant el al.[107]

In a hydrogel it is the chemical potential that drives water in between the chains and the elastic retractive forces of the network that push the water out. The equilibrium is called the equilibrium degree of swelling and is defined either as the mass equilibrium degree of swelling (q) or the volumetric equilibrium degree of swelling (Q)[107]:

$$\mathbf{q} = \frac{\mathbf{M_s}}{\mathbf{M_d}}, \quad \boldsymbol{Q} = \frac{\mathbf{V_s}}{\mathbf{V_d}} = \mathbf{1} + \frac{\boldsymbol{\rho_p}}{\boldsymbol{\rho_s}}(\mathbf{q} - \mathbf{1})$$

with M_s and M_d being the mass of the swollen and the dry gel, V_s and V_d being the volume of the swollen and dry gel, and ρ_p and ρ_s being the density of the polymer and the solvent respectively. The equilibrium degree of swelling is interesting, since it relates to the mechanical properties of the gels and hence is very important when designing biomimetic gels for a specific tissue or cell response[35,108–110]. q is especially easy to measure by weighing the polymerized dry and swollen samples. PEGDA hydrogels have been shown to

span a range of elastic moduli ranging from that of soft tissue ~1 kPa[111] to that of soft cartilage ~ 1 MPa[108]. These numbers also correlate well with the mechanical properties of collagen gels used in migration studies as an extracellular matrix component that has been shown to have elastic moduli between 1 kPa and 25 kPa depending on concentration[112]. PEGDA is therefore a very good alternative for building soft 3D shaped migration scaffolds.

Several factors will influence the equilibrium degree of swelling and the mechanical properties of the PEGDA gel:

1. If the macromer length increases the gel will tend to swell more and become softer, on the other hand shorter macromers will give harder and more brittle gels.
2. The polymer volume fraction ($V_{2,r}$) in the relaxed preparation state will change the cross linking density and thus the swelling and the mechanical properties. Higher $V_{2,r}$ will lead to stiffer gels.
3. Total fluence (J/cm^2) and concentration of photo initiator will also have an effect on the mechanical properties of the gel. If limited by kinetics a short exposure or low photo initiator concentration will give a softer gel, due to incomplete crosslinking.
Depending on the photo initiator and macromer concentration a saturation point will be reached where extended exposure time will have no effect because all the crosslinkable moieties have reacted.

PEGDA hydrogels are also used in tissue engineering because they function as a “blank slate” for designing specific scaffolds for regenerative medicine[22]. The term blank slate means that the scaffold is free of any biochemical clue or signal that natural derived hydrogels, such as collagen or matrigel, have build in by nature. The idea is then to add only the biochemical stimuli needed for the study. The remaining unreacted acrylates in the hydrogel matrix will still be reactive and can be used to add biochemical functionalities either in 2D patterns on the surface[24] or in 3D patterns in the bulk[113,114], see also Figure 34 B. Macromers with the tri-peptide (Arg-Gly-Asp/RGD) have successfully been added to the preparation solution and incorporated to facilitate integrin mediated cell adhesion[115]. A typical way of linking a functional moiety to the PEG chains is to use a *N*-Hydroxysuccinimide (NHS) coupling reaction that couples any primary amine with a NHS functionalized molecule, see Figure 35, but also click chemistry[116,117] has proven very useful for functional patterning of PEG hydrogels . By coupling to a primary amine proteins and any peptide that include lysine can easily be coupled to an Acrylate-PEG-NHS macromer and then be linked to the gel either in bulk or in patterns with photo lithography.
With these methods it is possible to tailor both the PEGDA hydrogels mechanical and biochemical properties to a given purpose.

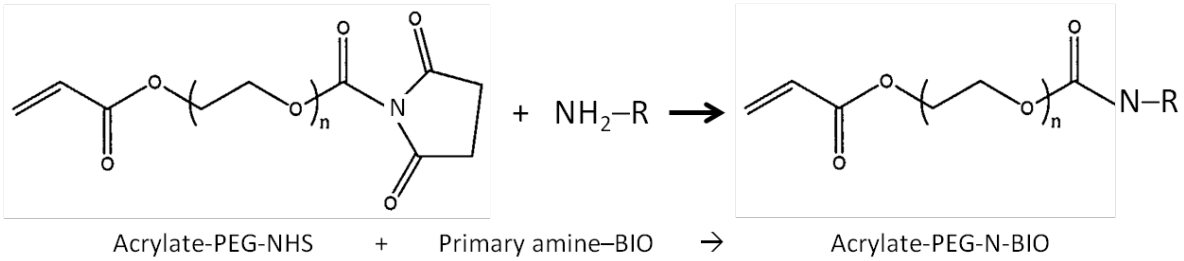

Figure 35 NHS coupling reaction often used to incorporate bio molecules into PEGDA hydrogels. The NHS moiety reacts under slightly basic conditions with primary amines. The primary amine in lysine is a very good candidate and most proteins and peptides with lysine will therefore easily couple with a NHS functionalized molecule.

3.2. Photo initiation with Irgacure 2959 and Irgacure 369

In this work two commercial UV photoinitiators have been used for cross linking the PEGDA hydrogel: Irgacure 369 (I369), and Irgacure 2959 (I2959). The photoinitiated radical formation of the two initiators can be seen in Figure 36.

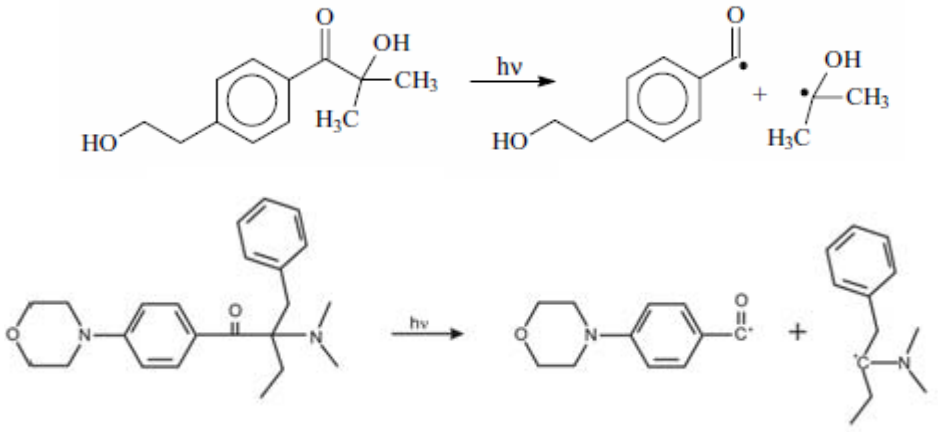

Figure 36 Schemes showing the photoinitiator Irgacure 2959 (TOP) and Irgacure 369 (BOTTOM) undergoing cleavage and radical formation after photon absorption, adopted from Masson et al.[118] and Ovsianikov et al.[59] respectively.

After absorption the molecule cleaves into two, creating two radicals that will initiate the polymerization of the acrylate end groups and crosslink the resin into a hydrogel. Irgacure 369 was the photoinitiator preferred for 2PP of the 3D PEGDA structures because of the superior 2PA[119] cross section and the better overlap of the excitation spectrum with the 780 nm laser in our 2PP setup. Irgacure 2959 was initially used

for polymerization of PEGDA slaps for evaluating biochemical functionalization with stained proteins and RGDS peptides as well as for evaluating the cytotoxicity of the Irgacure 369. Irgacure 2959 is known to be one of the least cytotoxic radical photoinitiators[91] and is widely used for cell encapsulations in tissue engineering[35,120]. It therefore served as a benchmark for the biocompatibility test of the Irgacure 369 that previously had shown signs of higher cytotoxicity[72].

Cytotoxicity of polymerized hydrogels was evaluated using the same metabolism assay (AlamarBlue) as presented in Section 2.2.2 with both DCs and NIH-3T3 cells to ensure no adverse effects originated from the resin with Irgacure 369. Cytotoxic comparison was made against Tissue Culture grade polystyrene (TCPS) as a non-toxic reference and against PEGDA photopolymerized with Irgacure 2959, a system that is often used in biomedical applications and in tissue engineering in general and proven one of the least cytotoxic[78,91]. The initiator concentration was increased to 3 % wt to simulate the concentration needed for 2PP fabrication of hydrogel constructs. 350 Da PEG was used as solvent for the hydrogel with Irgacure 369 as initiator, because Irgacure 369 is not water soluble.

Methods

Experiments were performed in a 96 well TCPS microtiter plate (Nunclon grade, Nunc, Roskilde, Denmark). 50 µl 20 % wt 1000 Da PEGDA (Sigma Aldrich) in MilliQ (Merck Millipore, Billerica, MA) water with 3 % wt Irgacure 2959 or in 350 Da PEG (Sigma Aldrich) with 3 wt % Irgacure 369 was dispensed into a well and photopolymerized with a dose of 8.6 J/cm^2 at 365 mW in a MA4 mask aligner (Suss Microtec). High exposure doses were required due to the presence of ambient oxygen acting as a radical quencher. A third untreated well was used as the non-toxic TCPS reference. Samples were prepared in triplicate on each plate. All wells were washed three times with MilliQ grade water and left with MilliQ water for a further 72 hours at room temperature. Culture medium consisted of IMDM for the DCs or DMEM for the 3T3 cells, both with 1% penicillin / streptomycin (P/S) and 10 % Fetal Bovine Serum (FBS) from Invitrogen (Life Technologies, Paisley, UK). The wells were filled with culture medium for 15 minutes and emptied, prior to seeding 5000 – 10000 cells in 100 µl culture medium in each well and incubation for 24 hours. The number of cells used in each experiment was constant but varied with the number of cells (DC) in the provided vials from Herlev Hospital between experiments, since the assay measures the relative metabolism an individual cell count was not performed. 10 µl AlamarBlue (Life Technologies) was added to each well and incubation was continued for 2 hours. After incubation 100 µl supernatant was transferred to a new microtiter plate, and the developed color was measured in a Victor3 plate reader (Perkin Elmer, Waltham, MA).

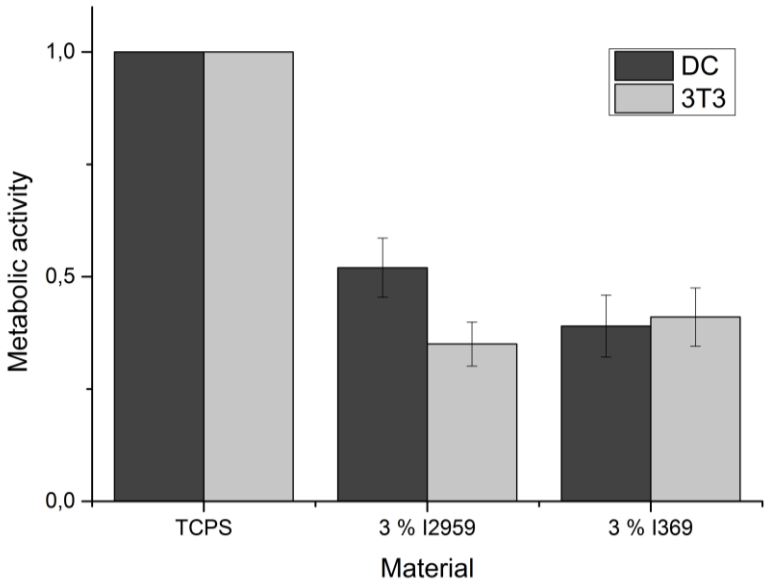

Figure 37 Metabolic activity of dendritic cells and 3T3 cells cultured on different materials. Lower metabolic activity is observed here than when performed previously (Figure 15) due to the increased photo initiator concentration. At 3 % wt concentration almost no difference between PEGDA hydrogels with the two initiators I2959 and I369 is observed. Tests are performed with an AlamarBlue assay and the graph shows the activity relative to the metabolic activity on TCPS. Values are the average of three independent experiments. Error bars show the standard error of the mean.

The TCPS well bottom was chosen as reference material for the cell metabolic activity on the PEGDA hydrogels with the two different initiators. Figure 37 shows that photopolymerized hydrogels induce some reduction in cell metabolism compared to TCPS, but no significant difference between the two initiators is found. These results were obtained on 1.5 mm thick material layers coating the entire well bottom. Considering the extremely small volumes of photopolymerized material in 2PP constructs as well as an efficient washing process if incorporated into the ibidi chip we do not anticipate significant cytotoxic effects. I369 is poorly soluble in water so the washing steps using MilliQ water presented above are not optimal. In the ibidi chip washing steps with isopropanol and ethanol can be introduced to increase the washing efficiency.

3.3. Chemical and physical tuning of PEGDA properties

Before starting to construct 3D scaffolds we tested the techniques used to alter the mechanical and chemical properties of the PEGDA gels. Control of surface adhesion sites and general biochemical patterning was investigated. Control of swelling and thus mechanical stiffness was examined as well as the post polymerization water uptake degree to decrease swelling post polymerization and aid 3D construction.

3.3.1. Swelling studies of PEGDA hydrogels and control of the mechanical properties

Swelling of a hydrogel is governed by the balance between the retractive forces in the network and the chemical potential driving the water into the network. From the change in chemical potential when mixing a polymer with a solvent one can express the polymer–solvent interaction parameter χ. For PEG in water χ is 0.426[121]. χ is small for PEG in water due to the very hydrophilic ether groups in the PEG chains. By changing the average molecular weight of the macromers we here show how q can be controlled.

Methods

Poly (ethylene glycol) diacrylate (PEGDA) with average molecular weights of either 1 kDa from Sigma Aldrich or 5 kDa from Creative PEGWorks, Winston Salem, NC, was mixed with MilliQ grade water in a 1 ml Eppendorf tube (Eppendorf AG, 22339 Hamburg, Germany) to make a solution with 2 parts PEGDA and 7 parts water. Subsequently 1 part 1 % Irgacure 2959 in acetone (both Sigma Aldrich) was added to yield a 20 wt % PEGDA, 0.1 wt % Irgacure 2959 formulation. A mixed (1kDA/5kDA) formulation with 10 wt % 1 kDa PEGDA and 10 wt % 5 kDa PEGDA was also prepared. The formulations were then briefly mixed on a vortex shaker and ultrasonicated for 10 minutes to avoid bubbles. The PEGDA formulations were polymerized by adding 65 µl formulation to a 65 µl Gene Frame (Thermo Scientific, Waltham, Massachusetts) situated in a 60 mm petri dish and sealed with the plastic lid. The formulations were then exposed to a dose of 8.6 J/cm^2 at 365 nm in a MA4 mask aligner (Suss Microtec). After exposure the Gene Frame was removed and 6 ml MilliQ water was poured over the polymerized hydrogel slap for hydration in the petri dish over night at room temperature. The following day the excessive water was carefully dried off the hydrogel slap with a tissue and the slap was weighed on a scale. The slap was then left to dry in an desiccator for 48 hours and weighed again. From the swollen and the dry weight the equilibrium degree of swelling, q was determined.

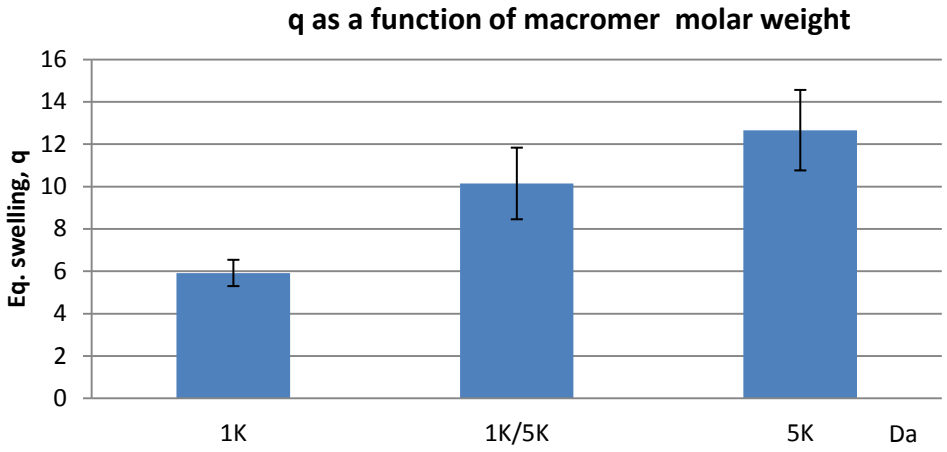

Figure 38 Equilibrium degree of swelling as a function of PEGDA macromer molar weight (1 kDa; 50/50 1kDa/5 kDa; 5 kDa). Error bars are 5 % confidence intervals, n=5.

The PEGDA mass equilibrium degree of swelling, q, is clearly tunable by changing the macromer weight. We observed a change from 5.9 to 12.6 when the macromer molar weight increased from 1 kDa to 5 kDa, and when the two formulations are mixed a q value of 10.1 (in between the two pure macromers) is found. From these numbers one can calculate the elastic modulus from the average molecular weight between cross links, M_c,[122] with the equation derived by Peppas and Merrill:

$$\frac{1}{\overline{M}_c} = \frac{2}{\overline{M}_n} - \frac{\left(\frac{\bar{v}}{V_1}\right)\left[\ln(1-\upsilon_{2,s}) + \upsilon_{2,s} + \chi_1 \upsilon_{2,s}^2\right]}{\upsilon_{2,r}\left[\left(\frac{\upsilon_{2,s}}{\upsilon_{2,r}}\right)^{1/3} - \left(\frac{\upsilon_{2,s}}{2\upsilon_{2,r}}\right)\right]}$$

Here M_n is the number average molecular weight of the macromers, $\bar{v}$ the specific volume of the polymer, V_1 the molar volume of the solvent, and $v_{2,s}$ and $v_{2,r}$ the polymer volume fraction in the relaxed and the swollen state, respectively ($v_{2,s}$=1/Q). From that one can calculate the shear modulus of a perfect hydrogel network[123]:

$$G = \frac{\rho R T}{\overline{M}_c}\frac{\overline{r_o^2}}{\overline{r_f^2}}\left(1 - \frac{2\overline{M}_c}{\overline{M}_n}\right)$$

where ρ is the polymer density, R the gas constant, T the absolute temperature and $\frac{\bar{r}_o^2}{\bar{r}_f^2}$ the front factor or the ratio between the end to end distance of a real network versus the end to end distance of an isolated

chain, which is often approximated to 1. From $E = 2G(1 - \nu)$ and the above equations it is clear that a reduced expression for the elastic modulus, E, can be derived:

$$E = -2\rho RT(1 - \nu)C \qquad with\ C = \frac{\left(\frac{\bar{v}}{V_1}\right)\left[\ln(1 - \upsilon_{2,s}) + \upsilon_{2,s} + \chi_1\upsilon_{2,s}^2\right]}{\upsilon_{2,r}\left[\left(\frac{\upsilon_{2,s}}{\upsilon_{2,r}}\right)^{1/3} - \left(\frac{\upsilon_{2,s}}{2\upsilon_{2,r}}\right)\right]}$$

M_n, the molecular weight of the macromer is not a variable in the latter formula, thus the elastic properties of rubbery gels are independent of the macromer molecular weight and can be estimated from the observed equilibrium degree of swelling alone. Experimental findings in the literature also suggest that the modulus only depends on q and is independent of M_n[108].

By inserting the values for q from Figure 38 in the equations above we find the theoretical elastic moduli to be:

Macromer M_n and q	1 kDa PEGDA, q= 5.9	1 kDa/5 kDa PEGDA, q=10.1	5 kDa PEGDA, q=12.7
Calculated elastic modulus	71 kPa	19 kPa	11 kPa

These numbers indicate that we are in the range of the mechanical properties of soft tissue. The observed values for the elastic moduli of tissue differ often by an order of magnitude, and sometimes by two orders of magnitude dependent on the method used to determine them[111]. With the mechanical observations done from the studies of PEGDA hydrogels in literature it is clear that the calculated values presented here are lower than what is reported elsewhere for comparable degree of swelling[35,110,124,125].

If considering the amount of force individual cells have been observed to exert on their substrate upon migration or contraction to be between 50 nN and 400 nN for cardio myocytes and fibroblasts[33,56] it is relevant to calculate what deflections such forces would imply to the presented 10x4 µm beams of 10 µm length. If the beams are considered to have an elastic modulus of 10 kPa and either being free hanging or fixed at the ends, the deflection from a cell exerting 100 nN of force on the center of the beam is either 0.6 µm or 0.15 µm respectively[126]. DCs have been observed to exert much less force on PDMS micro pillars[127] so it is fair to assume that the stiffness of beams are sufficient not to be distorted by the DCs.

These considerations on the mechanical properties are purely based on thermodynamics and are only meant as a guideline. The amount of imperfections in a real world gel network and approximations done suggest that rheological measurements have to be done on the individual systems to establish the actual mechanical properties. We have shown that by altering the molecular weight of the macromers we can

control q and thus control the mechanical properties within the range of the values observed for soft tissue.

3.3.2. Biochemical modification of PEGDA hydrogels

To address our ability to control biochemical cues on the surface of the PEGDA hydrogels, we used photo lithography to test how we could attach the fluorescein labelled protein streptavidin to an Acrylate-PEG-NHS macromer and subsequently attach it to the surface of an already crosslinked hydrogel. By printing 300 µm stripes with a standard inkjet printer on a transparency sheet a quick shadow mask was created for the purpose.

Methods

First the NHS coupling reaction was performed by mixing 100 µl of 1mg/ml Streptavidin-Alexa488 (Sigma Aldrich) in PBS with 100 µl 20 wt % Acr-PEG-NHS, M_n 3400 g/mol from Creative PEGWorks in PBS and leaving it over night at room temperature. A molar ratio of PEG:Streptavidin of 300:1, was chosen to ensure that as many streptavidin molecules as possible were modified with at least one Acr-PEG-NHS. The following day 22 µl 2.5 wt % Irgacure 2959 in acetone was added to achieve 0.25 wt % photoinitiator in the formulation.

A gel slap was prepared from 5 kDa PEGDA as described above, but instead of immersing the polymerized slap in water it was briefly flushed with MilliQ water and 20 µl of the streptavidin-NHS-PEG-Acr solution was added on top of the slap, and covered by the printed mask which was laid directly on top. It was important to turn the printed side upwards as most printer ink is somewhat water soluble. The slap was then exposed to a dose of 1 J/cm^2 in the mask aligner. After exposure the transparency mask was removed and the hydrogel slap was flushed three times with MiliQ water.

The coupling reaction was verified with a MALDI-TOF mass spectrometer (Bruker, Billerica, Massachusetts), and the subsequent photo lithography was verified with an Axio Observer fluorescence microscope (Carl Zeiss, Oberkochen, Germany).

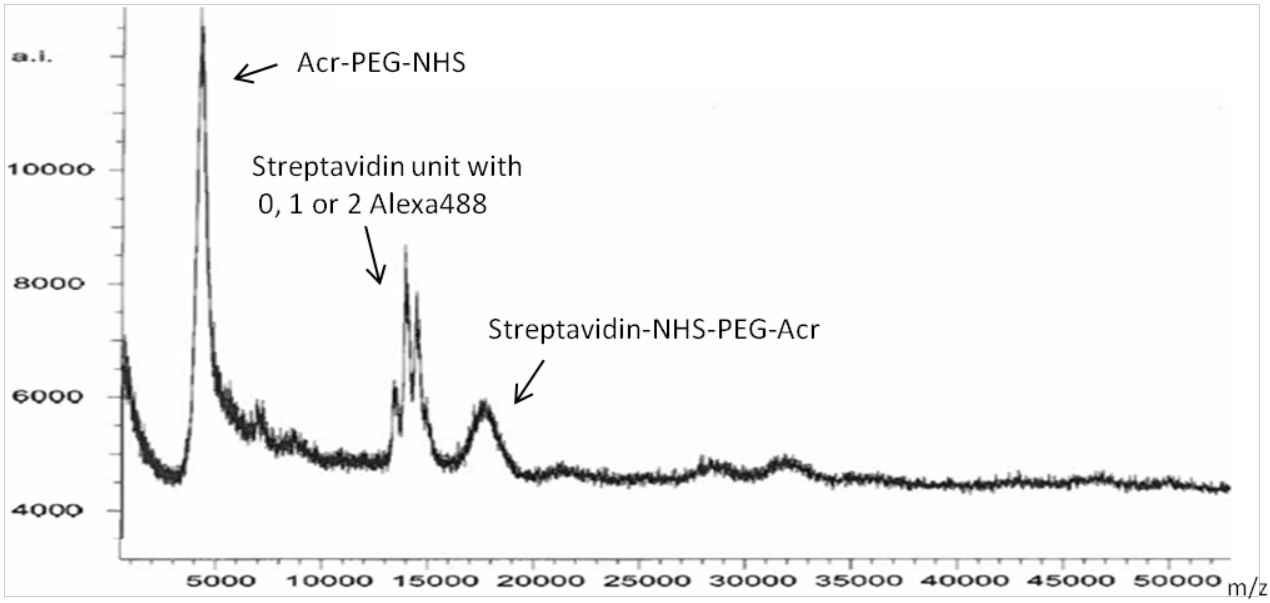

Figure 39 Scan of mass spectrum obtained after the coupling of a 3400 g/mol Acr-PEG-NHS with 53000 g/mol StreptavidinAlexa488. The 3400 g/mol Acr-PEG-NHS shows up at 5000 but is really only 3700, it is not displayed correctly here because the linear detector used does not handle small molecules very well. At 13500 the streptavidin-Alexa488 conjugate shows up with 0, 1 or 2 Alexa488 conjugated to the streptavidin. The conjugated Acr-PEG-NHS-Streptavidin product can be seen at around 17500. These data show around 50 % of the streptavidin molecules are coupled to a PEG macromer. The more smeared out signal of the product comes from the polydispersity of the PEG molecular weights, see Figure 41.

It can be seen in Figure 39 above that the MALDI-TOF data suggests that 50 % of the Streptavidin did couple to a NHS-PEG-Acr macromer. It is not the a very high yield, but as the unbound streptavidin will not passively adsorb to the gel due to the protein repellent properties of PEG this is not believed to be a problem.

To test if the remaining acrylates in the gel were stable over longer time, the hydrogel slap samples was stored in 6 ml PBS at 5 degree Celsius for 72 hours and the photo patterning process was repeated. After 72 hours all the hydrogel slaps were dried with a napkin and 20 µl of the photo active Acr-PEG-Streptavidin formulation was added and photo lithography was performed as before, but this time with the mask turned 90 degrees. The resulting patterns of both the first exposure and the second exposure after 72 hours can be seen in Figure 40. It is clear from the uneven edges of the resulting patterns that the DPI of the standard inkjet printer was a limiting factor in achieving the best resolution. The edges of the patterns are relatively sharp meaning the lithography is not the limiting factor here, but the resolution of the shadow mask is. Since 300 DPI equals to a "dot" size of 1 inch/300 = 85 µm this is to be expected. Even after 72 hours it seems that there are still free unreacted acrylates left in the network, as a clear pattern emerges perpendicular to the line created 72 hours earlier, Figure 40 B.

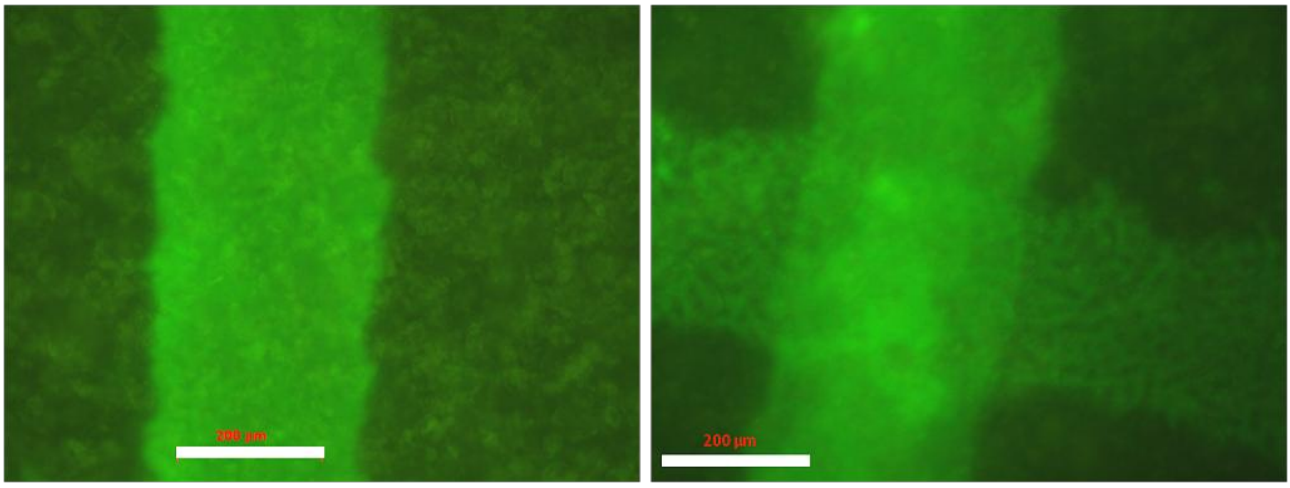

Figure 40 Fluorescence micrographs showing conjugation of Streptavidin-PEG-Acr to already polymerized PEGDA slaps. Lines created with an inkjet printed transparency shadow mask on a PEGDA slap, just after polymerization (Left) and subsequent patterning (horizontal line) after 72 hours of storage in PBS (Right).

To increase cell adhesion to the non-adhesive PEGDA hydrogels we decided to follow the same procedure as above with the protein SteptavidinAlex488 conjugation to a NHS-PEG-Acr macromer, but now with the small peptide KGGGGGGRGDS (889 Da). The lysine end is meant for coupling to the NHS moiety on the macromer while the RGD end will mediate integrin adhesion.

Methods

Coupling of the peptide to the Acr-PEG-NHS macromer was performed, as described earlier, by adding 100 µl 6.67 mg/ml peptide in PBS to the 100 µl 20 mg/ml Acr-PEG-NHS solution. This yields a 1:1 molar ratio of the peptide:macromer. Photo coupling with transparency shadow mask was also achieved as before. After patterning with the RGD peptide the slaps were moved to the cell lab and placed in a 6 well plate, where 10^5 NIH-3T3 fibroblast cells were seeded in DMEM medium with 10 % FBS and 1 % penicillin/streptomycin, all from Invitrogen, Life Technologies, Paisley, UK. They were then left to adhere overnight in an incubator, 37 °C, 5 % CO_2.

Coupling of the RGD peptide to the Acr-PEG-NHS macromer was verified by MALDI-TOF, see Figure 41. More than 50 % of the macromer is conjugated to the peptide shown by the shift in mass equivalent to the mass of the peptide of 889 Da, from approximately 3700 Da to 4600 Da. The number average molecular weight of the Acr-PEG-NHS was supposed to be 3400 Da, which does not fit very well with our findings, but for this purpose it is not relevant whether the average weight of the macromer is 3400 Da or 3700 Da.

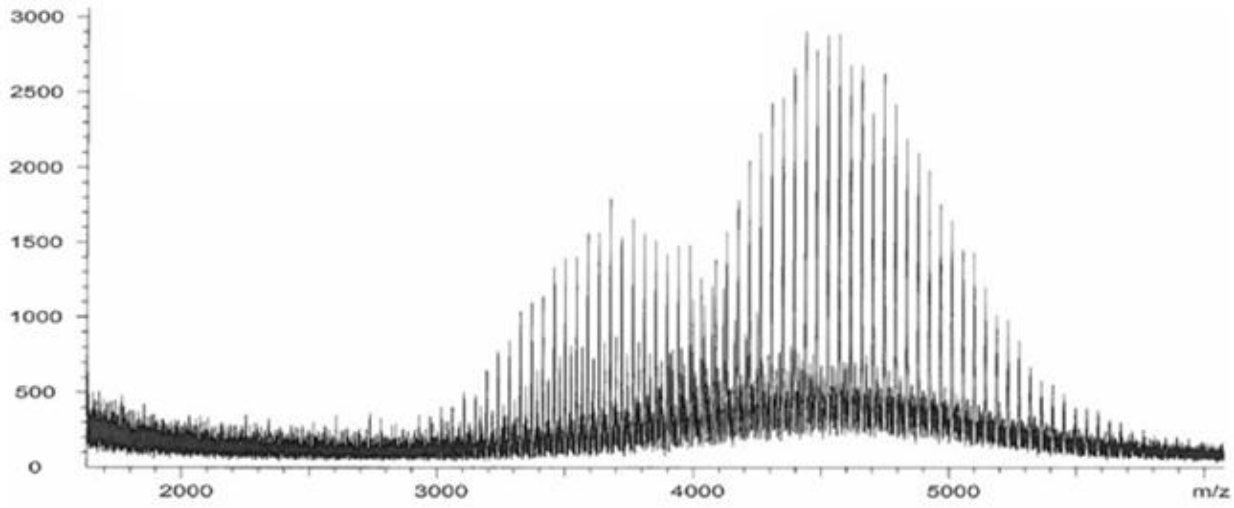

Figure 41 Scan of mass spectrum obtained after the coupling of a 3700 mw Acr-PEG-NHS with 889 mw RGD peptide. A clear shift of approximately 889 da is observed for more than 50 % of the PEG macromers confirming the successful creation of the RGD-PEG-Acr product.

Validation of the photo patterning of RGD peptide adhesion sites to the surface of the PEGDA slaps was done by microscopy investigation of the incubated slaps with 3T3 cells. Due to problems with the acquisition of the images only one image of adhering 3T3 cells was produced. It is evident from Figure 42 that a line of approximately 200 µm in width is created with confluent cells and the fact that no adherent cells are observed outside of this area confirms that no cells adhere to an untreated PEGDA hydrogel. Cell clusters are formed because the issues with acquisition meant the cells were a prolonged time at ambient temperature causing them to let go of the substrate and cluster. Right after the samples were removed from the incubator fine lines of cells adhering only to the photo patterned areas were observed, but unfortunately only the one image in Figure 42 was produced to document the experiment. Various problems with the coupling reaction and down time of the characterization equipment meant that the results were never reproduced. The results show that the hydrogels presented here can be modified to promote cell adhesion, but more evidence of reproducibility by this procedure is needed if further investigations are to be made.

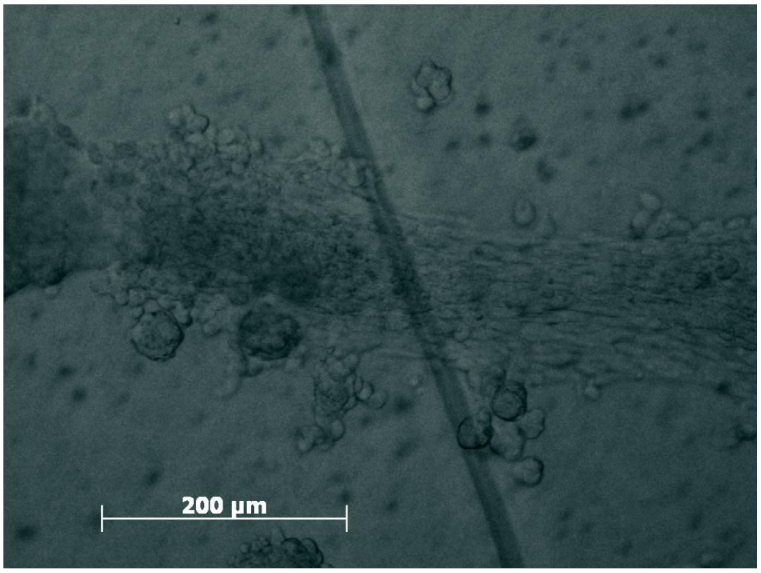

Figure 42 Bright field micrograph of a line with adherent 3T3 cells on a RGD photo patterned PEGDA hydrogel slap.

3.4. 3D structuring of hydrogels

In this section an attempt to find the best PEGDA formulation for 3D hydrogel fabrication will be discussed, including finding the optimal photoinitiator and optimizing the post polymerization swelling for minimal structural distortion. Finally, the early in-chip 2PP fabrication of 3D hydrogel constructs will be shown.

3.4.1. Optimizing the PEGDA formulation for 2PP

To achieve an optimal 2PP formulation two things are important: processability and structural rigidity. Processability means how effective the photo initiator is and what writing parameters are applicable. Structural rigidity includes whether the construct geometries are distorted due to swelling and whether the constructs are stable enough to handle the liquid exchange and washing procedures. An optimal photo initiator will need to be water soluble, because the polymer volume fraction in the preparation state has to be as close as possible to the polymer volume fraction in the swollen state to avoid post polymerization swelling and resulting distortion of any 3D geometry. The I369 is not water soluble but it is one of the most frequently used commercially available photointiators for 2PP[33,45]. It has even been used to produce 2PP scaffolds for tissue engineering from PEGDA[40,72], but only without water present in the preparation state. As most very effective 2PP initiators consist of large conjugated π-systems that feature a donor-acceptor-donor or acceptor-donor-acceptor geometry[63,128,129], they are very seldom water soluble. One group has

presented the use of a specially designed water soluble 2PP photoinitiator[130] to construct 3D hydrogel scaffolds with PEGDA and another group has presented a strategy to use hydrophobic initiators by solvating them in the surfactant Pluronic F127[131]. However, since we did not have access to an effective water soluble 2PP photoinitiator we exchanged water with a short liquid PEG 350 g/mol as the solvent and used 3 % wt I369 as the photoinitiator. Huang et al.[132] demonstrate that the polymer solvent interaction parameter χ of the solvent in the preparation state shows only a very weak influence on the resulting degree of swelling. This result suggest that we can exchange water as the solvent with PEG without increasing the post polymerization swelling.

The 3D constructs should be minimally distorted after development and introduction of water to the system. The post polymerization water uptake degree (w_u) defined as

$$\boldsymbol{w_u = \frac{v_{2,s}}{v_{2,r}}}$$

was determined to see which polymer volume fraction in the preparation state ($v_{2,r}$) would come closest to the polymer volume fraction of the swollen state ($v_{2,s}$). From Gnanou et al.[109] and the swelling data presented in Figure 38, PEGDA slaps with relevant polymer volume fractions in the preparation state were determined and tested as previously described. The polymer volume fraction was varied from 0.08 to 0.2 and the resulting water uptake degree can be seen in Figure 43**Error! Reference source not found.**. A minimum additional water uptake of 30 % vol was observed at a polymer volume fraction of 0.16. Hence it was decided to use 16 % wt 1k PEGDA in the hydrogel formulation for 3D structuring with 2PP instead of the 20 % wt used previously. By decreasing the polymer volume fraction during polymerization the water uptake was reduced from 60 % vol to 30 % vol welling will still occur, but with this optimized formulation a minimum of post process swelling is expected.

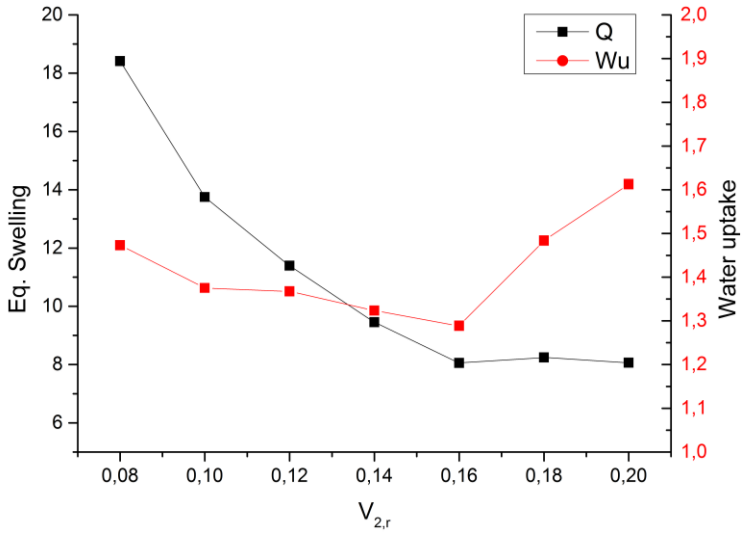

Figure 43 Equilibrium degree of swelling and water uptake degree as a function of polymer volume fraction in the preparation state. The water uptake degree has its minimum at a polymer volume fraction of 0.16. Values are average of triplicates.

3.4.2. In-chip 2PP structuring of 3D hydrogel constructs

As presented in the previous section 2PP of hydrogel constructs was performed on the Nanoscribe Photonic Professional. PEGDA hydrogels do not adhere very well to surfaces such as the polyethylene based ibidi chip we used for in-chip 2PP of cell migration constructs. As already discussed we have recently developed a procedure for attaching PEG to polymer surfaces in our lab. Above we presented an adjusted procedure to conjugate PEGDA macromers to the surface of the IP-L constructs and the ibidi chip interior, here we utilize that same procedure to increase adhesion of 2PP PEGDA constructs to the ibidi chip surface (see section 2.2.3 for methods). It was believed that adhesion of 2PP fabricated PEGDA constructs would be increased due to the attached PEGDA macromers still presenting free acrylate groups that would conjugate the polymerized hydrogel to the chip surface. We tested this hypothesis by cutting out small sections of the chip bottom (5 x 5 mm) with a CO_2 laser (FH Flyer, Synrad, Mukilteo, WA) and analysing the atomic composition by X-ray photoelectron spectroscopy (XPS). The analysis was performed on a K-Alpha spectrometer (Thermo Fisher Scientific, UK) using a 400 µm wide monochromatized AlKα X-ray spot with collection of the emitted photoelectrons at a pass energy of 200 eV. The data was fitted using the instruments Avantage software package. We analyzed the inside surface composition of the ibidi chip both before and after PEGDA coating.

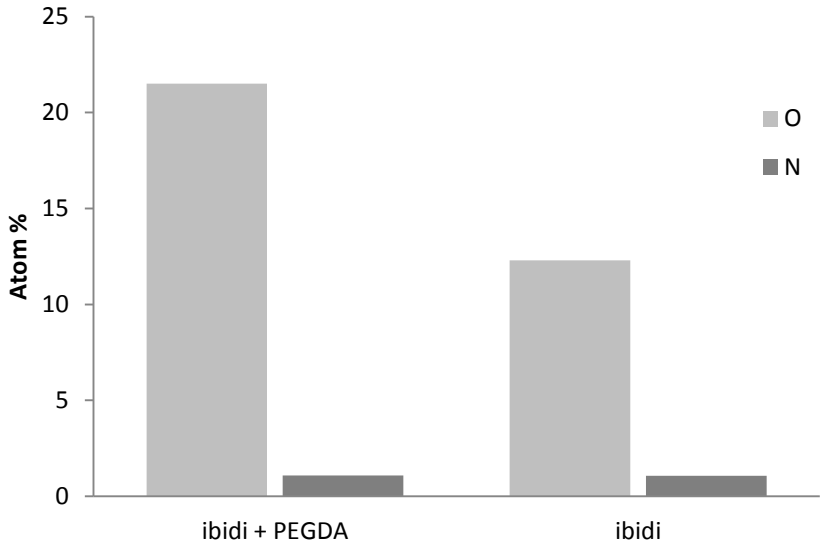

Figure 44 XPS survey showing the atomic composition of the inside of the ibidi chip with or without PEGDA surface coating. The oxygen content is clearly increased after surface coating with PEGDA indicating a successful coating procedure. The values are average values of two measurements.

The coating process increased the oxygen content on the inside of the ibidi chip from 12 % to 21 % (Figure 44). The increased oxygen content on the surface after PEGDA coating is consistent with the high oxygen content in PEG affecting the surface atom composition. The relatively high oxygen content on the untreated surface and the small amount of nitrogen is due to the treatment performed by ibidi: The chips are treated by ibidi with a physical treatment (ibiTreat[133]) to create a hydrophilic surface similar to culture flasks and Petri dishes for cell culture. We also tested the outer surface of the ibidi chip and, as expected, found polyethylene had 100 % carbon content. After surface coating with PEGDA the 2PP fabricated PEGDA constructs showed excellent adhesion to the surface of the chip.

The resin used for 2PP of PEGDA constructs contained 16 % wt 1 kDa PEGDA and 3 % wt Irgacure 369 dissolved in PEG (350 Da) and 1 mM 6-aminofluorescein for visualization, all from Sigma Aldrich. 70/30 ethanol/water was used as a developer for the finished constructs.

To realize woodpile constructs similar to those produced in IP-L we had to make adjustments for the less effective 2PP photoinitiator and slower cross linking in our PEGDA resin. Similar methods as presented above for the 2PP of the IP-L constructs were used with the PEGDA resin. 3D confocal reconstructions were created as described above from confocal stacks acquired with a Zeiss LSM 5 and processed with imageJ[90] software.

The woodpile constructs were reduced in size to a 50 x 50 μm^2 footprint to compensate for the slower writing speed. The writing parameters were changed as follows to increase structural rigidity as much as possible:

Update rate/writing speed: The update rate was slowed down to 600 giving a writing speed of 120 µm/min to achieve optimal polymerization. This increased the overall writing time to one hour for a 50 x 50 x 70 μm^3 woodpile construct.

Laser power: The laser power was adjusted to 70 % because the slower writing speed increased bubble formation and damage at higher power settings.

Line distance: By reducing the line distance to 150 nm the overlap of the individual lines were increased to improve structural rigidity.

Layer distance/ z distance: The z distance was reduced to 1 µm to increase the overlap between individual layers.

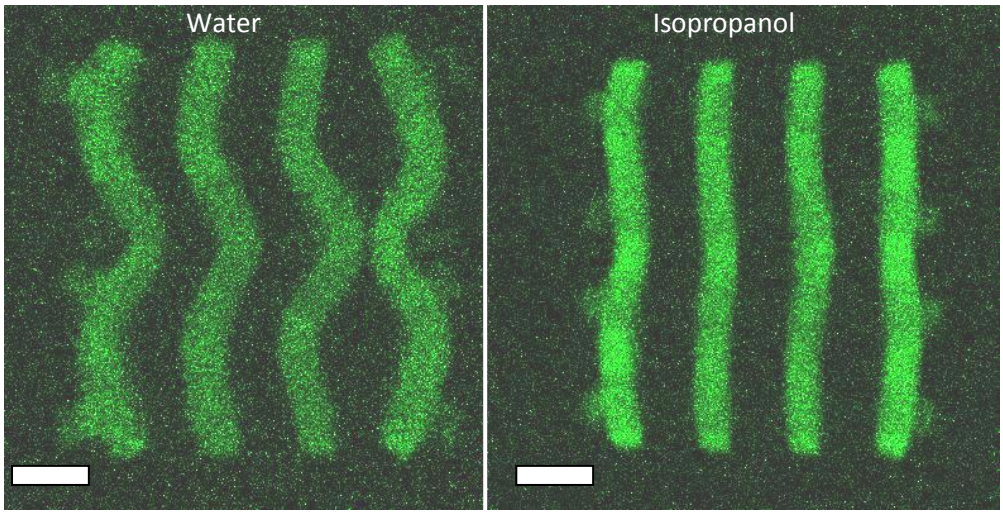

Figure 45 Confocal micrograph showing the bottom layer of a woodpile construct with 10x4 µm beams immersed in two different solvents, water and isopropanol. Swelling in water distorts the beams and causes them to bend. Bending in isopropanol is almost negligible. Scale bars are 10 µm.

The woodpile constructs with 10x4 μm^2 beams showed clear signs of solvent dependent swelling. Figure 45 shows confocal micrographs of the bottom layer of a 3 layer woodpile with a 50x50 μm^2 footprint immersed in water or in isopropanol. Immersion in water results in substantial bending due to swelling, while only slight bending is observed in ispopropanol. Water is a better solvent for PEG than isopropanol due to the higher dipole moment. Woodpile constructs with beams measuring 6 µm, 8 µm and 10 µm in width, the last being square in cross-section, were fabricated to evaluate the effect on the swelling induced bending.

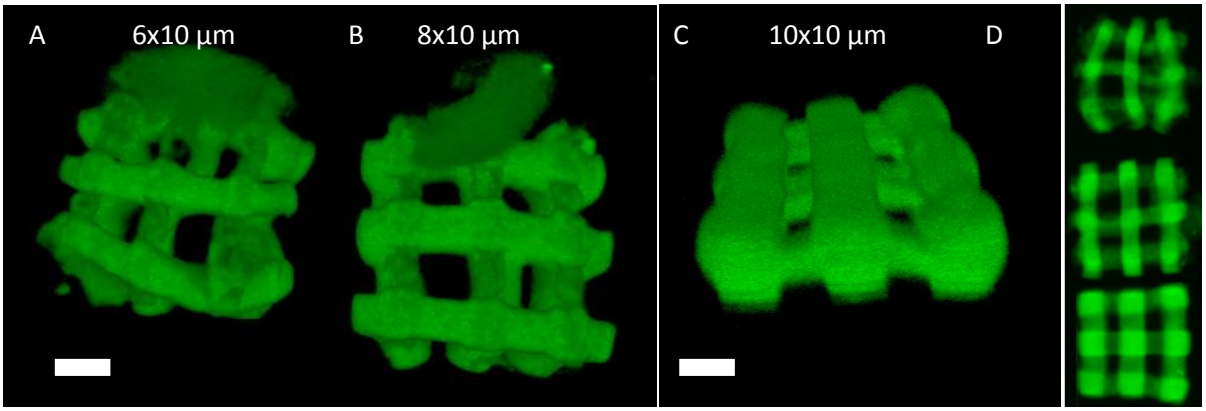

Figure 46 Confocal 3D reconstructions (A-C) and z projection (D) of 2PP fabricated hydrogel woodpile constructs. Wider beams decrease swelling distortion on PEGDA woodpile constructs. A polymerized blob is seen in both (A) and (B) hovering over the constructs, and is believed to be remnants of the last three layers that were not polymerized properly. In (C) no extra blob is observed because only three layers were written, but it was a general tendency that no more than three layers could be made. (D) shows a z-projection of the three image stacks to illustrate the increased structural stability gained from the widened beams. Scale bars are 10 µm.

Figure 46 displays that increasing the cross-section of the beams to 10x10 μm^2 made them more stable than beams of 4x10 μm^2, 6x10 μm^2 or 8x10 μm^2. The change in beam width also meant that the porosity of the fabricated structures were changed, thereby increasing the volume that needed to be polymerized and thus further increasing the writing time. The writing time of a 50x50x70 μm^3 (to fill the ibidi channel) increased to two hours. Figure 46 (A) and (B) show that remnants of the higher layers (4-6) were forming an aggregate of partly polymerized hydrogel hovering above the three bottom layers without any stable contact to the rest of the woodpile. No aggregation is observed in (C) since only three layers of the 10x10 μm^2 beam woodpile were written to illustrate the higher beam rigidity. In the z projections in (D) it is clearly seen that, as expected, increasing the width of the beams increased the structural rigidity of the construct.

Several other writing configurations were tried to increase structural rigidity and decrease the swelling effect. Increasing the overlap between the woodpile layers from the 1.3 µm overlap inherent from the voxel height to an overlap of 3.3 µm by increasing the beam height to 12 µm, did not improve stability. Finally it was believed that some of the bending happening during polymerization could be avoided if the whole woodpile was build one layer at a time, thereby stabilizing the already polymerized beams better during construction. This change of writing sequence did not yield better results either. It was not possible to construct woodpiles more than three layers in height (30 µm) and the writing speed of the woodpiles,

with the only stable 10x10 μm^2 beams, was so slow that it became clear that 3D shaping of soft hydrogels with this formulation and experimental setup was not optimal.

3.5. Discussion

3.5.1. Tuning PEGDA hydrogel properties

Bulk PEGDA hydrogels with mechanical properties in the range relevant for tissue engineering especially for soft tissue have been shown, and control of swelling behavior and thus of the mechanical properties has also been demonstrated. Conjugating of a RGD peptide sequence and the protein Streptavidin-Alexa488 to PEG macromers via a NHS coupling reaction is presented. The coupling reactions were confirmed with both mass spectrometry and with functional assays, but the coupling yield was in both cases far from 100 % . Purification of the coupling products was not performed, mainly because the PEGDA hydrogel platform is protein repellant and therefore inhibits non-specific adsorption to the surface or in the network. This material property allows for easy washing procedures and also allows for easy confirmation of covalently linked products as demonstrated with the green fluorescent Alexa488 streptavidin conjugate that is clearly seen forming stripes on the hydrogel surface. It could be argued that the remaining unreacted macromers would take up some of the available reactive spots in the network and leave too few for the functionalized macromers. However, the concentration of polymer chains in the network is far beyond what would be needed for RGD motifs to mediate cell adhesion[134] so the RGD concentration of 50 % pure product is more than sufficient. By introducing more advanced lithography processes such as gray scale masks and 2PP systems, gradients and 3D patterns can be realized. By utilizing the ibidi chip microfluidic system, gradients inside PEGDA hydrogels could be created as presented with collagen in section 2 of this thesis. Surface gradients would even be obtainable on 3D hydrogel constructs (optimization of fabrication procedure needed) inside the microchannel creating new possibilities for studying cellular phenomena dependent on mechanical, chemical or geometrical properties of the scaffold. One application of such a system would be to build on the IP-L based system presented above. The DCs could be tested against conjugated chemokine gradients for guiding haptotactic migration to more accurately mimic the presented *in vivo* homing scenario[8,135].

3.5.2. Fabricating in chip 3D hydrogel constructs

The in-chip setup that proved successful for testing DC migratory behavior, can also be used with a PEGDA based resin for making soft 3D in-chip constructs. By modifying the surface of the ibidi chip with PEGDA and thereby increasing adhesion of 2PP fabricated hydrogel constructs we successfully created soft 3D constructs inside the ibidi chip. The stability and structural rigidity of the fabricated constructs are not very good and constructs covering the entire height of the channel (70 µm) were not achieved. Woodpile constructs higher than 30 µm did not polymerize sufficiently to sustain the development step. Furthermore the constructs did show considerable post polymerization swelling that compromised the structural geometry making the fabricated constructs unusable for migration experiments. Increasing the beam cross section to 10x10 μm^2 enhanced the stability and reduced the distortion from the swelling to a minimum. To achieve these hydrogel constructs the writing parameters had to be adjusted compared to the optimized parameters used for the writing of IP-L woodpile constructs. Most noteworthy was the reduction in writing speed from up to 1200 µm/s to only 120 µm/s together with the increased width of the beams which meant that the overall fabrication time was increased between 10 and 20 times. These adjustments to the fabrication parameters are not acceptable, and combined with the still palpable stability issues with the constructs it must be concluded that, this formulation is not suited for 3D 2PP with our system.
The unsuccessful fabrication process may have several causes. All previously published work on 2PP of PEGDA with Irgacure369 have used 100 % PEGDA i.e. without added solvent, at the cost of much stiffer resulting hydrogels. The lower macromer concentration in our resin will drastically decrease the polymerization rate which can be assumed to be linearly dependent on the acrylate concentration[64]. To the best of our knowledge only two successful attempts has been made to polymerize 3D PEGDA constructs with water present in the resin. Both used slightly shorter PEGDA macromers and utilized either a custom synthesized hydrophilic photoinitiator[130] or a surfactant to dissolve the photoinitiator[131]. We tried the latter option with Irgacure 369, but with little success.
With a more effective 2PP photo initiation system it is believed that 3D PEGDA constructs can be tailored to many applications, and the in-chip setup allows for gradient formation which are found very important in mimicking the *in vivo* cell environment[136]. Combining the material flexibility in both chemical and mechanical terms with the in-chip manufacturing methods presented in this thesis with an effective water soluble 2-photon photoinitiator should enable us to construct 3D cell migration scaffolds with tunable mechanical stiffness and chemokine gradients for immune cell migration studies.

4. Conclusion

In this thesis two approaches to build 3D migration constructs are presented, one using the commercial resin IP-L for hard topology constructs and one using a custom soft PEGDA hydrogel resin that should allow full mechanical and chemical control over the construct. Both approaches utilize in-chip two-photon polymerization that combines the best of two chip fabrication approaches:
(1) Fast low-definition 2D macroscopic scale production of microchannel chip compatible with conventional optical analysis and standardized connectors interfacing to the surroundings; (2) Slower high-definition 3D fabrication of small volume application-specific components. By fabricating the constructs in-chip the need for subsequent chip bonding processes is avoided. These often require extensive optimization to avoid leakage and may easily damage fragile micro- or nanostructures present at the chip surfaces to be bonded.

When using the commercial hard IP-L resin we show accurate control of both the pore size and the topology experienced by the migrating cells in a material that does not appear to affect their migratory behavior. By adjusting the pore size in the woodpile constructs the DCs are prone to change behavior and are possibly doing full 3D spiral turns when navigating the constructs. We also present confined migration through microchannels in a controlled gradient. When the DCs migrate through microchannels of varying diameters the DCs show a clear jump in migration speed when they completely occlude the channel. This is most likely a combination of a changed migration mode and a steeper chemokine gradient created over the cells in the occluded channels. The migration speed of the DCs is simultaneously measured inside confined microchannels and in the surrounding collagen matrix giving an unprecedented comparison of confined migration and migration through a collagen matrix under identical conditions in the same chamber.

Using the custom PEGDA resin the fabricated constructs are successfully integrated in the ibidi chip. The constructs are not well defined and show considerable post swelling leading to distorted constructs unable to fill the entire channel in the ibidi chip not suitable for migratory analysis. Bulk modifications of the mechanical and chemical properties of the hydrogel are presented. Control over equilibrium degree of swelling yielding mechanical properties similar to a range of tissues is demonstrated. Repeated photo patterning of biomolecules are shown and a suitable response by 3T3 cells is also shown once. Though the work on 3D fabrication as well as biochemical modification of the hydrogels need further optimization, it is believed that 3D hydrogel constructs can be realized with a more effective photo initiator, such as the one utilized by Torgersen et al.[130]. The hydrogel constructs will contribute to the existing migration scaffolds by introducing a soft 3D shaped hydrous construct biochemically customizable to a specific need.

The source/sink design of the ibidi chip gives complete control of the concentration and thus the steepness of the chemokine gradient. Combining the above aspects with easy visualization and cell tracking through the thin bottom adds up to a very versatile and easy to use migration analysis system. The collagenase regeneration procedure strongly reduces the cost per experiment of the IP-L produced constructs and thus compensates for the higher expense of 2PP fabrication.

Applications of a migration screening platform for dendritic cells are wanted at hospitals and clinics working with cancer immunotherapy. DC migration is a vital part of the immune system and in cancer vaccines in particular a huge effort is being made towards achieving the perfect DC maturation cocktail. In the effort towards finding the most effective cocktail that simultaneously produces effective immunogenic DCs and DCs with a high migration potential a reliable migration screening platform is vital. The immunogenicity of the DCs is very much dependent on their ability to navigate to the lymph nodes and inside the lymph nodes. The Boyden chambers used now, where the cells navigate through a 10 μm thin membrane, offer poor resemblance with the *in*-vivo environment.
Our presented system offers a customizable environment that can be tailored to mimic a specific situation *in-vivo*. A relevant example is the entrance into the lymphatic vessels that occur via small preformed pores in the vessel. Such geometry will be easy to reproduce with the 2PP system by incorporating vessel shaped and pore filled channels into known scaffold geometry. Thereby the DCs will encounter a situation *in-vitro* - very similar to what they will *in-vivo,* increasing the possibility for the investigators to isolate a specific cell response to a given treatment.
We foresee that our in-chip designed reusable migration constructs can be employed both for optimizing cell processing conditions to maximize in vivo chemotaxis of DCs and for validating the migratory potential of each patient's cells in immunotherapy.

5. Outlook

Further development of the presented migration platform is needed to better mimic the *in-vivo* environment which the DCs encounter when migrating towards the lymph nodes. Hard migration constructs can be fabricated with the commercial IP-L resin in almost any geometric shape. Combined with the gradient formed by the ibidi chip and the easy fluid exchange it will offer a unique control over the environment experienced by the cells as well as easy handling in the clinic. To develop the IP-L based constructs it is worth determining if the acrylate based resin maintains unreacted acrylate moieties that can be used for surface modification with biomolecules. The PEGDA hydrogels have proven suitable for modification of the acrylate moieties remaining after polymerization and it will most likely be the same for the IP-L resin. Modification of the hard IP-L scaffolds with gradients of biomolecules such as RGD peptides or chemokine motifs would vastly increase the versatility of the system and enhance the resemblance with the *in-vivo* environment. A suitable spacer is needed when anchoring the biomolecules and the Acr-PEG-NHS chemistry presented in this thesis and, utilized widely, it would be a good starting point to test the opportunities for post polymerization surface modification of the IP-L resin. Employing this strategy would also allow the cells to traverse the scaffolds without collagen present because adhesion motifs can be attached to the surface of the scaffold. This would mean that the migration ability of the DCs could be tested with and without adhesion motifs on the surface to further investigate the integrin dependency of 3D migration in a more controlled environment, as initialized by Lämmermann et al.[17].

Optimizing the 3D processing of the PEGDA constructs is essential to obtain results applicable to migration studies. By introducing a more effective water soluble 2PP photo initiator, such as the one presented by Torgersen et al.[130], the processability of the PEGDA resin would be much improved. A better photo initiator will increase the crosslinking density and by doing so the swelling of the fabricated constructs can be reduced enough to obtain 3D structures suitable for migration purposes. The soft water containing constructs would add a mechanical dimension to the tissue mimicking property space of the migration platform and could build on experiences learned from the more mature IP-L platform.

Recently 2PP systems with increased writing speed have been developed[83,84] and all technical progress that will lower cost and fabrication time of the individual scaffolds is a huge benefit for the relatively slow and expensive 2PP process. If soft hydrogel 2PP constructs shall evolve into a widely used fast prototyping technology it is necessary to combine the newly presented systems with further improvement of water containing resin processability. At the moment the technology is slow and expensive, but there are many opportunities for developing new and improved migration systems.

6. References

1. Kalinski, P., Muthuswamy, R. & Urban, J. Dendritic cells in cancer immunotherapy: vaccines and combination immunotherapies. *Expert review of vaccines* **12,** 285–95 (2013).

2. Van Brussel, I., Berneman, Z. N. & Cools, N. Optimizing dendritic cell-based immunotherapy: tackling the complexity of different arms of the immune system. *Mediators of inflammation* **2012,** 690643 (2012).

3. Engell-Noerregaard, L., Hansen, T. H., Andersen, M. H., Thor Straten, P. & Svane, I. M. Review of clinical studies on dendritic cell-based vaccination of patients with malignant melanoma: assessment of correlation between clinical response and vaccine parameters. *Cancer immunology, immunotherapy* **58,** 1–14 (2009).

4. Mellman, I., Coukos, G. & Dranoff, G. Cancer immunotherapy comes of age. *Nature* **480,** 480–9 (2011).

5. Schuler, G. Dendritic cells in cancer immunotherapy. *European journal of immunology* **40,** 2123–30 (2010).

6. Verdijk, P. *et al.* Limited amounts of dendritic cells migrate into the T-cell area of lymph nodes but have high immune activating potential in melanoma patients. *Clinical cancer research* **15,** 2531–40 (2009).

7. Tal, O. *et al.* DC mobilization from the skin requires docking to immobilized CCL21 on lymphatic endothelium and intralymphatic crawling. *The Journal of experimental medicine* **208,** 2141–53 (2011).

8. Weber, M. *et al.* Interstitial dendritic cell guidance by haptotactic chemokine gradients. *Science* **339,** 328–32 (2013).

9. Cavanagh, L. L. & Weninger, W. Dendritic cell behaviour in vivo: lessons learned from intravital two-photon microscopy. *Immunology and cell biology* **86,** 428–38 (2008).

10. Friedl, P. & Weigelin, B. Interstitial leukocyte migration and immune function. *Nature immunology* **9,** 960–9 (2008).

11. Pflicke, H. & Sixt, M. Preformed portals facilitate dendritic cell entry into afferent lymphatic vessels. *The Journal of experimental medicine* **206,** 2925–35 (2009).

12. Cukierman, E., Pankov, R., Stevens, D. R. & Yamada, K. M. Taking cell-matrix adhesions to the third dimension. *Science* **294,** 1708–12 (2001).

13. Cukierman, E., Pankov, R. & Yamada, K. M. Cell interactions with three-dimensional matrices. *Current opinion in cell biology* **14,** 633–9 (2002).

14. Pedersen, J. a & Swartz, M. a. Mechanobiology in the third dimension. *Annals of biomedical engineering* **33,** 1469–90 (2005).

15. Lämmermann, T. & Sixt, M. Mechanical modes of “amoeboid” cell migration. *Current opinion in cell biology* **21,** 636–44 (2009).

16. Friedl, P. & Wolf, K. Plasticity of cell migration: a multiscale tuning model. *The Journal of cell biology* **188,** 11–9 (2010).

17. Lämmermann, T. *et al.* Rapid leukocyte migration by integrin-independent flowing and squeezing. *Nature* **453,** 51–5 (2008).

18. Friedl, P., Wolf, K. & Lammerding, J. Nuclear mechanics during cell migration. *Current opinion in cell biology* **23,** 55–64 (2011).

19. Wolf, K. *et al.* Physical limits of cell migration: Control by ECM space and nuclear deformation and tuning by proteolysis and traction force. *The Journal of cell biology* **201,** 1069–84 (2013).

20. Kim, H.-D. & Peyton, S. R. Bio-inspired materials for parsing matrix physicochemical control of cell migration: a review. *Integrative biology* **4,** 37–52 (2012).

21. Lee, K. Y. & Mooney, D. J. Hydrogels for Tissue Engineering. *Chemical Reviews* **101,** 1869–1880 (2001).

22. Slaughter, B. V, Khurshid, S. S., Fisher, O. Z., Khademhosseini, A. & Peppas, N. a. Hydrogels in regenerative medicine. *Advanced materials* **21,** 3307–29 (2009).

23. Kloxin, A. M., Kasko, A. M., Salinas, C. N. & Anseth, K. S. Photodegradable hydrogels for dynamic tuning of physical and chemical properties. *Science* **324,** 59–63 (2009).

24. Hahn, M. S. *et al.* Photolithographic patterning of polyethylene glycol hydrogels. *Biomaterials* **27,** 2519–24 (2006).

25. Culver, J. C. *et al.* Three-dimensional biomimetic patterning in hydrogels to guide cellular organization. *Advanced materials* **24,** 2344–8 (2012).

26. Guillame-Gentil, O. *et al.* Engineering the extracellular environment: Strategies for building 2D and 3D cellular structures. *Advanced materials* **22,** 5443–62 (2010).

27. Kumar, G. *et al.* The determination of stem cell fate by 3D scaffold structures through the control of cell shape. *Biomaterials* **32,** 9188–96 (2011).

28. Kotov, N. A. *et al.* Inverted Colloidal Crystals as Three-Dimensional Cell Scaffolds. *Langmuir* **20,** 7887–7892 (2004).

29. Stachowiak, A. N. & Irvine, D. J. Inverse opal hydrogel-collagen composite scaffolds as a supportive microenvironment for immune cell migration. *Journal of biomedical materials research. Part A* **85,** 815–28 (2008).

30. Stachowiak, a. N., Bershteyn, A., Tzatzalos, E. & Irvine, D. J. Bioactive Hydrogels with an Ordered Cellular Structure Combine Interconnected Macroporosity and Robust Mechanical Properties. *Advanced Materials* **17,** 399–403 (2005).

31. Zhang, Y. & Xia, Y. Formation of Embryoid Bodies with Controlled Sizes and Maintained Pluripotency in Three-Dimensional Inverse Opal Scaffolds. *Advanced Functional Materials* **22,** 121–129 (2012).

32. Choi, S.-W., Xie, J. & Xia, Y. Chitosan-Based Inverse Opals: Three-Dimensional Scaffolds with Uniform Pore Structures for Cell Culture. *Advanced materials* **21,** 2997–3001 (2009).

33. Greiner, A. M., Richter, B. & Bastmeyer, M. Micro-engineered 3D scaffolds for cell culture studies. *Macromolecular bioscience* **12,** 1301–14 (2012).

34. Melchels, F. P. W., Feijen, J. & Grijpma, D. W. A review on stereolithography and its applications in biomedical engineering. *Biomaterials* **31,** 6121–30 (2010).

35. Chan, V., Zorlutuna, P., Jeong, J. H., Kong, H. & Bashir, R. Three-dimensional photopatterning of hydrogels using stereolithography for long-term cell encapsulation. *Lab on a chip* **10,** 2062–70 (2010).

36. Zorlutuna, P., Jeong, J. H., Kong, H. & Bashir, R. Stereolithography-Based Hydrogel Microenvironments to Examine Cellular Interactions. *Advanced Functional Materials* **21,** 3642–3651 (2011).

37. Mapili, G., Lu, Y., Chen, S. & Roy, K. Laser-layered microfabrication of spatially patterned functionalized tissue-engineering scaffolds. *Journal of biomedical materials research B* **75,** 414–24 (2005).

38. Raimondi, M. T. *et al.* Two-photon laser polymerization: from fundamentals to biomedical application in tissue engineering and regenerative medicine. *Journal of Applied Biomaterials & Biomechanics* **10,** 55–65 (2012).

39. Narayan, R. J., Doraiswamy, A., Chrisey, D. B. & Chichkov, B. N. Medical prototyping using two photon polymerization. *Materials Today* **13,** 42–48 (2010).

40. Klein, F. *et al.* Two-component polymer scaffolds for controlled three-dimensional cell culture. *Advanced materials* **23,** 1341–5 (2011).

41. Maruo, S., Nakamura, O. & Kawata, S. Three-dimensional microfabrication with two-photon-absorbed photopolymerization. *Optics letters* **22,** 132–4 (1997).

42. Erskine, L. L. *et al.* Two-photon polymerization initiators for three- dimensional optical data storage and microfabrication. *Nature* **398,** 51–54 (1999).

43. Sun, H.-B., Matsuo, S. & Misawa, H. Three-dimensional photonic crystal structures achieved with two-photon-absorption photopolymerization of resin. *Applied Physics Letters* **74,** 786 (1999).

44. Guo, R. *et al.* Micro lens fabrication by means of femtosecond two photon photopolymerization. *Optics express* **14,** 810–6 (2006).

45. LaFratta, C. N., Fourkas, J. T., Baldacchini, T. & Farrer, R. a. Multiphoton fabrication. *Angewandte Chemie (International ed.)* **46,** 6238–58 (2007).

46. Wu, D. *et al.* Femtosecond laser rapid prototyping of nanoshells and suspending components towards microfluidic devices. *Lab on a chip* **9,** 2391–4 (2009).

47. Sun, H. B. *et al.* Real three-dimensional microstructures fabricated by photopolymerization of resins through two-photon absorption. *Optics letters* **25,** 1110–2 (2000).

48. Kumi, G., Yanez, C. O., Belfield, K. D. & Fourkas, J. T. High-speed multiphoton absorption polymerization: fabrication of microfluidic channels with arbitrary cross-sections and high aspect ratios. *Lab on a chip* **10,** 1057–60 (2010).

49. Wang, J. *et al.* Embellishment of microfluidic devices via femtosecond laser micronanofabrication for chip functionalization. *Lab on a chip* **10,** 1993–6 (2010).

50. Xu, B.-B. *et al.* Fabrication and multifunction integration of microfluidic chips by femtosecond laser direct writing. *Lab on a chip* **13,** 1677–90 (2013).

51. Kawata, S., Sun, H. B., Tanaka, T. & Takada, K. Finer features for functional microdevices. *Nature* **412,** 697–8 (2001).

52. Leventon, W. One-Step Fabbing Two-photon polymerization: one-step process for fabricating 3-D structures. *Micromanufacturing* **3,** 25–29 (2010).

53. Serbin, J. *et al.* Femtosecond laser-induced two-photon polymerization of inorganic-organic hybrid materials for applications in photonics. *Optics letters* **28,** 301–3 (2003).

54. Ovsianikov, a *et al.* Laser printing of cells into 3D scaffolds. *Biofabrication* **2,** 014104 (2010).

55. Tayalia, P., Mendonca, C. R., Baldacchini, T., Mooney, D. J. & Mazur, E. 3D Cell-Migration Studies using Two-Photon Engineered Polymer Scaffolds. *Advanced Materials* **20,** 4494–4498 (2008).

56. Klein, F. *et al.* Elastic fully three-dimensional microstructure scaffolds for cell force measurements. *Advanced materials* **22,** 868–71 (2010).

57. Valeur, B. *Molecular Fluorescence: Principles and Applications*. **8,** 250 (Wiley-VCH, 2001).

58. Wu, S., Serbin, J. & Gu, M. Two-photon polymerisation for three-dimensional micro-fabrication. *Journal of Photochemistry and Photobiology A* **181,** 1–11 (2006).

59. Ovsianikov, A. & Chichkov, B. N. in *Nanoelectronics and Photonics* (Korkin, A. & Rosei, F.) 427–446 (Springer New York, 2008). doi:10.1007/978-0-387-76499-3

60. Bhawalkar, J. D., He, G. S. & Prasad, P. N. Nonlinear multiphoton processes in organic and polymeric materials. *Reports on Progress in Physics* **59,** 1041–1070 (1996).

61. Göppert-Mayer, M. Über Elementarakte mit zwei Quantensprüngen. *Annalen der Physik* **401,** 273–294 (1931).

62. Woo, H. Y. *et al.* Solvent Effects on the Two-Photon Absorption of Distyrylbenzene Chromophores Emerging technologies such as memory storage , photody-. *Jounal of American Chemical Society* **127,** 14721–14729 (2005).

63. Li, Z. *et al.* A Straightforward Synthesis and Structure–Activity Relationship of Highly Efficient Initiators for Two-Photon Polymerization. *Macromolecules* **46,** 352–361 (2013).

64. Fried, J. *Polymer Science and Technology (2nd Edition)*. 608 (Prentice Hall, 2003). at <http://www.amazon.com/Polymer-Science-Technology-2nd-Edition/dp/0130181684>

65. Zipfel, W. R., Williams, R. M. & Webb, W. W. Nonlinear magic: multiphoton microscopy in the biosciences. *Nature biotechnology* **21,** 1369–77 (2003).

66. Sun, H.-B. *et al.* Experimental investigation of single voxels for laser nanofabrication via two-photon photopolymerization. *Applied Physics Letters* **83,** 819 (2003).

67. Sun, H.-B., Takada, K., Kim, M.-S., Lee, K.-S. & Kawata, S. Scaling laws of voxels in two-photon photopolymerization nanofabrication. *Applied Physics Letters* **83,** 1104 (2003).

68. Maruo, S. & Fourkas, J. T. Recent progress in multiphoton microfabrication. *Laser & Photonics Review* **2,** 100–111 (2008).

69. Haske, W. *et al.* 65 nm feature sizes using visible wavelength 3-D multiphoton lithography. *Optics express* **15,** 3426–36 (2007).

70. Tan, D. *et al.* Reduction in feature size of two-photon polymerization using SCR500. *Applied Physics Letters* **90,** 071106 (2007).

71. Ovsianikov, A., Schlie, S., Ngezahayo, A., Haverich, A. & Chichkov, B. N. Two-photon polymerization technique for microfabrication of CAD-designed 3D scaffolds from commercially available photosensitive materials. *Journal of tissue engineering and regenerative medicine* **1,** 443–449 (2007).

72. Ovsianikov, a *et al.* Three-dimensional laser micro- and nano-structuring of acrylated poly(ethylene glycol) materials and evaluation of their cytoxicity for tissue engineering applications. *Acta biomaterialia* **7,** 967–74 (2011).

73. Melissinaki, V. *et al.* Direct laser writing of 3D scaffolds for neural tissue engineering applications. *Biofabrication* **3,** 045005 (2011).

74. Weiss, T. *et al.* Two-Photon Polymerization of Biocompatible Photopolymers for Microstructured 3D Biointerfaces. *Advanced Engineering Materials* **13,** B264–B273 (2011).

75. Weiss, T., Hildebrand, G., Schade, R. & Liefeith, K. Two-Photon polymerization for microfabrication of three-dimensional scaffolds for tissue engineering application. *Engineering in Life Sciences* **9,** 384–390 (2009).

76. Tayalia, P., Mazur, E. & Mooney, D. J. Controlled architectural and chemotactic studies of 3D cell migration. *Biomaterials* **32,** 2634–41 (2011).

77. Claeyssens, F. *et al.* Three-dimensional biodegradable structures fabricated by two-photon polymerization. *Langmuir* **25,** 3219–23 (2009).

78. Ovsianikov, A. *et al.* Laser fabrication of three-dimensional CAD scaffolds from photosensitive gelatin for applications in tissue engineering. *Biomacromolecules* **12,** 851–8 (2011).

79. Käpylä, E. *et al.* Direct laser writing and geometrical analysis of scaffolds with designed pore architecture for three-dimensional cell culturing. *Journal of Micromechanics and Microengineering* **22,** 115016 (2012).

80. Malinauskas, M. *et al.* 3D artificial polymeric scaffolds for stem cell growth fabricated by femtosecond laser. *Lithuanian Journal of Physics* **50,** 75–82 (2010).

81. Iosin, M. *et al.* Laser microstructuration of three-dimensional enzyme reactors in microfluidic channels. *Microfluidics and Nanofluidics* **10,** 685–690 (2010).

82. Amato, L. *et al.* Integrated three-dimensional filter separates nanoscale from microscale elements in a microfluidic chip. *Lab on a chip* **12,** 1135–42 (2012).

83. Http://www.tuwien.ac.at/en/news/news_detail/article/7444/. Technische Universität Wien : 3D-Printer with Nano-Precision. at <http://www.tuwien.ac.at/en/news/news_detail/article/7444/>

84. http://www.nanoscribe.de/en/products/photonic-professional-gt. Nanoscribe GmbH: True 3D Laser Lithography. at <http://www.nanoscribe.de/en/products/photonic-professional-gt>

85. LaFratta, C. & Baldacchini, T. Replication of two-photon-polymerized structures with extremely high aspect ratios and large overhangs. *The Journal of Physical Chemistry B* 11256–11258 (2004). at <http://pubs.acs.org/doi/abs/10.1021/jp048525r>

86. LaFratta, C. N., Li, L. & Fourkas, J. T. Soft-lithographic replication of 3D microstructures with closed loops. *Proceedings of the National Academy of Sciences of the United States of America* **103,** 8589–94 (2006).

87. Koroleva, A. *et al.* Two-photon polymerization-generated and micromolding-replicated 3D scaffolds for peripheral neural tissue engineering applications. *Biofabrication* **4,** 025005 (2012).

88. Olsen, M. H., Hjortø, M., Hansen, M., Met, Ö. & Svane, M. In-chip fabrication of free-form 3D constructs for directed cell migration analysis. *Lab on a chip* **?,** ? (2013).

89. Larsen, E. K. U. & Larsen, N. B. One-step polymer surface modification for minimizing drug, protein, and DNA adsorption in microanalytical systems. *Lab on a chip* **13,** 669–75 (2013).

90. ImageJ, U.S. National Institutes of Health, Bethesda, Maryland, USA. *ImageJ, U.S. National Institutes of Health, Bethesda, Maryland, USA http://rsbweb.nih.gov/ij/* at <http://rsbweb.nih.gov/ij/>

91. Williams, C. G., Malik, A. N., Kim, T. K., Manson, P. N. & Elisseeff, J. H. Variable cytocompatibility of six cell lines with photoinitiators used for polymerizing hydrogels and cell encapsulation. *Biomaterials* **26,** 1211–8 (2005).

92. Gradient Stability :: ibidi. at <http://ibidi.com/applications/chemotaxis/gradient-stability/>

93. Hoogschagen, J. Diffusion in Porous Catalysts and Adsorbents. *Industrial & Engineering Chemistry* **47,** 906–912 (1955).

94. Brakel, J. V. A. N. & Heertjes, P. M. ANALYSIS OF DIFFUSION IN MACROPOROUS MEDIA IN TERMS OF A POROSITY , A TORTUOSITY AND A CONSTRICTIVITY FACTOR XA RSA + XB / (MA CrB ~. *Int. J. Heat Mass Transfer* **17,** 1093–1103 (1974).

95. Wolf, K. *et al.* Collagen-based cell migration models in vitro and in vivo. *Seminars in cell & developmental biology* **20,** 931–41 (2009).

96. Weber, M. *et al.* Interstitial dendritic cell guidance by haptotactic chemokine gradients. *Science* **339,** 328–32 (2013).

97. Balzer, E. M. *et al.* Physical confinement alters tumor cell adhesion and migration phenotypes. *FASEB journal* **26,** 4045–56 (2012).

98. Tong, Z. *et al.* Chemotaxis of cell populations through confined spaces at single-cell resolution. *PloS one* **7,** e29211 (2012).

99. Hansen, M. *et al.* Comparison of clinical grade type 1 polarized and standard matured dendritic cells for cancer immunotherapy. *Vaccine* **31,** 639–46 (2013).

100. Frankenberger, B. & Schendel, D. J. Third generation dendritic cell vaccines for tumor immunotherapy. *European journal of cell biology* **91,** 53–8 (2012).

101. Irimia, D., Charras, G., Agrawal, N., Mitchison, T. & Toner, M. Polar stimulation and constrained cell migration in microfluidic channels. *Lab on a chip* **7,** 1783–90 (2007).

102. Faure-andré, G. *et al.* Regulation of Dendritic Cell Migration by CD74, the MHC Class II-Associated Invariant Chain. *Science* **322,** 1705–1710 (2008).

103. Yamada, K. M. & Cukierman, E. Modeling tissue morphogenesis and cancer in 3D. *Cell* **130,** 601–10 (2007).

104. Decaestecker, C., Debeir, O., Van Ham, P. & Kiss, R. Can anti-migratory drugs be screened in vitro? A review of 2D and 3D assays for the quantitative analysis of cell migration. *Medicinal research reviews* **27,** 149–76 (2007).

105. Alemán, J. *et al.* Definitions of terms relating to the structure and processing of sols, gels, networks, and inorganic-organic hybrid materials (IUPAC Recommendations 2007). *Pure and Applied Chemistry* **79,** 1801–1829 (2007).

106. Larsen, E. K. U. & Larsen, N. B. One-step polymer surface modification for minimizing drug, protein, and DNA adsorption in microanalytical systems. *Lab on a chip* **13,** 669–75 (2013).

107. Bryant, S. J. & Anseth, K. S. in *Scaffolding in Tissue Engineering* 71–90 (Taylor & Francis Group, LLC, 2006).

108. Nguyen, Q. T., Hwang, Y., Chen, A. C., Varghese, S. & Sah, R. L. Biomaterials Cartilage-like mechanical properties of poly (ethylene glycol) -diacrylate hydrogels. *Biomaterials* **33,** 6682–6690 (2012).

109. Gnanou, Y., Hild, G. & Rempp, P. Molecular Structure and Elastic Behavior of Poly(ethy1ene oxide) Networks Swollen to Equilibrium. *Macromolecules* **20,** 1662–1671 (1987).

110. Bryant, S. J., Chowdhury, T. T., Lee, D. a, Bader, D. L. & Anseth, K. S. Crosslinking density influences chondrocyte metabolism in dynamically loaded photocrosslinked poly(ethylene glycol) hydrogels. *Annals of biomedical engineering* **32,** 407–17 (2004).

111. McKee, C. T., Last, J. A., Russell, P. & Murphy, C. J. Indentation versus tensile measurements of Young's modulus for soft biological tissues. *Tissue engineering B* **17,** 155–64 (2011).

112. Roeder, B. a., Kokini, K., Sturgis, J. E., Robinson, J. P. & Voytik-Harbin, S. L. Tensile Mechanical Properties of Three-Dimensional Type I Collagen Extracellular Matrices With Varied Microstructure. *Journal of Biomechanical Engineering* **124,** 214 (2002).

113. Hahn, M. S., Miller, J. S. & West, J. L. Three-Dimensional Biochemical and Biomechanical Patterning of Hydrogels for Guiding Cell Behavior. *Advanced Materials* **18,** 2679–2684 (2006).

114. Lee, S.-H., Moon, J. J. & West, J. L. Three-dimensional micropatterning of bioactive hydrogels via two-photon laser scanning photolithography for guided 3D cell migration. *Biomaterials* **29,** 2962–8 (2008).

115. Burdick, J. a & Anseth, K. S. Photoencapsulation of osteoblasts in injectable RGD-modified PEG hydrogels for bone tissue engineering. *Biomaterials* **23,** 4315–23 (2002).

116. DeForest, C. a, Polizzotti, B. D. & Anseth, K. S. Sequential click reactions for synthesizing and patterning three-dimensional cell microenvironments. *Nature materials* **8,** 659–64 (2009).

117. Deforest, C. a, Sims, E. a & Anseth, K. S. Peptide-Functionalized Click Hydrogels with Independently Tunable Mechanics and Chemical Functionality for 3D Cell Culture. *Chemistry of materials* **22,** 4783–4790 (2010).

118. Masson, F., Decker, C., Andre, S. & Andrieu, X. UV-curable formulations for UV-transparent optical fiber coatings. *Progress in Organic Coatings* **49,** 1–12 (2004).

119. Schafer, K. J. *et al.* Two-photon absorption cross-sections of common photoinitiators. *Journal of Photochemistry and Photobiology A* **162,** 497–502 (2004).

120. Hume, P. S., Bowman, C. N. & Anseth, K. S. Functionalized PEG hydrogels through reactive dip-coating for the formation of immunoactive barriers. *Biomaterials* **32,** 6204–12 (2011).

121. Merrill, E. W., Dennison, K. a & Sung, C. Partitioning and diffusion of solutes in hydrogels of poly(ethylene oxide). *Biomaterials* **14,** 1117–26 (1993).

122. Canal, T. & Peppas, N. A. Correlation between mesh size and equilibrium degree of swelling of polymeric networks. *Journal of biomedical materials research* **23,** 1183–1193 (1989).

123. Anseth, K. S., Bowman, C. N. & Brannon-Peppas, L. Mechanical properties of hydrogels and their experimental determination. *Biomaterials* **17,** 1647–57 (1996).

124. Gunn, J. W., Turner, S. D. & Mann, B. K. Adhesive and mechanical properties of hydrogels influence neurite extension. *Journal of biomedical materials research. Part A* **72,** 91–7 (2005).

125. Peyton, S. R., Raub, C. B., Keschrumrus, V. P. & Putnam, A. J. The use of poly(ethylene glycol) hydrogels to investigate the impact of ECM chemistry and mechanics on smooth muscle cells. *Biomaterials* **27,** 4881–93 (2006).

126. Oberg, E., Jones, F. D., Horton, H. L. & Ryffel, H. H. *Machinery's Handbook (27th Edition) & Guide to Machinery's Handbook*. *Industrial Press* 260 ff (2004). at <http://app.knovel.com/web/toc.v/cid:kpMHEGMH0B/viewerType:toc/?>

127. Ricart, B. G., Yang, M. T., Hunter, C. A., Chen, C. S. & Hammer, D. A. Measuring traction forces of motile dendritic cells on micropost arrays. *Biophysical journal* **101,** 2620–8 (2011).

128. Sun, H. & Kawata, S. in *Advances in Polymer Science* 169–273 (2004). doi:10.1007/b94405

129. Strehmel, B. & Strehmel, V. *Advances in photochemistry Vol. 29*. **29,** 156–233 (John Wiley & Sons, Inc, 2007).

130. Torgersen, J. *et al.* Photo-sensitive hydrogels for three-dimensional laser microfabrication in the presence of whole organisms. *Journal of Biomedical Optics* **17,** 1–10 (2012).

131. Jhaveri, S. J. *et al.* Direct three-dimensional microfabrication of hydrogels via two-photon lithography in aqueous solution. *Chemistry of materials* **21,** 2003–2006 (2009).

132. Huang, Y., Szleifer, I. & Peppas, N. a. A Molecular Theory of Polymer Gels. *Macromolecules* **35,** 1373–1380 (2002).

133. Cell Culture Surfaces :: ibidi. at <http://ibidi.com/applications/technical-aspects-of-microscopy/cell-culture-surfaces/>

134. Guarnieri, D. *et al.* Covalently immobilized RGD gradient on PEG hydrogel scaffold influences cell migration parameters. *Acta biomaterialia* **6,** 2532–9 (2010).

135. Förster, R., Braun, A. & Worbs, T. Lymph node homing of T cells and dendritic cells via afferent lymphatics. *Trends in immunology* **33,** 271–80 (2012).

136. Lühmann, T. & Hall, H. Cell Guidance by 3D-Gradients in Hydrogel Matrices: Importance for Biomedical Applications. *Materials* **2,** 1058–1083 (2009).

Appendix 1

Cell lab protocols

Here follows the protocols involving cell handling for extraction, maturation and migration studies from Olsen et al.[88].

Generation of monocyte-derived dendritic cells

CellGro DC serum-free medium, GM-CSF, IL-4, IL-1β, TNF-α and IL-6 were all obtained from CellGenix (Freiburg, Germany). PGE_2 was obtained from Sigma-Aldrich. Iscoves modified Dulbecco's medium (IMDM), and human AB-Serum was acquired from Lonza (Basal, Switzerland), penicillin / streptomycin (P/S) and Fetal Bovine Serum (FBS) from Invitrogen (Life Technologies, Paisley, UK). $NaHCO_3$ solution (7.5%), 10x MEM solution, and collagenase (Clostridium Histolyticum, cell culture tested) were from Sigma-Aldrich, PureCol (collagen I) solution from Advanced Biomatrix (San Diego, CA) and CCL21 from R&D Systems (Minneapolis, MN). Leukapheresis was done on healthy blood donors after informed consent followed by separation using elutriation (Terumo BCT, Lakewood, CO) and subsequent freezing of monocytes (80-90% pure as determined by flow cytometry on CD14). Thawed monocytes with a viability >99% were cultured for five days in culture plates (Ø 21 cm) at $5 \cdot 10^5$ cells/ml in CellGro DC medium supplemented with 1000 U/ml GM-CSF and 250 U/ml IL-4 to produce immature DCs. Maturation of DCs was induced for two days by adding 1000 U/ml TNF-α, 1000 U/ml IL-1β, 1000 U/mL IL-6, and 1 µg/ml PGE_2. Harvest of DCs was performed by aspiration followed by cold incubation of the remaining cells in PBS with EDTA (5 mM) and subsequent scraping of cells followed by freezing of DCs in aliquots (90% human serum and 10 % DMSO).

Collagen gel and DC loading in chips with constructs

Mature DCs were thawed and transferred to pre-warmed IMDM, 10% FBS, 1% P/S. The DCs were centrifuged at 220g for 5 minutes. Medium with DMSO was removed and the cells were left to acclimatize for 30 minutes at room temperature in fresh medium. The cells were centrifuged and re-suspended at 4×10^6 cells/ml. A collagen mixture with cells was prepared according to the ibidi manual. Briefly, 10 µl of $NaHCO_3$ (7.5%) was mixed with 20 µl of 10 x MEM solution. After addition and mixing with 150 µl of PureCol solution, 90 µl of DC suspension was added and the mixture was applied to the chip for

polymerization at 37°C for 30 minutes (either 6 µl inside the ibidi channel or 60 µl in the sink reservoir). After collagen polymerization, the sink and source reservoirs were filled with medium alone and medium with added CCL21 (60 nM), respectively. In the cases where the cells were loaded in the sink reservoir, only the source reservoir was filled upon collagen polymerization. The final collagen concentration was 1.67 mg/ml.

Time-lapse microscopy of DC migration

We monitored DC migration using a custom made time lapse setup based on an inverted phase contrast microscope (Zeiss Axiovert 100, Oberkochen, Germany) with a 20x phase contrast objective. The plugged chip with loaded DCs was mounted on a computer controlled translation stage, holding a temperature controlled (37°C) humidified incubation chamber supplied with 5% CO_2 in air. This setup allowed tracking for several days. Analysis of cell migration in the X, Y and Z direction is in principle possible. However, the optical contrast was insufficient for allowing analysis in the Z direction, since the DCs during migration are often very long and slender with dendrite lengths of 100-300 µm and only a few µm in width and consequently a very small cell body. DC migration was tracked for approximately 48 hours. This is the time-span during which the gradient established inside the chip is reported to be stable.
Slight positional variations in the stage position during time-lapse recordings were corrected by use of the TurboStack plugin for ImageJ. The faint outlines of the DC dendrites within the microporous constructs were subsequently enhanced by subtracting the average (static) image of the construct from all images in the time-lapse sequence, and adding the subtracted images into the green channel of the recorded phase contrast images. Thus, the non-static cells will appear with a green tint in the final image sequences. Movies are provided of both the unprocessed and image processed time lapse sequences.

Collagenase treatment of construct

After experimentation, the IPL woodpile structures were collagenase treated for removal of collagen and cells: collagenase solution (0.5 mg/ml in PBS) was added to the reservoirs and the channel inlets of the chip. The chip was incubated for 1 hour at 37°C, the collagenase solution was withdrawn from the reservoirs, and the chip reservoirs were washed with water and then ethanol. Before reuse, the chip reservoirs were washed once more in sterile water, and the reservoirs and structures were completely emptied by applying suction to the channel after plugging the reservoir inlets.

Example of 2PP recipe (100x100x70 µm in-chip woodpile construct)

```
%Main job file 100x100x70 µm, 10x10 µm
in-chip Woodpile

%Header:
TiltCorrectionOff
Operationmode 1
Linestartmode 1
timestampOn
ConnectPointsOn
DwellTime 10
PowerScaling 1
Laserpower 80
Pointdistance 200
DefocusFactor 1.0
TiltCorrectionOn
Polylinemode 1
PerfectShapeOn
measuretilt 3
FindInterfaceAt 0.5

%The woodpile has 7 beam layers:
xoffset 0
yoffset 0
zoffset 60
Updaterate 3000
Include 100xlines10.gwl
xoffset 0
yoffset 0
zoffset 50
Updaterate 3000
Include 100ylines10.gwl
write
xoffset 0
yoffset 0
zoffset 40
Updaterate 4000
Include 100xlines10.gwl
xoffset 0
yoffset 0
zoffset 30
Updaterate 4000
Include 100ylines10.gwl
Xoffset 0
yoffset 0
zoffset 20
Updaterate 5000
Include 100xlines10.gwl
xoffset 0
yoffset 0
zoffset 10
Updaterate 5000
Include 100ylines10.gwl
Xoffset 0
yoffset 0
zoffset 0
Updaterate 6000
Include 100xlines10.gwl
```

```
%100xlines10.gwl
%One beam layer consists of 8 beams in x:
addxoffset 0
addyoffset 2
addzoffset 0
Include 100x4line.gwl
addxoffset 0
addyoffset 14
addzoffset 0
Include 100x4line.gwl
addxoffset 0
addyoffset 14
addzoffset 0
Include 100x4line.gwl
addxoffset 0
addyoffset 14
addzoffset 0
Include 100x4line.gwl
addxoffset 0
addyoffset 14
addzoffset 0
Include 100x4line.gwl
addxoffset 0
addyoffset 14
addzoffset 0
Include 100x4line.gwl
addxoffset 0
addyoffset 14
addzoffset 0
Include 100x4line.gwl
addxoffset 0
addyoffset 14
addzoffset 0
Include 100x4line.gwl
```

```
%100ylines10.gwl
%One beam layer consists of 8 beams in y:
addxoffset 6
addyoffset 0
addzoffset 0
Include 4x100line.gwl
addxoffset 14
addyoffset 0
addzoffset 0
Include 4x100line.gwl
addxoffset 14
addyoffset 0
addzoffset 0
Include 4x100line.gwl
addxoffset 14
addyoffset 0
addzoffset 0
Include 4x100line.gwl
addxoffset 14
addyoffset 0
addzoffset 0
Include 4x100line.gwl
addxoffset 14
addyoffset 0
addzoffset 0
Include 4x100line.gwl
addxoffset 14
addyoffset 0
addzoffset 0
Include 4x100line.gwl
addxoffset 14
addyoffset 0
addzoffset 0
Include 4x100line.gwl
```

```
%100xline.gwl
%One beam consists of 9 layers each of 16 lines
Linedistance 250
Linenumber 16
0 0 10
105 0 10
write
0 0 9.1
105 0 9.1
write
0 0 7.8
105 0 7.8
write
0 0 6.5
105 0 6.5
write
0 0 5.2
105 0 5.2
write
0 0 3.9
105 0 3.9
write
0 0 2.6
105 0 2.6
write
0 0 1.3
105 0 1.3
write
0 0 0
105 0 0
write
```

```
%4x100line.gwl
%One beam consists of 9 layers each of 16 lines
Linedistance 250
Linenumber 16
0 0 10
0 105 10
write
0 0 9.1
0 105 9.1
write
0 0 7.8
0 105 7.8
write
0 0 6.5
0 105 6.5
write
 0 0 5.2
0 105 5.2
write
0 0 3.9
0 105 3.9
write
0 0 2.6
0 105 2.6
write
0 0 1.3
0 105 1.3
write
0 0 1
0 105 0
write

```

External communication activities

Peer-reviewed journal papers

In-chip fabrication of free-form 3D constructs for directed cell migration analysis
Mark Holm Olsen, Gertrud Malene Hjortø, Morten Hansen, Özcan Met, Inge Marie Svane, and Niels B. Larsen
Lab on a Chip 2013 – accepted with minor revisions.

Confinement dependent chemotaxis analysis in chip-integrated linear migration constructs
Mark Holm Olsen, Gertrud Malene Hjortø, Morten Hansen, Özcan Met, Inge Marie Svane, and Niels B. Larsen
Manuscript under development.

Conference contributions

Oral presentation
O*n-chip two-photon polymerization of cell-sized 3D microenvironments for chemotaxis analysis*
Niels B. Larsen, Mark Holm Olsen, Gertrud Malene Hjortø, Morten Hansen, Özcan Met and Inge Marie Svane
Abstract from 38th International Conference on Micro and Nano Engineering, Toulouse, France, 2012

Poster
Multiphoton polymerization of immune cell scaffolds
Mark Holm Olsen, Gertrud Malene Hjortø, and Niels B. Larsen
European School On Nanosciences & Nanotechnologies, 2011

Teaching and supervising activities

Assistant teacher, Polymer Microfabrication course, winter 2011, 2012, 2013
Co supervisor for Rasmus Meyer Mortensen, Bachelor project, spring 2013
Co supervisor for Roberta Leah, 10 ECTS special curse, spring 2013

Appendix 2

In-chip fabrication of free-form 3D constructs for directed cell migration analysis

Accepted in Lab on a Chip, September 2013 – with minor revisions

In-chip fabrication of free-form 3D constructs for directed cell migration analysis

Mark Holm Olsen,[a] Gertrud Malene Hjortø,[a] Morten Hansen,[b] Özcan Met,[b] Inge Marie Svane,[b] and Niels B. Larsen[a]

Received (in XXX, XXX) Xth XXXXXXXXX 20XX, Accepted Xth XXXXXXXXX 20XX
DOI: 10.1039/b000000x

Free-form constructs with three-dimensional (3D) microporosity were fabricated by two-photon polymerization inside the closed microchannel of an injection molded commercially available polymer chip for analysis of directed cell migration. Acrylate constructs were produced as woodpile topologies with a range of pore sizes from 5x5 µm to 15x15 µm and prefilled with fibrillar collagen. Dendritic cells seeded into the polymer chip in a concentration gradient of the chemoattractant CCL21 efficiently negotiated the microporous maze structure for pore sizes of 8x8 µm or larger. Cells migrating through smaller pore sizes made significantly more turns than through larger pores. The introduction of additional defined barriers in the microporous structure resulted in dendritic cells making more turns, while still being able to follow the chemoattractant concentration gradient.

Introduction

Mammalian cell migration studies have traditionally been performed on planar culture substrates of glass or plastics, a two-dimensional (2D) environment not very similar to the 3D extracellular matrix environment of the animal body. Numerous publications in the past decades have reported how cell adhesion and migration mechanisms differ in 3D versus 2D microenvironments.[1-3] The strong dependence on 3D confinement is particularly notable for fast moving immune cells as recently demonstrated for neutrophils and T blasts in vitro [4] and for dendritic cells in vivo.[5] Migration analysis studies in 3D have extensively used self-assembling extracellular matrix components,[6] in particular fibrillar collagen, to form random microporous constructs typically located within macroscopic lateral confinements to permit the establishment of a defined concentration gradient directing the cell migration.[7] Approaches to improve the structural homogeneity have included templating of migration constructs on 3D close-packed microbead arrays to engineer more uniform sizes of cavities and connecting pores.[8, 9] Widely used Transwell assays (modified Boyden chambers)[10] capture some of the 3D characteristics by confining cell movement to an unbranched short tunnel of well-defined width and of typical length much shorter than the extended length of the cells being investigated. Thus, Transwell assays are useful improvements over the purely 2D motion on planar substrates, but with obvious analytical shortcomings. First, they cannot mimic the 3D connectivity of real tissue microenvironments in a defined way. Second, individual cells will not experience complete 3D confinement at any time point due to the short tunnel length. Third, cell migration only proceed perpendicular to the porous culture surface which does not allow for studying variations in the migration process, but only an endpoint analysis of the number of migrated cells. Recent reports have overcome some of the Transwell assay shortcomings by using poly(dimethyl siloxane) (PDMS) based soft lithography to produce microchannel arrays of varying dimensions for analysis of immune cell or cancer cell migration.[11-15] These studies have provided important insight on the intracellular mechanisms governing confined migration. However, easily accessible soft lithography methods are experimentally restricted to single or few layer topologies that cannot mimic the complex in vivo environments. We demonstrate how to overcome these limitations in cell migration analysis using two-photon polymerization to write the targeted 3D environments of arbitrary complexity with micrometer scale resolution. The resulting structures are made available for cell biologists in a ready-to-use and cost efficient format by fabricating the cell migration constructs inside a commercially available closed microfluidic chip designed for cell migration analysis.

The ideal construct for migration analysis should (a) result in cell migration behavior that functionally resembles the in vivo behavior as closely as possible, (b) be highly reproducible to enable reliable interpretation of the cell responses, and (c) support the presence of a stable concentration gradient of signaling molecules across the construct to perform directed cell migration (chemotaxis) studies. The natural microenvironment is a highly complex combination of topological, chemical, and mechanical cues that is unlikely to be mimicked exactly in a laboratory setting. As a functional approximation, in vitro microenvironments may be designed with varying degrees of microstructural complexity to explore cellular navigation abilities, possibly after the addition of natural extracellular components to provide biochemical and ultrastructural signaling. Designs inducing the most in vivo like migration can then be selected for larger scale fabrication to be used in cell preparation optimization or cell migration validation. Both applications are of relevance to cell-based immunotherapy by dendritic cells as we target here. Thus, constructs must be fabricated using a method capable of reproducible writing of 3D structures with a resolution of sub-cellular dimensions, preferably in combination with extracellular matrix components. The method should also be of sufficiently low cost per analysis to be used as a routine tool in cell biological work that typically calls for large number of experiments to

achieve adequate statistical significance. The final constructs should permit optical visualization of the migrating cells to analyze their individual detailed migration pathways within a stable concentration gradient maintained for hours to days.

Cell migration through connective tissue is of key interest in several biological areas including immune responses and cancer invasion. The main load bearing part of the extracellular matrix in connective tissue is fibrillar collagen, constituting >90% of the extracellular matrix protein and forming a protein hydrogel with abundant fibrils and fibers of sub-micrometer to micrometers diameters.[16] Consequently, most 3D migration studies have used collagen based systems. Recent reports comparing the in vivo topology of connective tissue in mice to in vitro models showed heterogeneous in vivo environments of microporous pathways (from 1-20 µm in diameter) between dense regions inaccessible to fast migrating immune cells, a heterogeneity only poorly reproduced by in vitro models.[5, 17] Addtionally, fiber and fibril diameters and spacings in in vitro collagen matrices vary a lot within each sample and between samples. Such topological variation prohibits reliable interpretation of possibly significant cell-to-cell differences in migratory properties.

The microstructural shortcomings of natural self-assembled polymers have in recent years been overcome by introducing non-linear optical methods for direct 3D writing. Two-photon processes can induce spatially localized chemical reactions in 3D with sub-micrometer accuracy, either for locally forming or breaking chemical bonds in synthetic or natural polymers. Several groups have employed two-photon microscopy for locally photodegrading cell-loaded collagen gels or cross-linked poly(ethylene glycol) (PEG) gels to produce defined channel networks for cell migration.[18, 19] This elegant solution has the disadvantage of requiring preloading of the cells in the collagen or PEG hydrogel, and thus local access to advanced two-photon microscopy systems. In addition, the loading of cells into the hydrogel material until two-photon induced release may affect their phenotype and their viability.

Two-photon polymerization (2PP) uses a two-photon microscope to locally polymerize the material into arbitrary 3D shapes with sub-micrometer resolution.[20-22] Such constructs are structurally stable and may be produced at dedicated fabrication facilities independently of their final biological use.[23] Recent reports have shown that 2PP can produce cellular sized constructs of low structural complexity for studying directed cell migration in an open custom built microchamber system.[24, 25] Broader use of the technology may be anticipated from increasing the structural complexity, decreasing the minimum feature size, and integrating the constructs in a closed standard chip design.

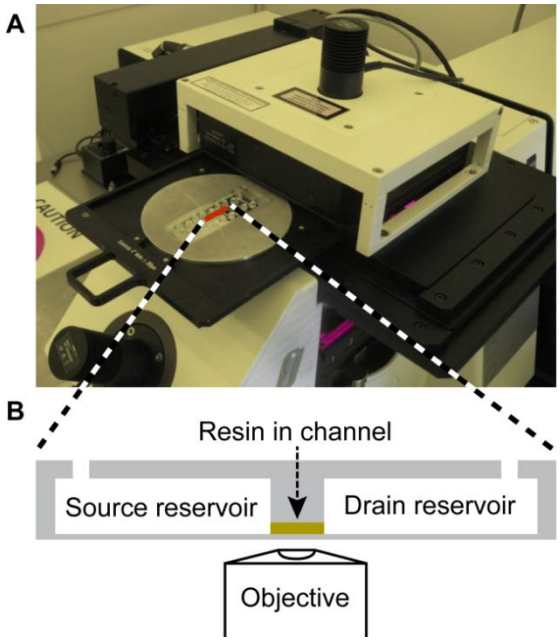

Fig. 1 (A) Two-photon polymerization system with chip mounted in a custom-made aluminum adaptor. (B) Cross section of the chip showing the reservoirs (65 µL) and channel (<1 µL) geometry with the channel loaded with resin (yellow). The thin chip bottom layer is optimized for microscopy with high NA objectives and thus ideal for high resolution 2PP fabrication.

Very recently, the extraordinary ability of 2PP to polymerize and structure 3D objects within a closed microchannel system was reported for use as in-chip filters or as in-chip enzymatic reactors.[26, 27] Here, we demonstrate the fabrication of reproducible 3D structures with cell sized pores by 2PP inside the closed channel of a commercially available disposable polymer microfluidic chip (Fig. 1) designed for chemotaxis analysis in non-structured hydrogel materials. The generated "woodpile" structures are employed to investigate the migration behavior of mature human dendritic cells (DCs) towards a chemoattractant (CCL21) in complex microtopologies of varying defined dimensions. The use of a chip system with integrated reservoir structures next to the targeted microchannel (Fig. 2) has added 2PP benefits of easy and fast pre-exposure loading and post-exposure structure development of the low viscosity acrylate resin. Loading and development is achieved in minutes instead of hours to days as previously reported for procedures including pre-exposure soft baking steps and cumbersome development in long closed channel systems.[26] Writing times of hours limit production volume. However, the in-chip system can be re-used for the biological analysis after a simple and short enzymatic (collagenase) treatment which compensates for the higher price of the serial 2PP fabrication technique. The dedicated chip design supports a stable chemoattractant concentration gradient for up to 48 h,[28] and the thin chip bottom layer is optimized for high magnification microscopy of the migrating cells.

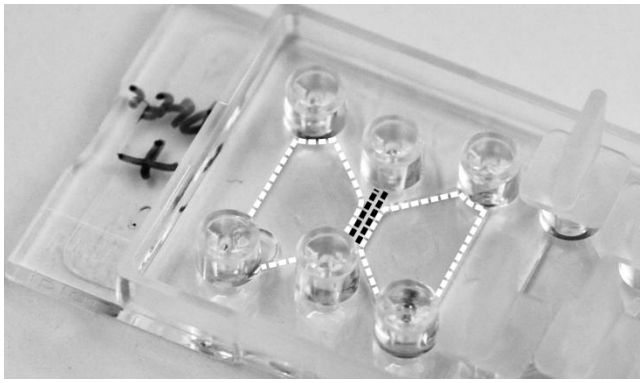

Fig. 2 Photograph of the ibidi µ-Slide Chemotaxis3D chip (76 mm x 25 mm) used as platform for two-photon polymerization of cell-sized 3D microstructures in the center channel (black dashed lines) between chemoattractant-containing and –free reservoirs (white dashed areas).

Materials and Methods

In-chip fabrication of cell migration constructs

Two-photon polymerization was performed on a Nanoscribe Photonic Professional system (Nanoscribe, Eggenstein-Leopoldshafen, Germany). The Nanoscribe system uses a 780 nm Ti-Sapphire laser emitting 150 fs pulses at 100 MHz with a maximum power of 100 mW (20 mW at the sample surface) and is equipped with a 100x, 1.4 NA oil immersion objective. The substrate is placed in a holder that fits into a piezoelectric x/y/z stage. Writing is done by controlling the laser in time and moving the stage in x,y and z. Structures were produced in a liquid acrylate based resin (IP-L 780, Nanoscribe). Writing speeds ranged from 400 µm/s to 1200 µm/s depending on the depth of writing into the resin: Larger writing depths caused loss of light intensity, and the writing speed was reduced to retain complete cross linking and structural rigidity. All structures were written in order from the largest to smallest writing depths to minimize intense scattering of the laser beam from already polymerized structures. Thus, the first layers written are furthest away from the objective and the surface of the substrate. In open systems, this technique requires the initial writing of support pillars and beams in the opposite writing order to prevent polymerized lines of the targeted structure from floating away in the liquid resin. Supports were not required for in-chip writing since the initial structure could be anchored to the channel ceiling.

Initial experiments used circular Ø 30 mm x 0.17 mm glass cover slips as substrates in an open system. Briefly, the cover slips were cleaned with acetone and 2-propanol (both Sigma-Aldrich, St. Louis, MO) before a drop of resin was placed on the top and the substrate was fixed in the holder with 4 drops of Fixogum (Marabu, Tamm, Germany). After exposure the substrates were developed in 2-propanol by submersion in a beaker for 20 min and washed with acetone before drying with compressed air.

The polymer chip (µ-Slide Chemotaxis^{3D}, ibidi, Martinsried, Germany) was mounted on the stage via fixation with Fixogum to a custom made aluminum adaptor (see Fig. 1A). A drop of resin was placed on one channel inlet for the channel to fill by capillary forces. Residual resin on the inlet was removed with tissue. Identical writing parameters were used for the chip and the cover slip substrates. An initial measurement of the channel dimensions was performed by the autofocus system to determine the required structure height to fill the channel. Development was done by filling the reservoirs with 2-propanol and emptying after 10 min. The process was repeated three times. After development, the reservoirs and channels were sterilized by flushing with ethanol in a flow bench, and left to dry for 24 h.

Confocal micrograph stacks were acquired with a Zeiss LSM 5 microscope (Carl Zeiss, Oberkochen, Germany) with either a 63x, 1.4 NA (numerical aperture) oil immersion objective or a 40x, 1.2 NA water immersion objective, using excitation light at 488 nm and collecting emitted light from 515-550 nm. The recorded stacks were processed into 3D reconstructions using ImageJ.[29]

Generation of monocyte-derived dendritic cells

CellGro DC serum-free medium, GM-CSF, IL-4, IL-1β, TNF-α and IL-6 were all obtained from CellGenix (Freiburg, Germany). PGE_2 was obtained from Sigma-Aldrich. Iscoves modified Dulbecco's medium (IMDM), and human AB-Serum was acquired from Lonza (Basal, Switzerland), penicillin / streptomycin (P/S) and Fetal Bovine Serum (FBS) from Invitrogen (Life Technologies, Paisley, UK). $NaHCO_3$ solution (7.5%), 10x MEM solution, and collagenase (Clostridium Histolyticum, cell culture tested) were from Sigma-Aldrich, PureCol (collagen I) solution from Advanced Biomatrix (San Diego, CA) and CCL21 from R&D Systems (Minneapolis, MN).

Leukapheresis was done on healthy blood donors after informed consent followed by separation using elutriation (Terumo BCT, Lakewood, CO) and subsequent freezing of monocytes (80-90% pure as determined by flow cytometry on CD14). Thawed monocytes with a viability >99% were cultured for five days in culture plates (Ø 21 cm) at $5{\cdot}10^5$ cells/ml in CellGro DC medium supplemented with 1000 U/ml GM-CSF and 250 U/ml IL-4 to produce immature DCs. Maturation of DCs was induced for 2 days by adding 1000 U/ml TNF-α, 1000 U/ml IL-1β, 1000 U/mL IL-6, and 1 µg/ml PGE_2.[30] Harvest of DCs was performed by aspiration followed by cold incubation of the remaining cells in PBS with EDTA (5 mM) and subsequent scraping of cells followed by freezing of DCs in aliquots (90% human serum and 10 % DMSO).

Collagen gel and DC loading in chips with constructs

Mature DCs were thawed and transferred to pre-warmed IMDM, 10% FBS, 1% P/S. The DCs were centrifuged at 220g for 5 minutes. Medium with DMSO was removed and the cells were left to acclimatize for 30 minutes at room temperature in fresh medium. The cells were centrifuged and re-suspended at $4{\times}10^6$ cells/ml. A collagen mixture with cells was prepared according to the ibidi manual. Briefly, 10 µl of $NaHCO_3$ (7.5%) was mixed with 20 µl of 10 x MEM solution. After addition and mixing with 150 µl of PureCol

solution, 90 µl of DC suspension was added and the mixture was applied to the chip for polymerization at 37°C for 30 minutes (either 6 µl inside the ibidi channel or 60 µl in the sink reservoir). After collagen polymerization, the sink and source reservoirs were filled with medium alone and medium with added CCL21 (60 nM), respectively. In the cases where the cells were loaded in the sink reservoir, only the source reservoir was filled upon collagen polymerization. The final collagen concentration was 1.67 mg/ml.

Time-lapse microscopy of DC migration

We monitored DC migration using a custom made time lapse setup based on an inverted phase contrast microscope (Zeiss Axiovert 100, Oberkochen, Germany) with a 20x phase contrast objective. The plugged chip with loaded DCs was mounted on a computer controlled translation stage, holding a temperature controlled (37°C) humidified incubation chamber supplied with 5% CO_2 in air. This setup allowed tracking for several days. Analysis of cell migration in the X, Y and Z direction is in principle possible. However, the optical contrast was insufficient for allowing analysis in the Z direction, since the DCs during migration are often very long and slender with dendrite lengths of 100-300 µm and only a few µm in width and consequently a very small cell body. DC migration was tracked for approximately 48 hours. This is the time-span during which the gradient established inside the chip is reported to be stable.[28]

Slight positional variations in the stage position during time-lapse recordings were corrected by use of the TurboStack plugin for ImageJ.[31] The faint outlines of the DC dendrites within the microporous constructs were subsequently enhanced by subtracting the average (static) image of the construct from all images in the time-lapse sequence, and adding the subtracted images into the green channel of the recorded phase contrast images. Thus, the non-static cells will appear with a green tint in the final image sequences. Movies are provided of both the unprocessed and image processed time lapse sequences.

Collagenase treatment of construct

After experimentation, the IPL woodpile structures were collagenase treated for removal of collagen and cells: collagenase solution (0.5 mg/ml in PBS) was added to the reservoirs and the channel inlets of the chip. The chip was incubated for 1 hour at 37°C, the collagenase solution was withdrawn from the reservoirs, and the chip reservoirs were washed with water and then ethanol. Before reuse, the chip reservoirs were washed once more in sterile water, and the reservoirs and structures were completely emptied by applying suction to the channel after plugging the reservoir inlets.

Results and discussion

Writing optimization using free-standing constructs

Woodpile structures were chosen as the starting point for designing and investigating directed cell migration in 3D, since they provide the cells with multiple straight pathways at perpendicular orientations in close vertical proximity (Fig. 3). Writing time is a key limitation in 2PP fabrication. Thus, the material volume fraction in the woodpile design should be minimized to reduce writing time while still maintaining structural integrity of the construct. We tested a range of beam cross-sections and found optimum rectangular beam height-to-width ratios of 5:2 for 5x5 µm to 10x10 µm pore sizes and 3:1 for 15x15 µm pore sizes, respectively. Additionally, overlying layers of beams were written with a vertical overlap of one writing layer (1.3 µm) to enhance the mechanical stability. The 2PP-induced polymerization resulted in a change in refractive index from the unpolymerized resin. The associated light scattering through structured construct parts prevented accurate and fast writing at greater writing depths. Consequently, writing of the structured construct volumes had to proceed from the largest writing depths (hereafter termed "top" with reference to the channel structure configuration) towards the smallest writing depths (termed "bottom").

The woodpile writing process was optimized in an open system prior to in-chip fabrication due to easier access for structural characterization by confocal optical microscopy and electron microscopy. All constructs had outer dimensions of W x L x H = 100 µm x 100 µm x 70 µm produced on glass cover slips as substrates. Polymerization of a free-floating polymer wire in liquid resin was problematic since convective flow resulted in the wire floating away before its neighboring wire could be written. Thus, at least the endpoints of all polymerized wires must be anchored to a solid material. The fabrication of free standing constructs using the top-to-bottom approach called for the introduction of support pillars and beams as anchoring objects, as shown in Fig. 3 with and without the supports. The support pillars were fabricated bottom-to-top to ensure anchoring to the cover slip surface before initiating polymerization of the targeted woodpile construct. A substantial power loss was observed at larger writing depths which could be compensated by reducing the writing speed from 1200 µm/s at the bottommost layer to 400 µm/s at the topmost layer (70 µm writing depth). The spatial separation of neighboring written wires directly affects the writing time. Center-to-center spacings of 250 nm and 1300 nm in the lateral and vertical dimensions, respectively, were found to minimize writing time while maintaining structural integrity.

The use of a lower magnification objective will increase the voxel volume (formally the two-photon point spread function) and might lead to higher volumetric writing speeds ($\mu m^3/s$). However, the larger voxel volume also reduces the photon density resulting in a strong decrease in two-photon initiated processes. We explored this experimentally using either a 100x/1.4 NA or a 20x/0.5 NA objective and found the required reduction in writing speed at lower magnification to result in largely equal volumetric writing speeds using either objective. The lower magnification objective with a lower numerical aperture will have a substantially elongated voxel in the axial direction leading to poorer vertical resolution.[20, 32] Consequently, a 100x/1.4 NA objective was used for the fabrication of all free-standing and

in-chip constructs.

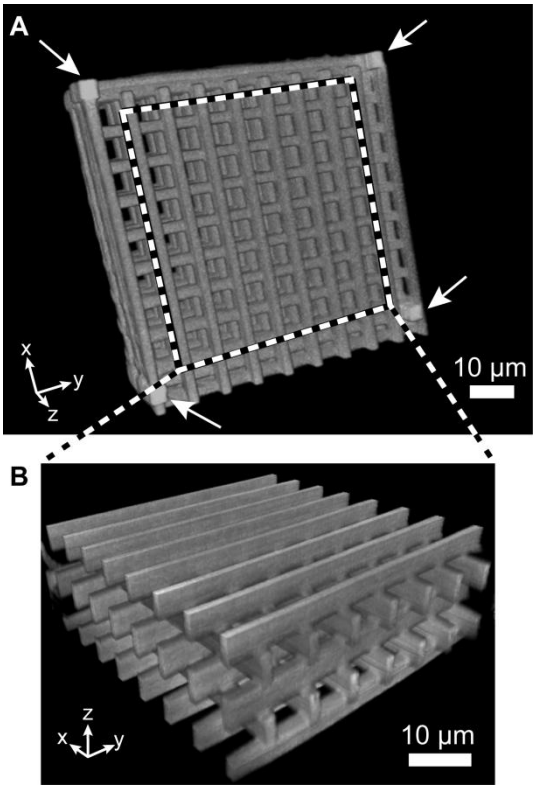

Fig. 3 Confocal fluorescence microscopy of a freestanding autoflourescent woodpile structure on a glass cover slip with pore sizes of 8 x 8 µm in the x, y and z directions. (A) 3D reconstruction of the woodpile construct, confirming a porous 3D structure. Support pillars and beams were added at the corners and around the edges of the structure (pillars marked by white arrows). (B) Reconstruction of the center volume outlined in A.

In-chip cell migration constructs

Most microfluidic chips designed for in-channel high resolution optical microscopy can be used as substrates for in-chip 2PP fabrication. The thin bottom layer and the two reservoirs situated next to the channel in the ibidi chip is a particular favorable design (see Fig. 1). The two reservoirs with a total volume of 130 µL in close proximity to a total channel volume of ≈1 µL facilitate fast diffusion based development due to a very short diffusion distance of only 0.5 mm. Development times are further reduced by pressure-driven and thermal convection effects during filling and emptying of the reservoirs. In terms of material economics, the closed microchannel system uses very small volumes (few µL) of costly resins and optional biomolecular additives compared to open systems. For chemotaxis analysis, the closed chip system can sustain a controlled linear concentration gradient in solution for up to 48h [28] with a better control of the observed gradient than in previously reported open systems written by 2PP.[24, 25]

The chemoattractant concentration gradient is established in the middle channel section of dimensions W x L x H = 1 mm x 2 mm x 70 µm. Microstructured constructs of that size would take several days to produce using the available combination of resin and 2PP system. We chose to reduce the writing time by fabricating a construct of smaller outer dimensions (W x L x H = 100 µm x 300 µm x 70 µm) in the middle of the channel. The minimum construct dimensions were given by three requirements: (a) A substantial number of cells should traverse the porous construct instead of migrating around the construct (minimum length); (b) No cells should be able to sense both ends of the construct with their dendrites simultaneously (minimum width); (c) Cells should not be able to migrate above or below the construct (full channel height). The biological relevance of migration analysis constructs with widths on the 100 µm length scale is supported by a recent publication showing oriented motion of murine dendritic cells only within the nearest 100-150 µm of chemokine-secreting lymphatic vessels.[33] Ideally, all cells should be forced to migrate through the construct. We tried to achieve this by a "mix-and-match" combination of 2PP fabrication of the 3D microstructured construct followed by conventional 2D patterned exposure through a shadow mask in a mask aligner to polymerize bulk barriers leading up to the construct. The process and the resulting in-chip structures are presented in the Electronic Supplementary Information (ESI) Fig. S1. The fabrication procedure was successful but the bulk structures resulted in substantial cytotoxicity that prevented reliable migration studies. We did not further explore the use of bulk barriers since the cell analysis could be performed with statistical significance on the fraction of cells migrating through the construct in the absence of bulk barriers.

Complete development of in-channel woodpile constructs was verified by fluorescence microscopy. A CO_2 laser (FH Flyer, Synrad, Mukilteo, WA) was employed for sectioning a chip next to the woodpile construct to provide optical access. The chip had already been used for cell migration analysis followed by regeneration (collagen degradation) by collagenase treatment. Fig. 4 shows fluorescence micrographs of an in-channel woodpile construct in side view and in bottom view, and confirms the presence of a continuous porous structure from channel top to bottom.

Cytotoxicity is a well-known issue of photopolymerized materials. We compared the metabolic activity of dendritic cells cultured on polymerized slabs of IP-L resin to polymerized slabs of a widely used poly(ethylene glycol) diacrylate resin.[34] Both materials induced similar slightly reduced metabolic activity compared to a reference cell culture surface of tissue culture grade polystyrene (TCPS) (ESI Fig. S2). The cytotoxicity of the in-chip written IP-L constructs was not evaluated directly. However, the efficient washing process via the chip reservoirs is expected to remove unreacted macromers and photoinitiators to a similar extent as found for the IP-L slabs. Cell functional assays supported this assumption by showing indistinguishable migration behavior of DCs loaded in channels with or without a fabricated IP-L construct.

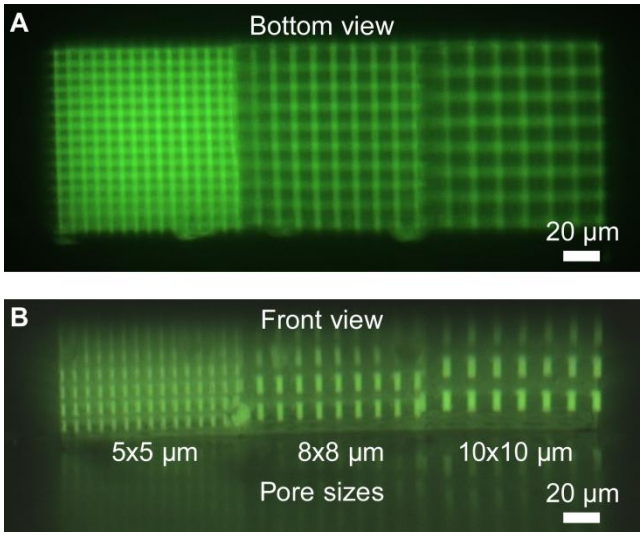

Fig. 4 Fluorescence micrograph of a woodpile construct in an ibidi channel shown in (A) top view and (B) side view after cell analysis and regeneration with collagenase. Each construct consists of three 100 x 100 x 70 μm^3 volumes with 5x5 µm, 8x8 µm, and 10x10 µm pore sizes respectively. A reflection in the channel bottom is seen in the side view image. The construct microstructure is found to sustain multiple cell loading, cell analysis, and regeneration cycles without observable degradation.

Directed in-chip cell migration

The IP-L woodpile constructs were tested for their ability to allow directed DC transmigration in a concentration gradient of the chemokine CCL21 in the construct, hereafter termed "front-to-back" migration. We designed woodpile constructs with square pore sizes of 5x5 µm, 8x8 µm, 10x10 µm, and 15x15 µm to evaluate the ability of the DCs to migrate or squeeze through cell-sized passage ways (Fig. 3 and Fig. 4). Collagen was introduced into the construct pores to provide a biological environment supporting migration, while still permitting formation of the chemokine gradient, as demonstrated in former chemotaxis studies using similar minimal channel cross-sections (3 µm x 10 µm versus 5 µm x 5 µm in this work).[11] Migration through the 5x5 µm pores was rarely seen and thus not included in the statistical analysis of the migration pathways. The inability of DCs to pass 5x5 µm pores despite the presence of a chemokine gradient is interesting, since we have recently successfully used conventional Transwell migration assays with circular pore diameters of 5 µm to study other aspects of DC migration potential.[35] The main topological difference is the much smaller thickness (width) of the 10 µm thick Transwell membrane that allows DC dendrites of lengths >50 µm to explore the highest and lowest chemokine concentrations simultaneously, effectively presenting a very steep concentration gradient. In this aspect, our 100 µm wide constructs with a definable gradient slope likely resemble the in vivo microenvironment of the DCs more closely.[33]

In the further migration experiments we only used woodpile constructs with pore sizes of 8x8, 10x10, and 15x15 µm, respectively. DC migration was analyzed by manual inspection of time-lapse image sequences to determine the number of lateral turns (in bottom view) performed by each cell inside woodpile structures of different pore sizes. A lateral turn requires concomitant vertical translocation due to the woodpile topology, thereby revealing full 3D cell motion. Directed cell migration analysis requires a stable CCL21 concentration gradient that is established by diffusion in the full channel width within hours, and cells need to migrate in from the sink reservoir where they are seeded. Consequently, the tracking of cells was only started once significant migration was observed within the channel region (typically within 4 hours). The introduction of a microporous construct might delay gradient formation within the construct. As discussed in the ESI, the microscopic pore dimensions, the large porosity of the woodpile topology (>0.68), and the high constrictivity factor (estimated to be 0.9) [36] gives a reduction in the effective CCL21 diffusion constant by <2. Thus, the additional time involved in establishing a stable gradient within the 100 µm wide construct will be insignificant compared to the time for forming the full gradient across the 1 mm wide channel.

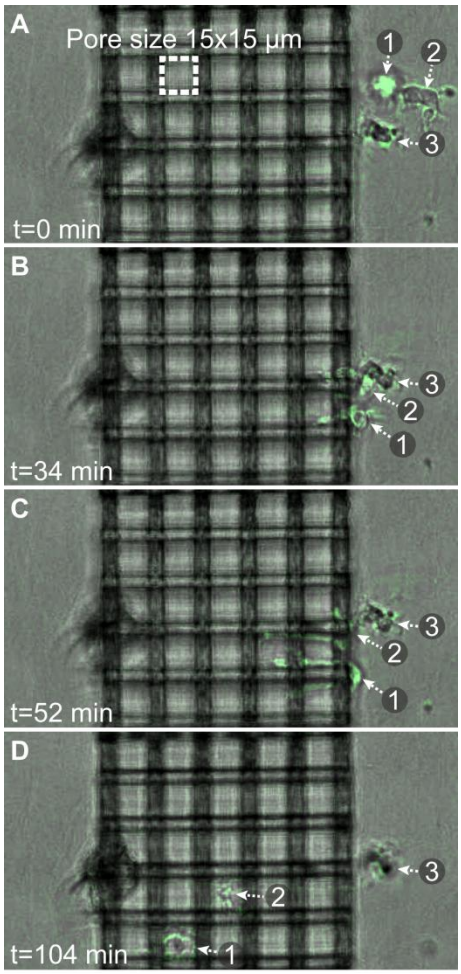

Fig. 5 Phase contrast microscopy snapshots (bottom view) showing two dendritic cells (labeled "1" and "2") migrating inside a 15 x 15 µm pore size woodpile construct. Both cells probe neighboring channels in (B) and (C), before deciding on a channel to migrate through in (D). The cell outlines have been highlighted by use of image processing in ImageJ.

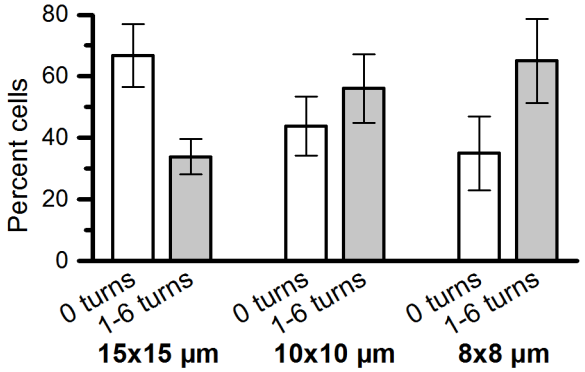

Fig. 6 Comparison of the fraction of cells moving straight through a woodpile construct to cells taking 1 or more turns, as a function of the construct pore size. Significantly more cells turn as they migrate through 8x8 µm pore constructs than through 15x15 µm pore constructs (p=0.033). Error bars show the standard error of the mean (n≥7).

In general the DCs continue their migration path after entering the construct and do not seem to have problems detecting the concentration gradient within the construct. Fig. 5 shows microscopy snapshots at different time points of two DCs crossing a 15x15 µm pore-size woodpile structure. Both cells initially probe two neighboring channel structures with their dendrites before deciding to traverse one of the channels without performing any turns inside the construct. Equivalent behavior has been observed for neutrophils encountering bifurcations in a straight microchannel system.[37] Movies of the time-lapse series are available in image processed and unprocessed versions (ESI Movies 1 and 2). Fig. 6 summarizes the observed difference in migration behavior. Cells migrating through the smaller pore dimensions (8x8 and 10x10 µm) have a significantly higher probability of making at least one turn than cells migrating through the largest pores (15x15 µm). In the latter geometry, the majority of the DCs moves straight through the porous construct, while most cells make at least one turn on their passage of the smallest pore size structures. ESI Fig. S3 shows a detailed analysis of the number of turns made (0, 1-2, 3-4, or 5-6 turns, respectively) as a function of pore size, with a clear trend towards more turns occurring in smaller pores. The results indicate that the cells are more prone to seek alternative paths when confined to smaller cross-sectional areas in a tighter woodpile.

The free-form 2PP process allows for the introduction of barriers to cell migration at arbitrary locations. We explored this design freedom to measure the ability of DCs to navigate in 3D maze structures. The basic woodpile topology permits direct cell migration from the front to the back of the construct, as was most commonly observed for the 15x15 µm pores (Fig. 6). If the cell wants to turn it will need to change its vertical level beforehand to reach a channel in the perpendicular orientation. By blocking the straight front-to-back channels by one additional photopolymerized barrier per channel at alternating positions in neighboring channels, we force all migrating cells to perform at least two half spiral turns in 3D. Fig. 7A shows a computer rendition of the targeted structure in perspective and in side view. The basic woodpile structure is shown in gray while the additional barriers present in all three layers with front-to-back pathways are shown in dark green. The side view shows the barrier-free passage ways for cells in the three layers with sideway channels. The outer dimensions of the construct are increased to W x L x H = 200 µm x 400 µm x 70 µm to provide longer and more detailed analysis of the migration path of the individual cells. The detailed DC migration analysis through the basic woodpile structure indicated a higher fraction of cells making multiple turns through the 10x10 µm porous construct than either 15x15 µm or 8x8 µm pores (ESI Fig. S3). Consequently, we selected the 10x10 pore size for the higher complexity construct. Fig. 7B shows a confocal fluorescence micrograph of one of the layers containing extra barriers in the final in-chip produced construct. Cross-sectional views through one set of the additional barriers show blockage of every second front-to-back channel, while cross-section through the other set of barriers would show blockage of the remaining front-to-back channels.

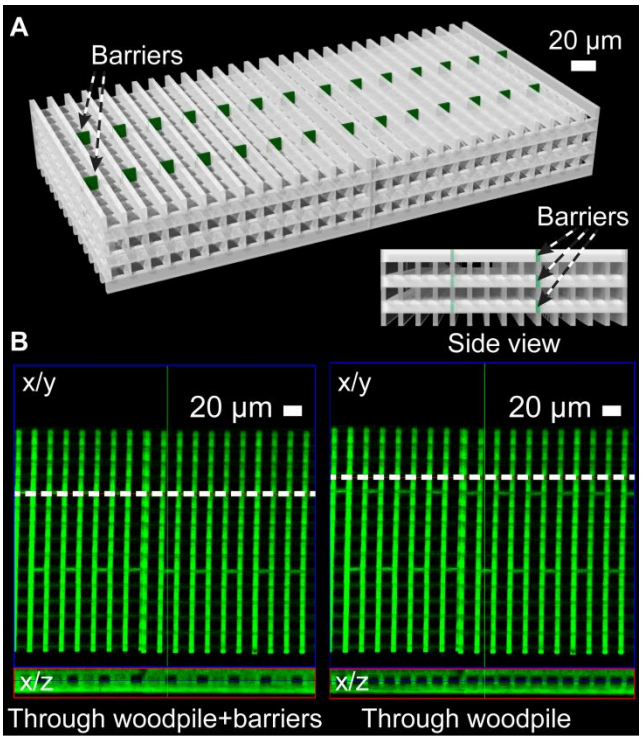

Fig. 7 Higher complexity 3D cell migration construct. (A) Schematic of the construct highlighting in green the additional barriers introduced to obstruct cell migration straight through the construct (from front to back). Insert: Construct in side view showing the free passage ways in the perpendicular direction. (B) Confocal fluorescence micrograph of the construct fabricated by 2PP, focusing on the lower three layers. Left: Orthogonal slice through the barriers (along dashed line in x/y projection) showing blockage of every second front-to-back channel in the x/z projection. Right: Slice through the basic woodpile showing all channels being open at these locations.

DCs were seeded next to the complex constructs using the same procedure as for basic woodpile constructs. The

resulting time lapse sequences are available in image processed and unprocessed formats as ESI Movies 3 and 4, respectively. In general, DCs efficiently found their way through the construct, showing their detection of the chemotactic concentration gradient even in a more complex topology calling for intermittent migration perpendicular to the concentration gradient. Fig. 8 compares the results from the manual cell tracking in 10x10 µm pore woodpiles with or without additional barrier structures. The comparison shows a clear trend for DCs to take many more turns in constructs with additional barriers, also beyond the minimum 2 turns required to traverse the construct from front to back. We observed multiple possible pathways being probed by both DCs in Fig. 5 with very long straight dendrites (up to 70 µm in length, see ESI Movies 1 and 2) being extended into the construct channels prior to deciding on a channel for transmigration. The presence of additional barriers prevents straight extension of probing dendrites, and may thus result in less persistent cell motion either due to differences in signal processing or due to the need for repeated cytoskeletal rearrangements. This is most likely also the case in the less organized in vivo extracellular microenvironment.

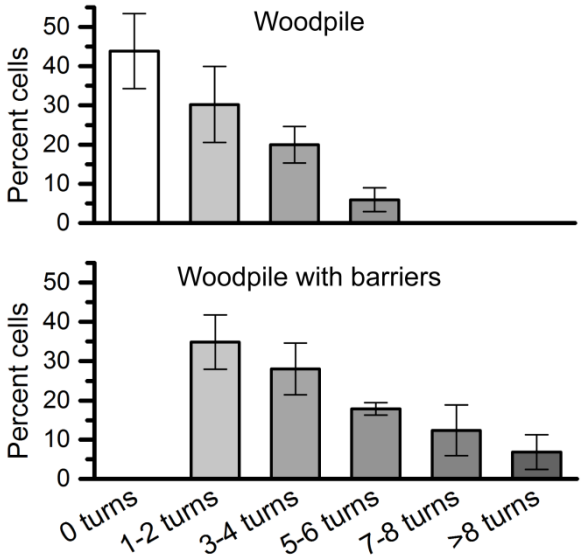

Fig. 8 Fraction of DCs making specific numbers of turns inside an in-chip woodpile construct with 10x10 µm pores without (top) or with (bottom) additional barriers as shown in Fig. 7. Note that cells by design of the construct must make at least two turns to pass the barriers. Error bars show the standard error of the mean (n=3).

Recent work explored the correlation of average pore sizes in random 3D collagen gel networks to the resulting chemotaxis speeds of different cell types ranging from small neutrophils over intermediate sized T blasts to large cancer cells.[4] The fibrillar collagen gel pore size was varied via the concentration and type of collagen used to reflect the variability of fiber widths and interfibrillar spacing observed in connective tissue in vivo.[17] The authors observed a strong correlation between average pore size and migration speed for all three cell types correlating to the size and deformability of their respective nuclei. However, the measured pore sizes spanned more than a factor of 3 for the less dense networks (average pore size >15 μm^2), which likely contributed to the broad range of measured cell migration speeds. In a complementary approach, the motion of dendritic cells was accurately confined within straight PDMS microchannels at a substrate surface, thus bordering 2D and 3D migration.[14] The latter study provided a highly reproducible porous environment for cell migration at the cost of a highly simplified model of a connected 3D pore network of spatially varying complexity. The synthetic in-chip fabricated 3D constructs presented here ideally capture the best of both analytical approaches by providing accurate structural definition and allowing for arbitrary variation in 3D connectivity, with or without the added ultrastructure of fibrillar collagen. We observed dendritic cell migration speeds of 5-6 µm/min in unbranched straight microchannels filled with fibrillar collagen (data not shown) in good agreement with the former work using protein coated but unfilled channels.[14] However, the effective migration speed was significantly reduced upon introduction of branching or barriers in the channel systems due to repeated directional decision processes by the cell when encountering an obstacle parallel (woodpile wall at the construct entrance) or perpendicular (barrier) to its direction of motion. This is in agreement with in vivo migration studies showing slower migration speeds of approx. 2 µm/min of dendritic cells migrating towards towards lymph nodes.[38]

Chip regeneration compensates for higher fabrication costs

Two-photon polymerization is a serial and time-consuming fabrication process which is not well suited for affordable single-use systems. Thanks to the easy liquid exchange and sink/source design of the ibidi chip system the collagenase treatment introduced here thoroughly rinses the chip of collagen residues and prepares the construct for repeated experiments. The effect of the collagenase treatment is observed in Fig. 4 where there is no sign of collagen left on the construct after multiple experiments. The hard IP-L resin creates a tough structure where the pores are still intact and the structural integrity of the construct is not compromised by the treatment. The collagenase regeneration not only drastically reduces the cost of multiple experiments for this system but also for many others that utilize collagen in confined spaces. The only requirement is easy liquid exchange in the system.

Conclusions

In-chip two-photon polymerization of 3D microporous constructs combines the best of two chip fabrication approaches: (1) Fast low-definition 2D macroscopic scale production of channel structures compatible with conventional optical analysis and standardized connectors interfacing to the surroundings; (2) Slower high-definition 3D fabrication of small volume application-specific components. Direct in-chip fabrication obviates the need for subsequent chip bonding processes that often requires extensive optimization to avoid leakage and may easily damage fragile micro- or nanostructures present at the chip surfaces to be

bonded. The 2PP process provides accurate control of both the pore size and the topology experienced by the migrating cells in a material that does not appear to affect their migratory behavior. The source/drain design of the ibidi chip gives complete control of the concentration and thus the steepness of the chemokine gradient. Combining these aspects with easy visualization and cell tracking through the thin bottom adds up to a very versatile and easy to use migration analysis system. The collagenase regeneration procedure strongly reduces the cost per experiment and thus compensates for the higher expense of 2PP fabrication. We foresee that our in-chip designed constructs can be employed both for optimizing cell processing conditions to maximize in vivo chemotaxis of DCs [35] and for validating the migratory potential of each patient's cells in immunotherapy.

Acknowledgement

We acknowledge financial support from the Danish Council for Independent Research, Technology and Production Sciences, grant# 09-070021.

Notes and references

[a] *Department of Micro- and Nanotechnology, DTU Nanotech, Technical University of Denmark, Ørsteds Plads 345E, DK-2800 Kgs. Lyngby, Denmark. Fax: +45 4588 7762; Tel: +45 4525 8161; E-mail: niels.b.larsen@nanotech.dtu.dk*
[b] *Center for Cancer Immune Therapy (CCIT), Department of Hematology, 54P4, Copenhagen University Hospital, Herlev, Denmark*

† Electronic Supplementary Information (ESI) available: Fabrication of solid barriers; cytotoxicity analysis of photopolymers; detailed cell migration analysis; calculated diffusion through microporous constructs; time-lapse movies of migrating dendritic cells. See DOI: 10.1039/b000000x/

1 E. Cukierman, R. Pankov, D. Stevens and K. Yamada, *Science*, 2001, **294**, 1708-1712.
2 P. Friedl and B. Weigelin, *Nat. Immunol.*, 2008, **9**, 960-969.
3 T. Laemmermann and M. Sixt, *Curr. Opin. Cell Biol.*, 2009, **21**, 636-644.
4 K. Wolf, M. Te Lindert, M. Krause, S. Alexander, J. Te Riet, A. L. Willis, R. M. Hoffman, C. G. Figdor, S. J. Weiss and P. Friedl, *J. Cell Biol.*, 2013, **201**, 1069-1084.
5 T. Laemmermann, B. L. Bader, S. J. Monkley, T. Worbs, R. Wedlich-Soeldner, K. Hirsch, M. Keller, R. Foerster, D. R. Critchley, R. Faessler and M. Sixt, *Nature*, 2008, **453**, 51-55.
6 H. Kim and S. R. Peyton, *Integr. Biol. (Camb)*, 2012, **4**, 37-52.
7 V. V. Abhyankar, M. W. Toepke, C. L. Cortesio, M. A. Lokuta, A. Huttenlocher and D. J. Beebe, *Lab. Chip*, 2008, **8**, 1507-1515.
8 A. N. Stachowiak and D. J. Irvine, *J. Biomed. Mater. Res. A.*, 2008, **85A**, 815-828.
9 S. R. Peyton, Z. I. Kalcioglu, J. C. Cohen, A. P. Runkle, K. J. Van Vliet, D. A. Lauffenburger and L. G. Griffith, *Biotechnol. Bioeng.*, 2011, **108**, 1181-1193.
10 C. Decaestecker, O. Debeir, P. Van Ham and R. Kiss, *Med. Res. Rev.*, 2007, **27**, 149-176.
11 D. Irimia, G. Charras, N. Agrawal, T. Mitchison and M. Toner, *Lab. Chip*, 2007, **7**, 1783-1790.
12 D. Irimia and M. Toner, *Integr. Biol. (Camb)*, 2009, **1**, 506-512.
13 J. Jacobelli, R. S. Friedman, M. A. Conti, A. Lennon-Dumenil, M. Piel, C. M. Sorensen, R. S. Adelstein and M. F. Krummel, *Nat. Immunol.*, 2010, **11**, 953-U110.
14 G. Faure-Andre, P. Vargas, M. Yuseff, M. Heuze, J. Diaz, D. Lankar, V. Steri, J. Manry, S. Hugues, F. Vascotto, J. Boulanger, G. Raposo, M. Bono, M. Rosemblatt, M. Piel and A. Lennon-Dumenil, *Science*, 2008, **322**, 1705-1710.
15 Z. Tong, E. M. Balzer, M. R. Dallas, W. Hung, K. J. Stebe and K. Konstantopoulos, *Plos One*, 2012, **7**, e29211.
16 M. van der Rest and R. Garrone, *FASEB J.*, 1991, **5**, 2814-2823.
17 K. Wolf, S. Alexander, V. Schacht, L. M. Coussens, U. H. von Andrian, J. van Rheenen, E. Deryugina and P. Friedl, *Semin. Cell Dev. Biol.*, 2009, **20**, 931-941.
18 O. Sarig-Nadir, N. Livnat, R. Zajdman, S. Shoham and D. Seliktar, *Biophys. J.*, 2009, **96**, 4743-4752.
19 M. W. Tibbitt, A. M. Kloxin, K. U. Dyamenahalli and K. S. Anseth, *Soft Matter*, 2010, **6**, 5100-5108.
20 S. Maruo, O. Nakamura and S. Kawata, *Opt. Lett.*, 1997, **22**, 132-134.
21 J. Serbin, A. Egbert, A. Ostendorf, B. Chichkov, R. Houbertz, G. Domann, J. Schulz, C. Cronauer, L. Frohlich and M. Popall, *Opt. Lett.*, 2003, **28**, 301-303.
22 C. N. LaFratta, J. T. Fourkas, T. Baldacchini and R. A. Farrer, *Angew. Chem., Int. Ed.*, 2007, **46**, 6238-6258.
23 A. M. Greiner, B. Richter and M. Bastmeyer, *Macromol. Biosci.*, 2012, **12**, 1301-1314.
24 P. Tayalia, C. R. Mendonca, T. Baldacchini, D. J. Mooney and E. Mazur, *Adv. Mater.*, 2008, **20**, 4494-4498.
25 P. Tayalia, E. Mazur and D. J. Mooney, *Biomaterials*, 2011, **32**, 2634-2641.
26 L. Amato, Y. Gu, N. Bellini, S. M. Eaton, G. Cerullo and R. Osellame, *Lab. Chip*, 2012, **12**, 1135-1142.
27 M. Iosin, T. Scheul, C. Nizak, O. Stephan, S. Astilean and P. Baldeck, *Microfluid. Nanofluid.*, 2011, **10**, 685-690.
28 ibidi GmbH, http://ibidi.com/applications/chemotaxis/gradient-stability/, 2013.
29 W. S. Rasband, *ImageJ, U.S. National Institutes of Health, Bethesda, Maryland, USA*, http://imagej.nih.gov/ij/, 1997-2012.
30 H. Jonuleit, U. Kühn, G. Müller, K. Steinbrink, L. Paragnik, E. Schmitt, J. Knop and A. H. Enk, *Eur. J. Immunol.*, 1997, **27**, 3135-3142.
31 P. Thevenaz, U. E. Ruttimann and M. Unser, *IEEE Trans. Image Process.*, 1998, **7**, 27-41.
32 W. Zipfel, R. Williams and W. Webb, *Nat. Biotechnol.*, 2003, **21**, 1368-1376.
33 M. Weber, R. Hauschild, J. Schwarz, C. Moussion, I. de Vries, D. F. Legler, S. A. Luther, T. Bollenbach and M. Sixt, *Science*, 2013, **339**, 328-332.
34 C. Williams, A. Malik, T. Kim, P. Manson and J. Elisseeff, *Biomaterials*, 2005, **26**, 1211-1218.
35 M. Hansen, G. M. Hjorto, M. Donia, O. Met, N. B. Larsen, M. H. Andersen, P. thor Straten and I. M. Svane, *Vaccine*, 2013, **31**, 639-646.
36 J. van Brakel and P. M. Heertjes, *Int. J. Heat Mass Transfer*, 1974, **17**, 1093-1103.
37 V. Ambravaneswaran, I. Y. Wong, A. J. Aranyosi, M. Toner and D. Irimia, *Integr. Biol. (Camb)*, 2010, **2**, 639-647.
38 M. Weber, R. Hauschild, J. Schwarz, C. Moussion, I. de Vries, D. F. Legler, S. A. Luther, T. Bollenbach and M. Sixt, *Science*, 2013, **339**, 328-332.

Electronic Supplementary Information for

In chip fabrication of free-form 3D constructs for directed cell migration analysis

Mark Holm Olsen, Gertrud Malene Hjortø, Morten Hansen, Özcan Met, Inge Marie Svane, and Niels B. Larsen

Mix-and-match in-chip fabrication of bulk barriers

Bulk barriers blocking the majority of the chip microchannel were fabricated to prevent cells from migrating around the in-chip produced microporous construct. In brief, the in-chip construct was exposed as described in the Materials and Methods section but without development of the structure, i.e. unexposed IP-L 780 resin remained in the chip channel. The bulk barriers were designed as open areas in a standard photolithography chrome-on-glass shadow mask. The resin-loaded chip was mounted in a Suss MA4 mask aligner (Süss Microtec, Garching, Germany) where the bulk barrier outlines on the shadow mask were aligned to the visible polymerized construct in the resin. The bulk barrier areas were exposed with a dose of 300 mJ/cm^2 at 365 nm, followed by simultaneous development of both construct and bulk barriers according to the procedure described in the Materials and Methods section. Fig. S1 shows that the bulk barriers effectively blocked the channel volume next to the construct and forced the cells to migrate through the construct. Unfortunately, cells showed very limited or aberrant migration behavior that was interpreted as being caused by released of cytotoxic compounds from the bulk barriers. We did not further explore the use of bulk barriers since the cell analysis could be performed with statistical significance on the fraction of cells migrating through the construct in the absence of bulk barriers.

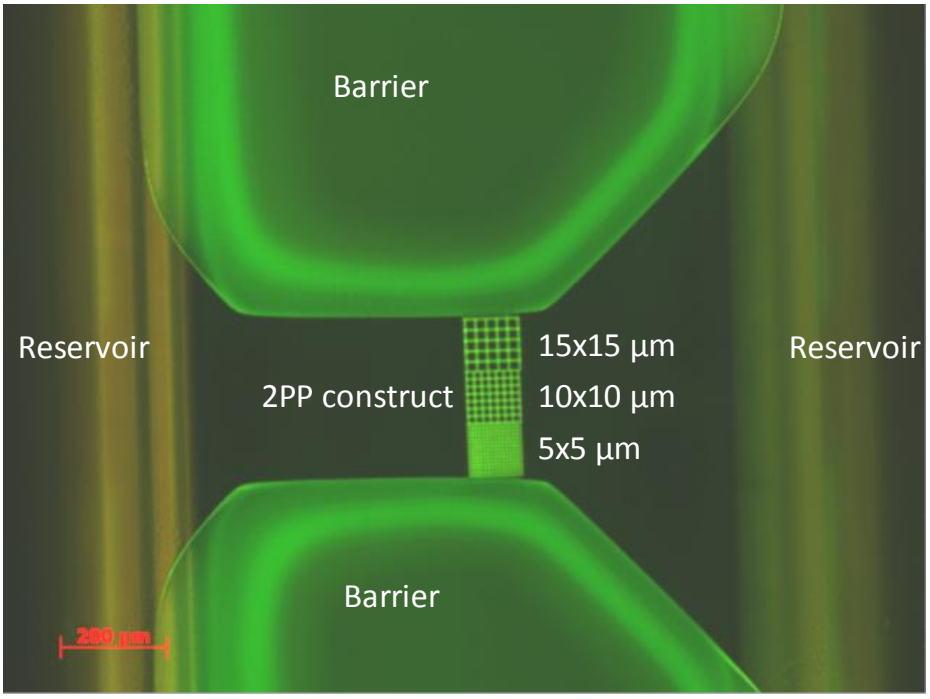

Fig. S1 Fluorescence micrograph of 2PP-written woodpile constructs with pore sizes of 5x5, 10x10 and 15x15 µm inside the microchannel with bulk barriers blocking the remaining channel. The cells were thus forced to enter the construct in order to migrate from one reservoir to the other.

Cytotoxicity test of polymerized IP-L 780 resin

Cytotoxicity of polymerized IP-L 780 resin was evaluated using a dendritic cell (DC) metabolism assay. Cytotoxic comparison was made against Tissue Culture grade polystyrene (TCPS) as a non-toxic reference and photopolymerized poly(ethylene glycol) diacrylate (PEGDA) that is often used in biomedical applications of two-photon polymerization. Experiments were performed in a 96 well TCPS microtiter plate (Nunclon grade, Nunc, Roskilde, Denmark). 50 µL IP-L 780 was dispensed into a well and photopolymerized with a dose of 180 mJ/cm^2 at 365 mW in an MA4 mask aligner (Suss Microtec). 50 µL of 1 kDa PEGDA (Laysan Bio, Arab, AL) with 0.1% w/v IrgaCure 2959 (2-Hydroxy-4′-(2-hydroxyethoxy)-2-methylpropiophenone, Sigma-Aldrich) was dispensed into a second well and photopolymerized with 8.6 J/cm^2. The latter high exposure dose was required due to the presence of ambient oxygen acting as radical quencher. A third untreated well was used as the non-toxic TCPS reference. Samples were prepared in triplicate on each plate.

All wells were washed 3 times with MilliQ grade water (Merck Millipore, Billerica, MA) water and left with MilliQ water for a further 72 h at room temperature. Culture medium consisted of IMDM with 10% FBS and 1% P/S. The wells were filled with culture medium for 15 min and emptied, prior to seeding 5000 – 10000 DCs in 100 µl culture medium in each well and incubation for 24 h. 10 µl AlamarBlue (Life Technologies) was added to each well and incubation was continued for 2 h. After incubation 100 µl supernatant was transferred to a new microtiter plate, and the developed color was measured in a Victor3 plate reader (Perkin Elmer, Waltham, MA). The TCPS well bottom was chosen as reference material for the DC metabolic activity on the two photopolymerized materials. **Fig. S2** shows that photopolymerized IP-L 780 induces some reduction in DC metabolism compared to TCPS, but a smaller reduction than observed on the commonly used PEGDA/IrgaCure 2959 system. These results were obtained on 1.5 mm thick material layers coating the entire well bottom. Considering the extremely small volumes photopolymerized in the in-chip constructs, we do not anticipate significant cytotoxic effects.

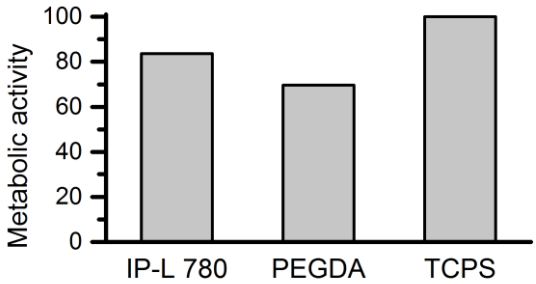

Fig. S2 Metabolic activity of dendritic cells cultured on different materials. Tests are performed with an AlamarBlue assay and the graph shows the activity relative to the metabolic activity on TCPS. Values are the average of 2 independent experiments.

Detailed analysis of the cell migration pathways through woodpile constructs

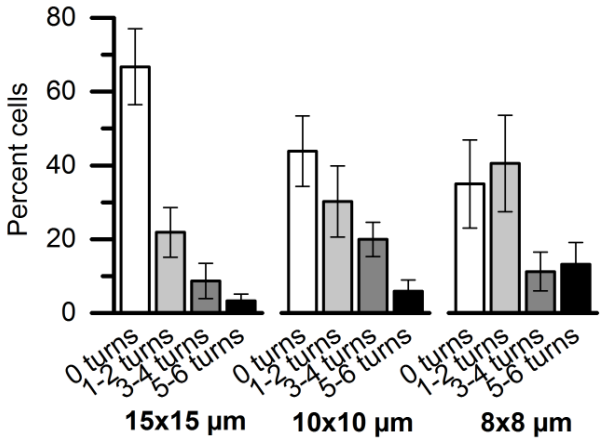

Fig. S3. Detailed cell migration analysis as a function of construct pore size. There is a clear trend towards more cells making at least one turn in the smaller pore constructs. It is less clear if the 8x8 µm pores induce more cell turns than the 10x10 µm pores. Error bars show the standard error of the man ($n \geq 3$).

Diffusion-based concentration gradients in woodpile constructs

The diffusivity of a compound A in a medium B can be written as D_{AB}. The diffusibility, Q, in a porous medium is then the ratio of the effective diffusivity, D_{eff}, of compound A through the porous medium to D_{AB}.[1] van Brakel and Heertjes expressed the diffusibility as:

$$Q = \frac{\varepsilon\delta}{\tau^2} \quad (\text{eq. } 1)$$

where ε is the porosity, δ the constrictivity, and τ the tortuosity. [2] The tortuosity τ is approximately unity in the woodpile design since the straight channels of the construct are parallel to the gradient direction outside the construct. The porosity is 0.71 for a perfect woodpile structure with 10 µm x10 µm pores separated by bars of cross-sectional dimensions 10 µm x 4 µm. The introduction of a 1.3 µm vertical overlap between overlying bars to optimize the mechanical stability reduces the porosity slightly to a value no smaller than 0.68. The constrictivity cannot be calculated directly. However, van Brakel and Heertjes estimated that the constrictivity does not depend on the particular shape of the porous structure but only on the ratio β between the maximum and minimum cross-sectional dimension of the porous path through the construct. For our woodpile design $\beta \approx 2$ corresponding to a constrictivity of approximately 0.9.[2] Inserting the worst case values into eq. 1 yields a diffusibility:

$$Q = \frac{0.68 \cdot 0.9}{1^2} = 0.61$$

The results shows that the effective diffusion constant is reduced by ~50% inside the construct compared to outside with a corresponding small delay in establishing a chemoattractant concentration gradient within the construct. However, the lateral extent of the construct is only up to 20% (200 µm) of the entire channel extent (1 mm) in the direction of the concentration gradient. This implies that the delay in gradient formation inside the construct will be insignificant in comparison to establishment of the channel-wide concentration gradient.

Description of the time-lapse movies

Movie 1: Migration of dendritic cells through a woodpile construct with 15x15 µm pores (see Fig. 4 in the main text). The image sequence has been processed to highlight the cells. Images were captured every 2 minutes.

Movie 2: Migration of dendritic cells through a woodpile construct with 15x15 µm pores. Same image sequence as Movie 1 but without any image processing. Images were captured every 2 minutes.

Movie 3: Migration of dendritic cells through a woodpile construct with 10x10 µm pores and added barrier structures (see Fig. 7 in the main text). The image sequence has been processed to highlight the cells. Images were captured every 2 minutes.

Movie 4: Migration of dendritic cells through a woodpile construct with 10x10 µm pores and added barrier structures (see Fig. 7 in the main text). Same image sequence as Movie 3 but without any image processing. Images were captured every 2 minutes.

References for Electronic Supplementary Information

1 J. Hoogschagen, *Ind. Eng. Chem.*, 1955, **47**, 906-913.

2 J. van Brakel and P. M. Heertjes, *Int. J. Heat Mass Transfer*, 1974, **17**, 1093-1103.